

## Propagating discontinuities in ionized porous media

**Citation for published version (APA):**

Kraaijeveld, F. (2009). *Propagating discontinuities in ionized porous media*. [Phd Thesis 1 (Research TU/e / Graduation TU/e), Biomedical Engineering]. Technische Universiteit Eindhoven.  
<https://doi.org/10.6100/IR652157>

**DOI:**

[10.6100/IR652157](https://doi.org/10.6100/IR652157)

**Document status and date:**

Published: 01/01/2009

**Document Version:**

Publisher's PDF, also known as Version of Record (includes final page, issue and volume numbers)

**Please check the document version of this publication:**

- A submitted manuscript is the version of the article upon submission and before peer-review. There can be important differences between the submitted version and the official published version of record. People interested in the research are advised to contact the author for the final version of the publication, or visit the DOI to the publisher's website.
- The final author version and the galley proof are versions of the publication after peer review.
- The final published version features the final layout of the paper including the volume, issue and page numbers.

[Link to publication](#)

**General rights**

Copyright and moral rights for the publications made accessible in the public portal are retained by the authors and/or other copyright owners and it is a condition of accessing publications that users recognise and abide by the legal requirements associated with these rights.

- Users may download and print one copy of any publication from the public portal for the purpose of private study or research.
- You may not further distribute the material or use it for any profit-making activity or commercial gain
- You may freely distribute the URL identifying the publication in the public portal.

If the publication is distributed under the terms of Article 25fa of the Dutch Copyright Act, indicated by the "Taverne" license above, please follow below link for the End User Agreement:

[www.tue.nl/taverne](http://www.tue.nl/taverne)

**Take down policy**

If you believe that this document breaches copyright please contact us at:

[openaccess@tue.nl](mailto:openaccess@tue.nl)

providing details and we will investigate your claim.

# **Propagating discontinuities in ionized porous media**

Famke Kraaijeveld

This research is performed as part of the collaboration "Multiscale Methods in Computational Mechanics" funded by the German and Dutch organizations for scientific research, DFG and NWO. The research itself was supported by the Technology Foundation STW, applied science division of NWO and the technology program of the Ministry of Economic Affairs. Further financial support was kindly provided by the Royal Dutch Shell.

A catalogue record is available from the Eindhoven University of Technology Library

ISBN: 978-90-386-1992-7

Copyright © 2009 by Famke Kraaijeveld. All rights reserved.

All rights reserved. No part of this book may be reproduced, stored in a database or retrieval system, or published, in any form or in any way, electronically, mechanically, by print, photo print, microfilm or any other means without prior written permission of the author.

This thesis is prepared with L<sup>A</sup>T<sub>E</sub>X 2<sub>ε</sub>

Cover design: Famke Kraaijeveld (*Beach near Mayres-Savel, France*)

Printed by the Universiteitsdrukkerij TU Eindhoven, Eindhoven, The Netherlands.

# Propagating discontinuities in ionized porous media

## PROEFSCHRIFT

ter verkrijging van de graad van doctor  
aan de Technische Universiteit Eindhoven,  
op gezag van de rector magnificus, prof.dr.ir. C.J. van Duijn,  
voor een commissie aangewezen door het College voor Promoties  
in het openbaar te verdedigen op  
dinsdag 6 oktober 2009 om 16.00 uur

door

Famke Kraaijeveld

geboren te 's-Gravendeel

Dit proefschrift is goedgekeurd door de promotoren:

prof.dr.ir. F.T.P. Baaijens

en

prof.Dr.-Ing. W. Ehlers

Copromotor:

dr.ir. J.M.R.J. Huyghe

# Contents

Contents	v
Summary	vii
List of symbols	xi
<b>I Introduction</b>	<b>I</b>
1.1 Scope: Swelling and fracture . . . . .	2
1.2 Objective . . . . .	9
<b>2 Biphasic model for saturated ionized porous media</b>	<b>II</b>
2.1 Introduction . . . . .	12
2.2 Governing equations . . . . .	13
2.3 Variational description . . . . .	16
2.4 Prestress . . . . .	18
<b>3 Singularity solution for shear loading</b>	<b>23</b>
Additional list of symbols . . . . .	24
3.1 Introduction . . . . .	24
3.2 Method . . . . .	25
3.3 Analytical solution . . . . .	28
3.4 Numerical example . . . . .	33
3.5 Results . . . . .	35
3.6 Discussion . . . . .	37
<b>4 Strong discontinuity model for shear loading</b>	<b>41</b>
4.1 Introduction . . . . .	42
4.2 Governing equations . . . . .	43
4.3 Numerical description . . . . .	51
4.4 Numerical examples . . . . .	56
4.5 Results . . . . .	59
4.6 Discussion . . . . .	65
<b>5 Weak discontinuity model for tensile loading</b>	<b>69</b>
5.1 Introduction . . . . .	70
5.2 Governing equations . . . . .	72
5.3 Numerical description . . . . .	77
5.4 Numerical examples . . . . .	83

5.5	Results . . . . .	87
5.6	Discussion . . . . .	93
<b>6</b>	<b>Discussion and conclusions</b>	<b>97</b>
	<b>References</b>	<b>103</b>
<b>A</b>	<b>Derivations for analytical solution</b>	<b>113</b>
A.1	Derivation of stress functions . . . . .	113
A.2	State variables in terms of Stress Functions . . . . .	115
A.3	Jump Condition Mode II . . . . .	115
A.4	Fourier and Laplace Transformations . . . . .	116
A.5	Laplace Solution . . . . .	119
A.6	Inverse Laplace . . . . .	120
A.7	Inverse Fourier transform . . . . .	125
A.8	Chemical potential and flow . . . . .	130
<b>B</b>	<b>Numerical aspects of a discontinuity</b>	<b>133</b>
B.1	Discontinuities and FEM . . . . .	133
B.2	Cohesive zone . . . . .	134
B.3	Yield criterion . . . . .	135
B.4	Implementation aspects . . . . .	135
	<b>Samenvatting</b>	<b>137</b>
	<b>Acknowledgement</b>	<b>141</b>
	<b>Curriculum vitae</b>	<b>143</b>

# Summary

## Propagating discontinuities in ionized porous media

Shales, clays, hydrogels and tissues swell and shrink under changing osmotic conditions. This change in conditions can lead to localized stresses and even to failure. These materials are described as a multi-phase materials consisting of a solid part with ions embedded in the porous solid matrix (fixed charges) and a fluid part containing mobile counter charges. That is why they are characterized as ionized porous media. The presence of the fixed charges causes an osmotic pressure difference between the material and surrounding fluid resulting in prestressing of the material. The response of the material to mechanical and chemical load is highly influenced by the presence of prestress, fluid and cracks. Understanding of the mechanisms for fracture and failure of these materials together with the fluid redistribution are important for material and construction design. Applications are found in the oil industry (e.g. hydraulic fracturing and borehole instability), material design (clay, diapers, orthopaedic prosthesis and seals) and medical treatment (intervertebral disc herniation and tissue engineering).

The relationship between the presence of cracks and fluid flow has had little attention, while the relationship between failure and osmotic conditions has had even less attention. The aim has therefore been to study the effect of osmotic conditions on propagating discontinuities under different types of loads for saturated ionized porous media using the Finite Element Method (FEM).

Discrete cracks are mathematically represented as displacement jumps, i.e. strong discontinuities. The modeling of cracks is challenging. Standard Finite Element models are not equipped to deal with discontinuous fields while they assume smooth displacement fields on forehand. Smeared or continuum approaches are suited for cases where no prominent crack can be distinguished.

An alternative to introducing discrete cracks into the FEM is exploiting the partition of unity property. The partition of unity method allows inclusion of discontinuous functions in the shape functions of the FEM and with that an approximation of the discontinuous field independently of the underlying mesh. For that purpose the number of degrees of freedom at the nodes is increased and not the amount of nodes, i.e. the topology is not altered. The method allows for crack propagation in arbitrary directions. In addition, inclusion of the crack prior to propagation is avoided, and so is the introduction of a nonphysical dummy stiffness to keep the crack closed before propagation.

Crack propagation in porous media is generally preceded by micro damage. This damage is introduced in the FEM by the cohesive zone model. The cohesive zone model lumps



all damage ahead of the physical crack-tip into one equation representing the debonding of the material and acting on a virtual extension of the crack. There is no consensus on the treatment of the fluid flow associated with crack evolution. Different approaches are taken.

In thesis the partition of unity method combined with cohesive zone modeling is applied to ionized porous media. The bulk material is described as a biphasic material (fluid and solid part). Ion flow contribution is assumed minimal compared to fluid flow and can therefore be neglected. Osmotic forces are added via constitutive modeling and initial stress. The model is described in chapter 2.

The work covers three parts. In the first part, an analytical solution of a dislocation in a swelling medium is derived acting as a benchmark for the second part. In the second part, the modeling of a propagating crack under shear loading (mode-II) is addressed. Finally, in the third part, the modeling of a crack under tensile loading (mode-I) in a swelling medium is addressed. The fluid flow associated with crack evolution is differently treated in the second and third part, since the different loading results in very different fluid flows.

Firstly, the distribution of shear stress is derived in the simplified situation of a non-propagating dislocation in an osmoelastic medium in chapter 3. This derivation requires Fourier and Laplace transformations. In addition, the distribution of the flow field is derived. Comparison of the analytical solution with computer simulations from a commercial code confirms the importance of a good crack representation. Hence, the analytical solution for a dislocation can be used as a benchmark to verify the partition of unity modeling in the second part.

Secondly, shear loading of a crack in an osmoelastic medium is addressed in chapter 4. Shear loading initially causes a high pressure gradient across the crack surfaces over a small transition zone, while the crack surfaces are still in contact. With time, the pressure relaxes in magnitude and the transition zone widens. This phenomenon is approximated by assuming that the fluid flow across the interface associated with damage is proportional to the jump in pressure. In addition, the associated proportionality constant depends on the time that passed since opening of the crack allowing for the relaxation of the fluid flow. Comparison of numerical simulations with the analytical solution of the first part shows a good match. Compression tests show that the pre-stress in the medium influences the crack propagation, both in terms of propagation velocity and direction. In addition, the results show that crack propagation is reasonably mesh-independent.

Finally, tensile loading is addressed in chapter 5. Tensile loading of a crack in an osmoelastic medium results in opening of the crack and high gradients between the pressure in the crack and the pressure of the fluid around the crack. This requires a model for the fluid flow around the crack that is essentially different for mode-I compared to mode-II. In mode-I, a weak discontinuity is assumed for the pressure in the crack area, while in mode-II a strong discontinuity across the crack is assumed for the pressure. In addition, in mode-I the fluid flow in the crack is approximated by Couette flow. Results show that depending on the load, permeability, prestress and

the stiffness of the material, when crack propagation initiates, fluid is attracted to the crack-tip from the crack rather than from the surrounding medium causing the crack to close and decreasing stress localization. Crack propagation is slowed down. The results show reasonable mesh-independent crack propagation for materials with a high stiffness.

Interestingly, step-wise crack propagation through the medium is seen both in mode-I and in mode-II. This is because the propagation of the crack alternates with pauses in which the crack-tip area consolidates. The consolidation results in a progressive transfer of the load from the fluid to the solid. As the load on the solid increases, the failure load is reached and the crack propagates again.

Furthermore, propagation is shown to depend on the osmotic prestressing of the medium. The dependence is present for mode-II and mode-I. In mode-II the prestressing has an influence on the angle of growth. In mode-I, the prestressing is found to enhance crack propagation or protect against failure depending on the load and material properties. It is found that osmotic prestressing in itself can propagate fractures without external mechanical load, such as the spontaneous formation of cracks during the drying of clay, but then in fully saturated conditions. This mechanism may explain the tears observed in intervertebral discs as degeneration progresses.



# List of symbols

$*$	$[-]$	Continuous field
$\tilde{*}$	$[-]$	Enhanced field
$[*]$	$[-]$	Jump over crack surface
$\vec{a}_u, a_\mu$	$[mm]$	Nodal values of continuous field
$\underline{B}$	$[mm^{-1}]$	Divergence of displacement shape functions: $\underline{B} = \underline{L}\vec{N}$
$\vec{b}_u, b_\mu$	$[mm]$	Nodal values of discontinuous field
$\underline{C}$	$[mm^{-1}]$	Divergence of chemical potential shape functions: $\underline{C} = \underline{L}^T \vec{l} m^T$
$c$	$[MPa]$	Deformation constant, $c = 2\mu + \lambda + \frac{\partial \Delta \pi}{\partial tr(\boldsymbol{\epsilon})}$
$c^{ex}$	$[mmol/mm^3]$	External salt concentration
$c^{fc}, c_i^{fc}, c_0^{fc}$	$[mmoleq/mm^3]$	Fixed charge concentration: current, initial, and at stress free state
$\underline{D}$	$[MPa]$	Material stiffness matrix
$\delta_{\Gamma_d}$	$[-]$	Delta Dirac function
$E$	$[MPa]$	Young's modulus
$\boldsymbol{\epsilon}, \boldsymbol{\epsilon}_i$	$[-]$	Current and initial strain tensor
$f_\Gamma^\pm$	$[mm/s]$	Normal flow over crack surface $\Gamma^\pm$
$\phi_i^f$	$[-]$	Initial volume fraction of the fluid
$\Gamma$	$[-]$	External boundary of body $\Omega$
$\Gamma_d, \Gamma_d^\pm$	$[-]$	Discontinuity boundaries: $\Gamma^\pm = \Gamma_d \cap \Omega^\pm$
$\mathcal{H}_{\Gamma_d}$	$[-]$	Heaviside function at discontinuity $\Gamma_d$
$K$	$[mm^4/Ns]$	Bulk permeability
$K_d$	$[mm^5/Ns]$	Crack permeability
$k_d$	$[mm^5/Ns]$	Unresolved hydraulic permeability
$l_a$	$[mm]$	Nonlocal length, measure for stress singularity
$\lambda$	$[MPa]$	Lamé constant

$\tilde{m}$	$[-]$	shape functions for chemical potential
$\tilde{\mu}$	$[MPa]$	Lamé constant, shear modulus
$\mu^f$	$[MPa]$	Chemical potential
$\tilde{N}$	$[-]$	shape functions for displacement
$\tilde{n}$	$[-]$	Normal unit vector on $\Gamma$ , directed outward $\Omega$
$\tilde{n}^\pm$	$[-]$	Normal unit vector on $\Gamma_d$ , directed to $\Omega^\pm$
$\nu$	$[-]$	Poisson's ratio
$\vec{\nabla}^s$	$[mm^{-1}]$	Symmetric divergence, $\vec{\nabla}^{s*} = 1/2\{\vec{\nabla} * + (\vec{\nabla} *)^T\}$
$\Omega$	$[-]$	Body of interest
$\Omega^\pm$	$[-]$	Body of interest in direction $\tilde{n}^\pm$ of $\Gamma_d$
$\Delta\pi$	$[MPa]$	Osmotic pressure difference $\pi - \pi_{ex}$
$\vec{q}$	$[mm/s]$	Seepage flux
$R$	$[Nmm/mmolK]$	Gas constant
$\sigma, \sigma_e$	$[MPa]$	Total and effective stress
$T$	$[K]$	Temperature
$\underline{T}_d$	$[MPa/mm]$	Tangent stiffness of cohesive law in local coordinates
$t$	$[s]$	Time parameter
$\vec{t}^+$	$[-]$	Tangential vector unit directed towards propagation
$\vec{t}_\Gamma^\pm$	$[-]$	Traction force at discontinuity surface $\Gamma^\pm$
$\vec{u}$	$[mm]$	Displacement
$x, y$	$[mm]$	Spatial parameters

## CHAPTER ONE

# Introduction

## 1.1 Scope: Swelling and fracture

Ionized porous media, such as shales, clays and soft tissues, swell and shrink under changing osmotic conditions. These materials are represented as a multi-phase material consisting of a solid matrix with polyvalent ions attached, the fixed charges [44,67]. The presence of the fixed charges together with mobile counter ions in the medium leads to a higher concentration of ions inside the medium than outside. The result is an osmotic pressure difference and a prestress on the solid matrix. These materials desire to absorb water and swell. In addition, ionized porous media can undergo phenomena like instability, localization and even fracturing under changing osmotic conditions [87,III].

Deformation as result of swelling in a hydrogel are given in Figs. 1.1 and 1.2. Hydrogel is a common physical model for soft tissues and consists of cross-linked ionized polymers. In both cases a hydrogel colored is moved from a highly concentrated salt solution to a less concentrated salt solution. The sample starts to swell, because of the high ionization of the gel.

In the first case a weakly cross-linked sample is considered. During swelling, surface instability is seen followed by other modes of instability (Fig. 1.1). This is the result of the outside swelling faster than the core. The strains on the solid matrix are large. Finally, the original shape is restored, only bigger.

In the second case, Fig. 1.2, the experiment is repeated with a highly cross-linked ionized

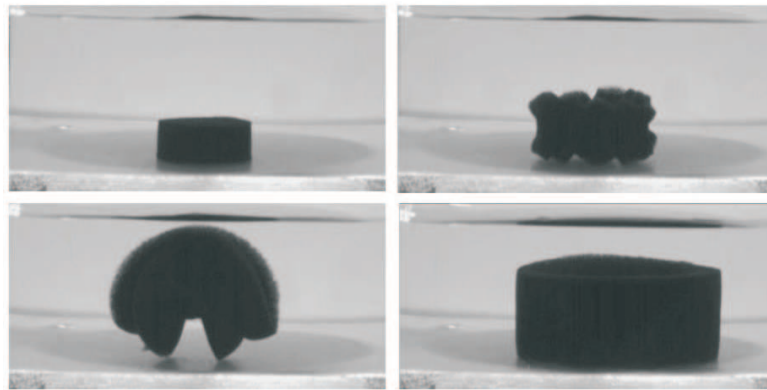


**Figure 1.1:** Instability in successive states of swelling of a hydrogel. Time runs from top left, top right, bottom left to bottom right.

gel. The strong cross-linking produces a much higher stiffness than the previous case. This time a mirror is placed in the upper right corner to monitor evolution from the top. The resulting swelling is prohibited by the solid matrix, causing high stresses. In this case the local stresses exceed the maximum stress the material can bear. The matrix fails and chops fly off. Failure has taken place without an external load.

Failure of swelling materials often have large environmental and financial consequences.



**Figure 1.2:** Failure of a hydrogel during swelling. Time runs from top left, top right, bottom left to bottom right.

Some examples are addressed.

### 1.1.1 Example 1: Borehole instability

Oil reservoirs are typically found under low-permeability clay-rich formations, simply because these formations trap the oil. While drilling, the drill has to pass at least one layer of rock rich in swelling ionized poly-silicates. During drilling the drill is cooled down and guided by a mud. This mud used to be oil-based, but these days the mud has been replaced by a salty water-based mud in view of the environment. These swelling rocks, shale or claystone, start swelling as soon as they are in contact with the drilling fluid, eventually leading to borehole instability, particularly in deviated borehole. Accurate choice of drilling fluid composition postpones the failure of the shale or claystone, hence delaying borehole instability.

### 1.1.2 Example 2: Hydraulic fracturing

Tight gas sands are typically low porosity, low permeability rocks. They account for about 15% of U.S. gas production. Tight sands require advanced fracture technologies to be exploited efficiently. Hydraulic fracturing is the key technology in tight gas development. Most tight gas reservoirs have to be fractured before they flow at commercial rates. In the 1990s, slick-water fracturing techniques were developed. The slick water used high volumes of water and low concentrations of proppant. Multi-stage fracturing was another development, allowing several stages to be treated in quick succession. At present, the choice of technique depends on the characteristics of a reservoir. Numerical simulation techniques describing the fracture propagation coupled to the fluid exchange between the fracture and the formation are highly desirable to enhance the understanding of the process of hydraulic fracturing.



### 1.1.3 Example 3: Intervertebral disc herniation

Intervertebral disc (IVD, Fig. 1.3a) tissue is mechanically described as a porous matrix containing water with mobile ions. The porous matrix is constructed from collagen, cells and entangled large polyvalent ions, namely proteoglycans (PGs) [67,99]. Disc tissue is therefore swollen highly prestressed. These properties help in giving the spine its range of motion and in absorbing shocks.

Low back pain is associated with IVD herniation (Fig. 1.3b) and is a major health problem which affects 60%-90% of the population between 20-50 years. Treatment and out-fall causes costs similar in magnitude to those of diabetes [100]. New multi-disciplinary collaborations are trying to combine the disciplines of cell biology, patient studies, imaging techniques and numerical simulations in order to develop new insights and treatments [100].

During ageing, the disc changes in structure, composition, volume and prestress. Eti-

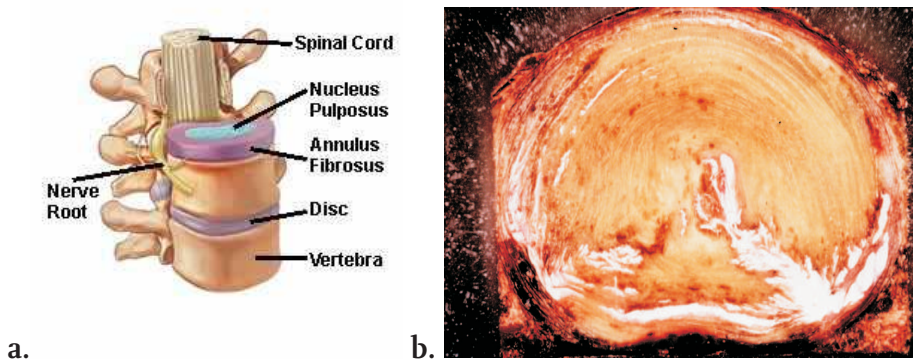


**Figure 1.3:** a. Overview of a spine with vertebrae and intervertebral discs (adopted from <http://www.spineuniverse.com>). b. A herniated disc, courtesy of T. Videman. The *anterior* is at the top of the figure and *posterior* at the bottom.

ology shows that the amount of cracks increases with ageing of the disc [3,100]. The prestress in the disc decreases due to loss of ionization [6,43]. Ageing, loss of ionization of PGs and presence of fissures in the disc seem to be strongly linked. This appears contradictory since material under tension is easier to break than something that is not. Some papers suggest that aged discs are more susceptible to injuries than healthy discs and that fissures are the result of injuries [18,42,95,96]. Others have been able to produce fissures in healthy discs [19,113] and suggest that fast ageing is the result of an injury. Twin studies showed that occupation (i.e. loading history) is of less influence than familiarity [11,105]. Clearly, there is no consensus on the etiology of IVD herniation.

### 1.1.4 Preliminary study

Many computational models have been developed to study the ageing of intervertebral disc and risks for herniation. Unfortunately, many researchers either neglected the pres-

ence of fluid [50] or the presence of fixed charges [61]. Wognum et al. [111] investigated the effect of a decrease in osmotic forces on a pre-existing crack in two models for the intervertebral disc. Firstly, by a physical experiment with hydrogel (Fig. 1.4) showed that existing cracks open under decreasing osmotic pressure and become visible.

Secondly, by a (quadriphasic) numerical model (Fig. 1.5), the opening of an existing crack

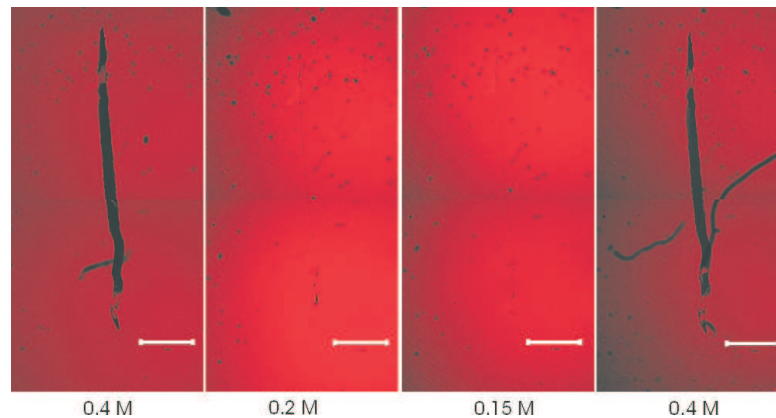


**Figure 1.4:** Swelling and shrinking of a hydrogel. Cracks open and close under changing osmotic conditions [111].

under decreasing osmotic pressure was simulated.

As it is well known that osmotic pressure decreases with degeneration, these two models suggest that the decrease in osmotic pressure may induce opening of cracks and propagation of cracks in the degenerating disc.

Wognum et al. [111] did not simulate propagation of cracks, nor did they verify their

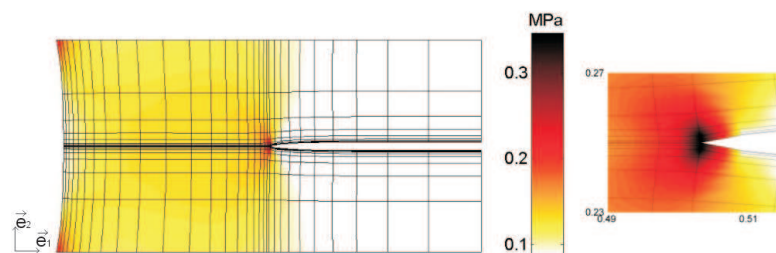


**Figure 1.5:** Stress distribution of component  $\sigma_{22}$ . Decreasing the osmotic pressure causes a global decrease in stress, and a local increase of stress at the tip [111].

hypothesis in human disc tissue.

### 1.1.5 Computational models of fracture

Most computational models are based on Finite Elements (FE). FE uses a grid and shape approximations to calculate the fields of interest. Ingredients of computational fracture

models are as follows.

- Model for bulk behavior
- Method for including discontinuities in the FEM
- Damage initiation or yield criterion
- Damage evolution model or constitutive model for crack growth

Computational models for the simulation of fractures are of two kinds: continuous and discrete. There are two approaches to the numerical analysis of failure in media, continuum damage mechanics and fracture mechanics [23]. In continuum damage mechanics there is no prominent crack to be distinguished, but discontinuities are distributed over a finite volume. In continuous models failure is simulated using a smooth displacement everywhere in the body, such as in plastic behavior. This means that the strain field and stress field is defined uniquely everywhere. Discrete models allow for a change in gradient (weak discontinuity) or a jump (strong discontinuity) of the displacement field (Fig. 1.6). The presence of discontinuities in the displacement affects the gradient of the field, i.e. strain (bottom of Fig. 1.6). Physically a discontinuity means that a failure surface has developed within the body and continuum theory cannot be used anymore.

Fractures in ionized porous media are discrete in nature, for instance herniation

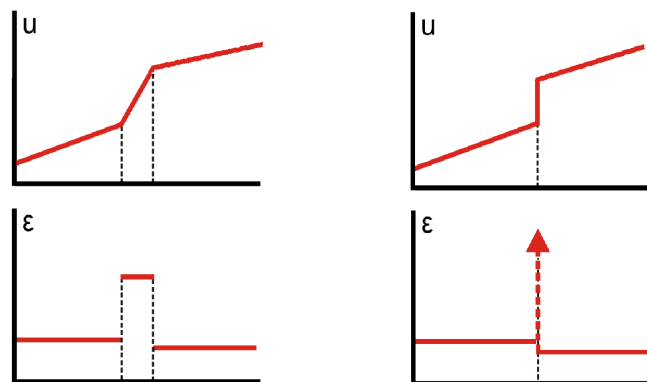


**Figure 1.6:** Displacement  $u$  and strain  $\epsilon$  as a function of space. Left: weak discontinuity in strain field causes strong discontinuity in strain field. Right: strong discontinuity in displacement causes strain not to be defined at the discontinuity.

(Fig. 1.3). Jumps in displacement are seen, therefore we would like a discrete fracture model. A small damage zone, the so-called process zone, ahead of the growth of the macro-crack is seen in which micro-separations and crack-bridging (fibers running from one crack-surface to the other) takes place (Fig. 1.7a). The fracture is preceded by a damage zone, therefore the material is classified as quasi-brittle.

Models based on linear elastic fracture mechanics (LEFM) cannot capture this nonlinear behavior in the process zone. The exact evolution of micro-damage to macro-cracks is highly dependent on the material, i.e. location in the disc. Phenomena like heterogeneity and initial defects influence final crack patterns. A way to describe damage is the introduction of the cohesive zone. Barenblatt [10] and Dugdale [30] introduced the concept of cohesive zone for cases where the length of the process zone is small compared to the structural dimensions. In this concept all processes in the process zone are lumped into a relationship between load and debonding of the material, i.e. traction forces and displacement, in a fictional extension of the crack. The nature of the work of the cohesive zone is such that the stress singularity in the crack-tip is canceled. The traction forces reduce to zero towards the actual crack-tip, Fig. 1.7b. Needleman [75] introduced these cohesive elements at all element boundaries allowing for crack nucleation and a constitutive model determining length of damage zone.

A benefit of this method is that the stress singularity at the crack-tip predicted by LEFM is removed and all physical processes ahead of the tip are reduced to one simple equation. The actual shape of the cohesive zone model is still a point of research [20,101,112].

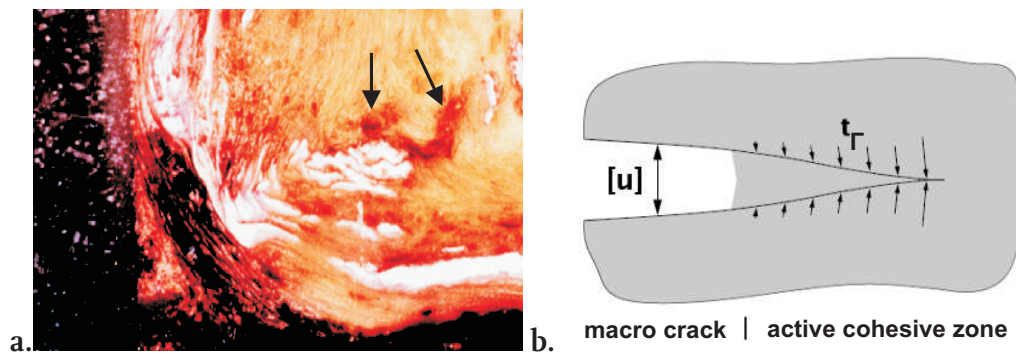


**Figure 1.7:** a. Close-up from a herniation (Fig. 1.3, courtesy of T. Videman) with micro-damage at the crack-tip pointed out by the arrows. b. Schematic representation of the cohesive zone.

There are several discrete methods to introduce discontinuities in FEM: adaptive remeshing, interface elements or meshless methods [23]. In adaptive remeshing the mesh is continually remodeled to fit the discontinuity between the elements (geometrical approach). Remeshing is computationally expensive and difficult to implement. Interface elements use elements of zero width that are fitted between the elements to model the discontinuity (appendix B, Fig. B.2). The nodes of the new elements are related to the nodes of the continuum elements. Interface modeling requires alignment of the element with the crack path a priori. Therefore the discontinuity path depends on the mesh and a dummy stiffness is required to prevent the crack from debonding when it is not physical [23]. A dummy stiffness that is too low produces a too flexible response and a dummy stiffness that is too high produces oscillations.

Meshless methods incorporate a displacement jump by cutting the domain (Embedded

Discontinuity Elements) or adding discontinuous functions to the shape functions of the FE (Partition of Unity or eXtended Finite Element method) [9,12]. Embedded Discontinuity Element is based on adding the effect of a displacement jump to the finite elements as an incompatible strain mode. Unfortunately these methods lack robustness [23]. PU-FEM and X-FEM were developed in the nineties and use enhancement functions to add discontinuities to the standard shape functions of the FE, for instance a jump is introduced by adding the Heaviside function. The use of these enhanced functions makes it possible to preserve continuity along the crack surface. The discontinuity is projected on the element by additional degrees of freedom and not nodes. It is not necessary to align elements with the crack path, no dummy stiffness is needed nor remeshing is required. Furthermore, standard discretization is used. The partition of unity is a powerful property which can also be used for other scale separation than crack growth, for instance material separation [38,39]. The benefit of this method is also that relatively coarse meshes can be used. Unfortunately, the method is not easy to implement in commercial codes.

Where in previous research the cohesive zone model has been introduced either at all element boundaries [112] or in the path of interest [86,88], the application of partition of unity on discontinuity kinematics allowed for the cohesive zone to cross continuum elements [70,80,107].

An increasing amount of papers is published on applying these tools in biomechanics [37], in which fluid contribution is unfortunately usually neglected. The presence of fluid highly affects the mechanical response of the structure, fracture initiation and fracture growth. Most computational poromechanical models involving strong discontinuities consider shear banding (mode-II, denoted in appendix B, Fig. B.1a) in porous media where fluid exchange from one crack surface to the other is assumed continuous [7] or decreased [82]. The partition of unity method has been combined with Delta-dirac function [58] for simulating an undrained localization band.

In tensile mode (mode-I, denoted in appendix B, Fig. B.1b), applications to hydraulic fracturing is seen where benchmarks are available when assuming little exchange of fluid between the fracture and surrounding fluid [16,17,34]. With efficient mesh generators and transfer schemes, fracturing of porous media has been successfully modeled by adaptive meshing without making assumptions on the shape of the pressure field or displacement [89,93,94]. Mesh refinement plays a large role in these models.

The partition of unity method allows for relatively coarse meshes in solid mechanics. Correctly capturing the pressure field corresponding to a displacement discontinuity is not straightforward. Attempts for combining partition of unity model with porous media in tensile mode are a double porosity model for the fluid flow without enhancing the fluid phase [4], a moisturizing model without enhancing the fluid phase [85] and a weak discontinuity model for the fluid phase with Couette flow in the crack [83]. Still, numerical simulations of a fracturing process in a porous medium are limited and it is difficult to verify and validate model performance with a benchmark. In any case no osmotic effects were taken into account.

## 1.2 Objective

The objective of this research is to explore the effect of osmolarity on propagating quasi-brittle macro cracks in ionized porous media with Finite Elements. For that, a Finite Element method is needed which allows for the inclusion of displacement discontinuities and the associated pressure field. This inclusion should be independent of the underlying mesh. The requirement that results are independent of spatial discretization, limits the choice of method to PU-FEM or X-FEM.

- the computed results are mesh-independent
- no remeshing is required
- no artificial length scale have to be introduced in the constitutive model
- fluid flow over crack surfaces is enabled

To reach that aim, several steps were defined.

- **Step 1.** Singularity solution for shear loading in ionized porous media
- **Step 2.** Model for crack propagation under shear loading in ionized porous media
- **Step 3.** Model for crack propagation under tensile loading in ionized porous media

An analytical singularity solution is developed for a non-propagating crack in shear loading. This analytical solution is used as a benchmark to verify the partition of unity model which is developed in the second step. This model captures a propagating crack in shearing (mode-II) conditions. With this model the effect of osmotic conditions on crack growth is studied. Lastly, a partition of unity model is developed for tensile (mode-I) loading in a swelling porous medium. The models for shear loading and tensile loading require different treatment of the fluid flow related to the discontinuity. The model is used to determine if the osmotic conditions on crack propagation as result of external loading and internal loading, i.e. a change in osmotic conditions. These steps form the outline of this thesis.



## CHAPTER TWO

# **Biphasic model for saturated ionized porous media**



## 2.1 Introduction

Experimental measurements in porous media are difficult, especially in the spine. For this reason, computational models are addressed to aid in the understanding and prediction of mechanical and chemical response of ionized porous media such as the intervertebral disc. The models allow for the study of the relation of different parameters and complex loading conditions, such as cyclic loading. The difficulty and challenge, though, lies in verifying (assessing numerical accuracy), analyzing sensitivity (assessing dependence of the results on input parameters) and validating (comparison to real-life) the models [48,74].

Different models for the intervertebral disc exist. Several papers have focussed on geometrically and material nonlinearity and global responses to complex loading conditions [50,63]. In these cases, the annulus is represented by a solid material and the nucleus is modeled by applying a hydrostatic pressure on the wall, either as boundary condition or by use of solid elements. Unfortunately, the contribution of fluid has been neglected. The load exchange between fluid and solid is not captured, and therefore time-dependent effects, such as creep, are not captured. Furthermore the presence of fluid might enhance or decrease localization.

Based on the poro-elastic and chemical electric (PEACE) model [46] Iatridis et al. found that changing the fixed charge density from a healthy disc to a degenerated disc, the stresses in the solid matrix increased and streaming potential decreased which can have consequences for cell nutrition and remodeling which agrees with experiments [47]. Natarajan et al. [73,74] studied cyclic loading of the disc concluding that a healthy disc is more flexible and that with increased cycles the height of the disc decreases as found in experiments [2].

Models including fluid (poro-mechanical models) are usually based on Biot's model [13, 14] consisting of momentum balance, mass balance and constitutive relations. Furthermore, osmotic forces have to be added to the model.

For this reason, Lanir et al. [56,57] have extended Biot's model and include osmotic forces via constitutive laws and initial stress. Ion flow contribution is assumed minimal compared to fluid flow and can therefore be neglected. Based on this model, finite element studies have been able to predict stress profiles, hydrostatic pressure and material properties in the intervertebral disc within physical range [91,92].

Lai et al. [54] included ion flow as the third phase using physico-chemical theory allowing for the tracing of ion contribution. The model has been used to study articular cartilage [55,71]. Huyghe et al. [44] introduced a quadriphasic model, separating cations and anions, including electrical fluxes and streaming potential based on mixture theory. Mixture theory represents the porous media is represented by a spatially superposed interacting media [21]. The model has been implemented by Van Loon et al. [102], where mass balance is satisfied in a weak sense. The quadriphasic model has been molded into a mixed-hybrid formulation by Malakpour et al. [65,66] satisfying mass balance at the element boundary. With the quadriphasic model the effect of osmolarity has been studied on tissue [43] and cracks [111].

Ehlers et al. [31,32] described the inhomogeneous behavior of the human intervertebral

disc including electro-chemo-mechanical couplings by mixed FEM based on the Theory of Porous Media.

Different models seem successful at capturing trends. Wilson et al compared a biphasic model [56,109] to the quadriphasic model [44,102] for confined compression and 1D swelling. As chemo-electro-mechanical models are complex and computationally expensive, it was shown that a biphasic model was sufficient to capture the mechanical behavior of the material, i.e. stresses and strains due to mechanical or chemical perturbations. Therefore for cases where ion flux is not the focus, a biphasic model is sufficient. This research aims at studying the effect of osmolarity on propagating quasi-brittle macro cracks in ionized porous media in general. Therefore the biphasic model by Lanir [56] is used. This model is stated here. A 1D swelling solution is derived for verification. Lastly, the variational description is given.

## 2.2 Governing equations

Lanir's biphasic model [56] for osmotically swelling media is used. A charged solid saturated continuum is considered with a fluid, namely water containing freely diffusing solutes of low molecular weight subjected to an external salt concentration. The material is assumed to be isothermal, isotropic, homogeneous and fully saturated.

Mixture theory is used [98]. This means that not every particle in the medium is described, but the properties of the constituents are spread over a representative volume unit (RVU), represented in Fig. 2.1. This volume is large enough to provide a good representation, but small enough to avoid averaging out macroscopic variations, which is similar to homogenization of microscopic scale to define a material point at the macroscopic level [29].

The ion flow is assumed to be infinitely fast with respect to fluid flow. This means that

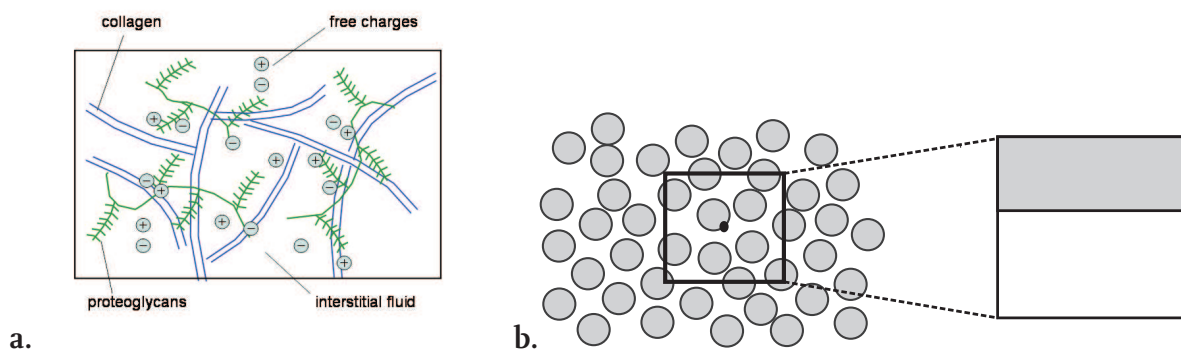


**Figure 2.1:** a. Schematic overview of the disc tissue with its components: water, collagen and PGs. b. Quantities are averaged over a volume RVU, and represented by volume fractions of the components.

on forehand an equilibrium is reached with the external salt solution. The medium is therefore described by only two constituents: the solid (s) and the interstitial fluid (f).

Since the compressibility of the constituents is small with respect to the compressibility of the medium, the constituents are assumed to be incompressible. Small deformation theory is used.

The model consists of momentum balance, mass balance and a swelling equation for the bulk. For the balances the forces on the solid and fluid separately play a part but also the influence of the constituents on each other. Biot's model [13] is used as a basis for the bulk. Osmotic swelling is added to these equations by means of chemical potential.

### 2.2.1 Momentum equation

The stress in the mixture follows Terzaghi's rule of effective stress  $\sigma_e$  [98]. If inertia and body forces are neglected, the momentum balance reads

$$\vec{\nabla} \cdot \sigma = \vec{0}. \quad (2.1)$$

The stress is split into two parts, effective stress and hydraulic pressure ( $p$ ). The effective stress contains all effects of the fluid and the solid related to deformation.

$$\sigma = \sigma_e - p\mathbf{I}. \quad (2.2)$$

In small deformation theory the effective stress ( $\sigma_e$ ) follows the (constitutive) linear and reversible stress-strain relation.

$$\sigma_e = 2\mu\epsilon + \lambda \text{tr}(\epsilon)\mathbf{I}, \quad (2.3)$$

with the strain tensor  $\epsilon = 1/2\{\vec{\nabla}\vec{u} + (\vec{\nabla}\vec{u})^T\} = \vec{\nabla}^s\vec{u}$  and  $\text{tr}(\epsilon) = \vec{\nabla} \cdot \vec{u}$ . The parameters  $\mu = G = \frac{E}{2(1+\nu)}$  (isotropic) and  $\lambda = \frac{\nu E}{(1+\nu)(1-2\nu)} = \frac{2\nu G}{1-2\nu}$  denote the Lamé constants.  $E$ ,  $\nu$  and  $G$  are the Young's modulus, Poisson's ratio and shear modulus respectively.

Then the momentum equations are given by

$$2\mu\vec{\nabla} \cdot \epsilon + \lambda\vec{\nabla}\text{tr}(\epsilon) - \vec{\nabla}p = \vec{0}. \quad (2.4)$$

### 2.2.2 Mass equation

The volume fractions are given for the solid by  $\varphi^s = \frac{V^s}{V}$  and for the fluid part by  $\varphi^f = \frac{V^f}{V}$ . The medium is fully saturated so (2.5) holds.

$$\varphi^f + \varphi^s = 1. \quad (2.5)$$

The volume of the medium can change through fluid flow and therefore the volume fractions can alter. An additional subscript 0 will refer to the stress free configuration.

In absence of chemical reactions, the mass balance per component becomes (2.6) with  $\alpha = f, s$  and  $D/Dt$  spatial time derivative.

$$\frac{D\varphi^\alpha}{Dt} + \nabla \cdot (\varphi^\alpha \vec{v}^\alpha) = 0. \quad (2.6)$$

Combining equations (2.5) and (2.6) the total mass balance (2.7) is found for incompressible constituents.

$$\vec{\nabla} \cdot \vec{v}^s + \vec{\nabla} \cdot \vec{q} = 0, \quad (2.7)$$

with  $\vec{q} = [\varphi^f(\vec{v}^f - \vec{v}^s)]$  denoting the filtration flux or seepage flux.

### 2.2.3 Swelling equation

To introduce swelling into the model, gradients in chemical potentials are introduced. The presence of polyvalent molecules in the solid causes a concentration effect with the external solution. This effect is called Donnan-osmosis. Because of the presence of ions, both solid and fluid have chemical potentials partly determined by the osmotic pressure. The chemical potential of a constituent is a measure for the free energy of that constituent. So the chemical potential of the fluid is a measure for the fluid flux.

Lanir [56] neglects the time effect of chemical potential response to local ionic diffusion, which is assumed to be much faster than filtrational or mechanical response. This means that equilibrium of ions is immediately reached. We define the chemical potential of the fluid  $\mu^f$  as follows.

$$\mu^f = p - \pi, \quad (2.8)$$

with  $\pi$  the osmotic pressure and  $p$  the hydrostatic pressure. The seepage flux follows Darcy's law in presence of concentration gradients (2.9) and therefore relates to the chemical potential:

$$\vec{q} = -\mathbf{K} \cdot \vec{\nabla}(p - \pi) = -\mathbf{K} \cdot \vec{\nabla}\mu^f, \quad (2.9)$$

with  $\mathbf{K}$  the permeability tensor. When isotropic conditions are considered for the bulk the permeability is constant,  $\mathbf{K} = KI$ .

Van 't Hoff empirical relation defines the osmotic pressure in terms of concentrations of free cations,  $c^+$ , anions  $c^-$ , gas constant  $R$  and temperature  $T$ . In case of perfect osmotic equilibrium the osmotic pressure is given by (2.10)

$$\pi = RT(c^+ + c^-). \quad (2.10)$$

Equilibrium with the external salt solution and the electro-neutrality condition, requires that:

$$c^+ + c^- = \sqrt{(c^{fc})^2 + 4(c^{ex})^2}. \quad (2.11)$$

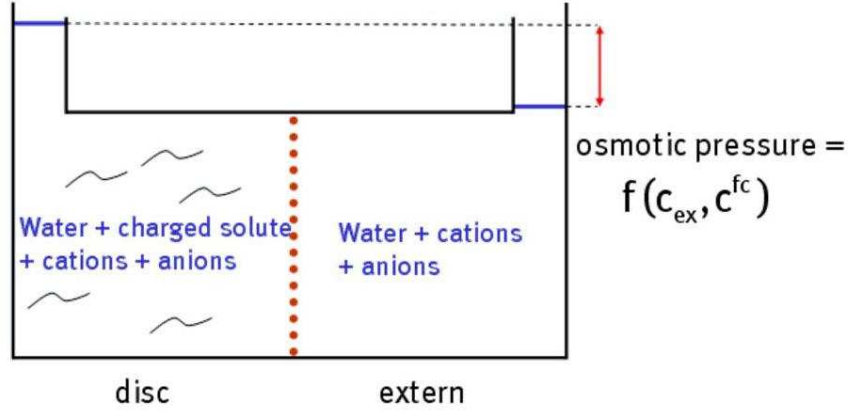


Figure 2.2: Schematic overview of Donnan osmosis.

Here  $c^{ex}$  denotes the external salt concentration and is known. The fixed charge density  $c^{fc}$  depends on the volume of the sample and therefore on the deformation. It is measured by determining the equivalent salt concentration and therefore units are denoted in  $moleq/m^3$  instead of  $mol/m^3$ . In the small strains setting it is assumed that the initial volume fraction is equal to the volume fraction at stress free state. Defining  $c_0^{fc}$  the fixed charge density at stress free configuration, the next holds

$$c^{fc} = \frac{\varphi_0^f c_0^{fc}}{(\varphi_0^f + tr(\epsilon))} \quad (2.12)$$

Then the difference in osmotic pressure between the material and the external salt solution is given by

$$\Delta\pi(\epsilon) = RT\Gamma_{in} \sqrt{(c^{fc})^2 + 4(c^{ex})^2} - 2\Gamma_{ex}c^{ex}. \quad (2.13)$$

## 2.3 Variational description

The governing equations consist of equations for the bulk and for the discontinuity, dominated by mass balance, momentum balance and constitutive behavior. Figure 2.3 shows a body  $\Omega$  with external boundary  $\Gamma$  with a traction force on  $\Gamma_t$  and fluid supply on  $\Gamma_f$ , with  $\vec{n}$  the normal unit vector on the boundary  $\Gamma$  directed outwards. The body is cut by a discontinuity  $\Gamma_d$  in two domains,  $\Omega^+$  and  $\Omega^-$ . The normal of the discontinuity  $\vec{n}_\Gamma$  is directed towards  $\Omega^+$ .

### 2.3.1 Momentum balance

In the solid subproblem a correction for deformation because of osmotic pressure is already accounted for. We assume inertia forces are negligible and traction forces are

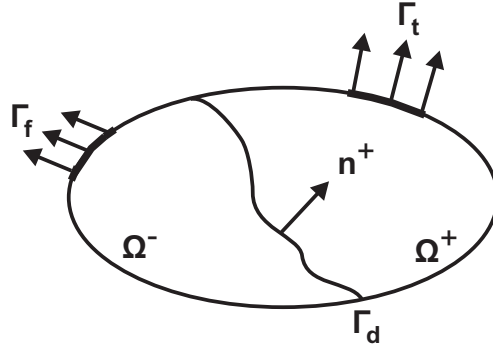


**Figure 2.3:** Schematic representation of the body  $\Omega$ : the two parts are  $\Omega^+$  and  $\Omega^-$ , separated by crack  $\Gamma_d$ . A traction force holds on  $\Gamma_t$  and fluid supply at  $\Gamma_f$ .

included. The strong equations on body  $\Omega$  are given by the equation of motions, strain-displacement relation and constitutive law.

$$\begin{aligned}\vec{\nabla} \cdot \boldsymbol{\sigma}_e - \vec{\nabla} \mu^f &= \vec{0}, \\ \boldsymbol{\sigma}_e &= \boldsymbol{\sigma}_e(\boldsymbol{\epsilon}), \\ \boldsymbol{\epsilon} &= \vec{\nabla} \cdot \vec{u}.\end{aligned}\tag{2.14}$$

with boundary conditions and initial conditions ( $\Gamma_t \cup \Gamma_u = \Gamma$  and  $\Gamma_t \cap \Gamma_u = \emptyset$ )

$$\begin{aligned}\vec{u}(\vec{x}, 0) &= \vec{u}^i(\vec{x}), & \vec{x} &\in \Omega, \\ \vec{u}(\vec{x}, t) &= \vec{u}^\gamma(\vec{x}, t), & \vec{x} &\in \Gamma_u, \\ (\boldsymbol{\sigma}_e - \mu^f \mathbf{I}) \cdot \vec{n} &= \vec{t}(\vec{x}, t), & \vec{x} &\in \Gamma_t\end{aligned}\tag{2.15}$$

The equations have to hold in all circumstances. From the Hu-Washizu functional the strong equations are multiplied by variations of the functions and then integrated over the body  $\Omega$ . Using partial integration and Gauss theorem the boundary conditions are integrated in the variational formulation:

$$\begin{aligned}\int_{\Omega} \vec{a} \cdot (\vec{\nabla} \cdot \mathbf{B}) d\Omega &= 0 \\ \Leftrightarrow \int_{\Omega} (\vec{\nabla} \cdot (\vec{a} \cdot \mathbf{B}) - \vec{\nabla} \vec{a} : \mathbf{B}) d\Omega &= 0 \\ \Leftrightarrow - \int_{\Omega} \vec{\nabla} \vec{a} : \mathbf{B} d\Omega + \int_{\Gamma} (\vec{a} \cdot \mathbf{B}) \cdot \vec{n} d\Gamma &= 0\end{aligned}\tag{2.16}$$

Then the variational formulation becomes

$$\begin{aligned}\int_{\Omega} \vec{\nabla} \vec{\eta} : \boldsymbol{\sigma}_e d\Omega - \int_{\Omega} \vec{\nabla} \vec{\eta} : \mu^f \mathbf{I} d\Omega &= \int_{\Gamma_t} \vec{\eta} \cdot \vec{t} d\Gamma \\ \int_{\Omega} (\vec{\nabla} \boldsymbol{\tau} \cdot \vec{u} + \boldsymbol{\tau} : \boldsymbol{\epsilon}) d\Omega &= \int_{\Gamma_u} (\boldsymbol{\tau} \cdot \vec{u}^\gamma) \cdot \vec{n} d\Gamma \\ \int_{\Omega} \boldsymbol{\gamma} : (-\boldsymbol{\sigma}_e + \boldsymbol{\sigma}_e(\boldsymbol{\epsilon})) d\Omega &= 0.\end{aligned}\tag{2.17}$$

Here  $\vec{\eta}$ ,  $\boldsymbol{\tau}$  and  $\boldsymbol{\gamma}$  are the variations in displacement, stress and strain respectively.

### 2.3.2 Mass balance

The strong equations on body  $\Omega$  are dominated by the mass balance. They are given by continuity equation, Darcy's law and velocity equation.

$$\begin{aligned}\vec{\nabla} \cdot \vec{v} - \vec{\nabla} \cdot \vec{q} &= 0, \\ \vec{q} &= -\mathbf{K} \cdot \vec{\nabla} \mu^f, \\ \vec{v} &= \dot{\vec{u}}.\end{aligned}\tag{2.18}$$

with boundary and initial conditions are ( $\Gamma_f \cup \Gamma_\mu = \Gamma$  and  $\Gamma_f \cap \Gamma_\mu = \emptyset$ )

$$\begin{aligned}\vec{v}(\vec{x}, 0) &= \vec{v}_i(\vec{x}), & \vec{x} \in \Omega, \\ \mu^f(\vec{x}, 0) &= \mu_i^f(\vec{x}), & \vec{x} \in \Omega, \\ \mu^f(\vec{x}, t) &= \mu_{\Gamma_\mu}^f(\vec{x}, t), & \vec{x} \in \Gamma_-, \\ \vec{q} \cdot \vec{n} &= f(\vec{x}, t), & \vec{x} \in \Gamma_f\end{aligned}\tag{2.19}$$

Then the variational formulation becomes

$$\begin{aligned}\int_{\Omega} \vec{\nabla} \varphi \cdot \vec{q} d\Omega - \int_{\Omega} \varphi \vec{\nabla} \cdot \vec{v} d\Omega &= \int_{\Gamma_f} \varphi f d\Gamma \\ \int_{\Omega} \vec{\psi} \cdot (\dot{\vec{u}} - \vec{v}) d\Omega &= 0 \\ \int_{\Omega} \vec{\pi} \cdot (\vec{q} + \mathbf{K} \cdot \vec{\nabla} \mu^f) d\Omega &= 0\end{aligned}\tag{2.20}$$

Here  $\varphi$ ,  $\vec{\psi}$  and  $\vec{\pi}$  variations in chemical potential, flux and velocity respectively. Then the mass balance is satisfied in a weak sense.

## 2.4 Prestress

The term *stress-free* was already mentioned. Now it will be more elaborated. The calculations start in the initial state ( $\Omega_i$ ), where the medium is already in equilibrium with an external salt concentration. Therefore an osmotic pressure exists and the solid matrix is stressed. Unfortunately, constitutive modeling describes the deformation from a stress-free state ( $\Omega_0$ ) to the current deformed state ( $\Omega$ ). Therefore the equations have to be rewritten with respect to the initial state. The relations are shown in Fig. 2.4. Two cases are described. Firstly, it is assumed that the initial state is the state after free swelling. Secondly, the case that the initial state is not the state after free swelling, but swelling was inhibited partially in one or two directions.

### 2.4.1 Free swelling

For the sake of simplicity the medium is assumed to be homogeneous in terms of fixed charge density, fluid volume fraction and elasticity in the stress-free state. The initial state

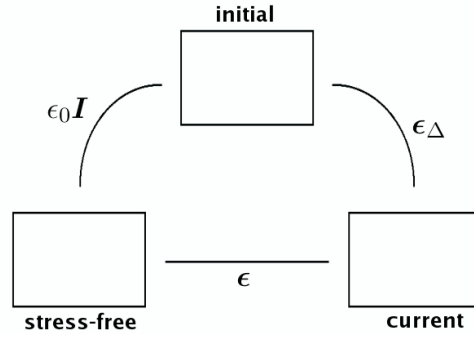


Figure 2.4: Schematic overview of stress-free, initial and current state.

of the medium as represented by the undeformed mesh is not the stress free state. Firstly, the initial state of the medium is assumed to be a free swelling state obtained through equilibration of the medium with an external salt solution. The specimen has grown from stress-free state to an equilibrium state with maximum stretching of the solid matrix. In this case the effective stress in the principal directions is equal to the osmotic pressure.

The osmotic pressure has induced a an initial volumetric deformation (depicted by strain  $\epsilon_i$ ) which is uniform w.r.t. the stress-free configuration, because the material is homogeneous and isotropic.

$$\epsilon_i = \epsilon_i \mathbf{I}. \quad (2.21)$$

Then in small strains the strain fields are additive (whereas in large deformations the deformations are multiplicative):

$$\epsilon = \epsilon_i \mathbf{I} + \epsilon_\Delta \quad (2.22)$$

Here  $\epsilon_\Delta$  is the strain from initial to current state (Fig. 2.4). Initially all the values are known and the sample is in equilibrium ( $\mu_{in}^f = \mu_{ex}^f = 0$ ) the next holds

$$\begin{aligned} c_i^{fc} &= \frac{\varphi_i^f c_0^{fc}}{(\varphi_i^f + 2\epsilon_i)}, \\ \Delta\pi(\epsilon) &= RT\Gamma_{in} \sqrt{(c_i^{fc})^2 + 4(c^{ex})^2} - 2\Gamma_{ex} c^{ex}, \\ \sigma(\epsilon) &= \Delta\pi(\epsilon) \mathbf{I}. \end{aligned} \quad (2.23)$$

Then the stress free fixed charge density is

$$c_0^{fc} = \frac{c_i^{fc} (\varphi_i^f + tr(\epsilon_i))}{\varphi_i^f} \quad (2.24)$$

In case of nonlinear material models the initial strain  $\epsilon_i$  is found by solving the equation above iteratively using a Newton-Rhapson procedure

$$\epsilon_i^{n+1} \approx \epsilon_i^n - \frac{\sigma_e(\epsilon_i^n) - \Delta\pi(\epsilon_i^n)}{\frac{\partial \sigma_e}{\partial \epsilon_i}(\epsilon_i^n) - \frac{\partial \Delta\pi}{\partial \epsilon_i}(\epsilon_i^n)} \quad (2.25)$$



Here  $\sigma_e = \sigma_{e,xx} = \sigma_{e,yy}$  holds. In this case the partial derivatives with respect to the strain components of interest are

$$\begin{aligned}\frac{\partial \sigma_e}{\partial \epsilon_i} &= 2\mu + 2\lambda \\ \frac{\partial \Delta \pi}{\partial \epsilon_i} &= \frac{\partial \Delta \pi}{\partial c^{fc}} \frac{\partial c^{fc}}{\partial \epsilon_i} \\ &= -\frac{RT\Gamma_{in}c^{fc}}{\sqrt{(c^{fc})^2 + 4(c^{ex})^2}} \frac{2c^{fc}}{(2\epsilon_i + \phi_i^f)}\end{aligned}\quad (2.26)$$

In the derivatives a factor 2 arises because  $\epsilon_i$  works in  $x$  and  $y$  direction. In this case the equations are simplified to

$$\epsilon_i = \frac{\Delta \pi}{2\mu + 2\lambda}, \quad \Delta \pi = RT\Gamma_{in} \sqrt{(c_i^{fc})^2 + 4(c^{ex})^2} - 2RT\Gamma_{ex}c^{ex}. \quad (2.27)$$

Finally, every cycle the strain  $\epsilon_\Delta$  is calculated from the displacement field. Then the initial strain is added to the calculated strain to get the strain w.r.t. stress-free state and this is inserted in the constitutive models.

## 2.4.2 Partially inhibited swelling

Secondly, the initial state is assumed to be a partially inhibited swelling state. An sample in a holder is in contact with an external salt solution. Subsequently, the sample wants to swell, but is inhibited partially by the holder. In this case the initial strain is less than in the case of free-swelling. Assuming the sample has an initial size of  $w_i \times h_i$ . Then the maximum swelling is

$$\begin{pmatrix} w \\ h \end{pmatrix} = \begin{pmatrix} w_i(1 + \epsilon_{ix}) \\ h_i(1 + \epsilon_{iy}) \end{pmatrix} \quad (2.28)$$

The corresponding stress is given by Eq. (2.29).

$$\begin{aligned}(2\mu + \lambda)\epsilon_{ix} + \lambda\epsilon_{iy} - \Delta \pi &= f_x \\ (2\mu + \lambda)\epsilon_{iy} + \lambda\epsilon_{ix} - \Delta \pi &= f_y\end{aligned}\quad (2.29)$$

Then when the initial strain in one direction is free, for instance in  $x$ -direction, then  $f_x = 0$ . When the strain is known in  $y$ -direction, the strain is calculated from

$$\epsilon_{ix} = \frac{(\Delta \pi - \lambda\epsilon_{iy})}{(2\mu + \lambda)} \quad (2.30)$$

The force  $f_y$  is calculated from the strains. When swelling is completely inhibited in  $y$ -direction, then  $\epsilon_{iy} = 0$  holds. Similarly, swelling in only  $y$ -direction is calculated.

### 2.4.3 Validation by swelling test

The implementation of the prestress is checked by inducing a small change in external salt concentration on a sample which is confined in a column which is open at the top. Then the deformation is given by

$$\boldsymbol{\epsilon} = \boldsymbol{\epsilon}_i + \delta\boldsymbol{\epsilon} = \epsilon_i \mathbf{I} + \delta\epsilon \vec{e}_2 \vec{e}_2. \quad (2.31)$$

For the stress in semi-ID holds

$$\sigma_{22} \approx \sigma_{e,22}(\boldsymbol{\epsilon}_i) + \frac{\partial \sigma_{e,22}}{\partial \epsilon_{22}}(\boldsymbol{\epsilon}_i) \delta\epsilon - \Delta\pi(c_i^{\text{ex}} + \delta c^{\text{ex}}, \boldsymbol{\epsilon}_i) - \frac{\partial \Delta\pi}{\partial \epsilon_{22}}(\boldsymbol{\epsilon}_i) \delta\epsilon \quad (2.32)$$

with

$$\begin{aligned} \sigma_{e,22} &= 2\mu\epsilon_{22} + \lambda(\epsilon_{11} + \epsilon_{22}) \\ c^{\text{fc}} &= \frac{c_0^{\text{fc}} \varphi_i^{\text{f}}}{\epsilon_{11} + \epsilon_{22} + \varphi_i^{\text{f}}} \\ \pi &= \sqrt{(c^{\text{fc}})^2 + 4(c^{\text{ex}} + \delta c)^2} \end{aligned} \quad (2.33)$$

and the partial derivatives to strain component of interest is

$$\begin{aligned} \frac{\partial \sigma_{e,22}}{\partial \epsilon_{22}} &= 2\mu + \lambda \\ \frac{\partial \Delta\pi}{\partial \epsilon_{22}} &= \frac{\partial \Delta\pi}{\partial c^{\text{fc}}} \frac{\partial c^{\text{fc}}}{\partial \epsilon_{22}} \\ &= - \frac{RT\Gamma_{in} c^{\text{fc}}}{\sqrt{(c^{\text{fc}})^2 + 4(c^{\text{ex}} + \delta c)^2}} \frac{c^{\text{fc}}}{(\epsilon_{11} + \epsilon_{22} + \varphi_i^{\text{f}})} \end{aligned} \quad (2.34)$$

Then

$$\delta\epsilon \approx - \frac{\sigma_{e,22}(\boldsymbol{\epsilon}_i) - \Delta\pi(c_i^{\text{ex}} + \delta c^{\text{ex}}, \boldsymbol{\epsilon}_i)}{\frac{\partial \sigma_{22}}{\partial \epsilon_{22}}(\boldsymbol{\epsilon}_i) - \frac{\partial \Delta\pi}{\partial \epsilon_{22}}(\boldsymbol{\epsilon}_i)} \quad (2.35)$$

The increase in height w.r.t. initial state is then given by

$$\text{swelling} = \delta h = h_i(\epsilon_i + \delta\epsilon) \quad (2.36)$$

The implementation of the bulk material models have been tested by the swelling test. A mesh is generated of eight elements over a height of 1 mm and each with width 0.5 mm. The bottom is fixed and in contact with the external salt concentration. The sides are constrained to only movement in the height. Then changing the external salt concentration at the bottom with  $\Delta c = 0.75\text{e-}6 \text{ mmol/mm}^3$ . A time step of 5 s is used. The material properties are given in table 2.1.

The change in salt concentration causes a change in chemical potential of  $\Delta\mu^{\text{f}} = 6.0\text{e-}3 \text{ MPa}$ , which results in a height change of  $-4.7\text{e-}3 \text{ mm}$ . The change in height approaches the analytical solution (Fig. 2.5).

**Table 2.1:** Material properties for verification for bulk material.

$R$	$=$	$8.3145$	$[\text{N mm}/\text{mmol K}]$	$T$	$=$	$298$	$[\text{K}]$
$E$	$=$	$0.9$	$[\text{MPa}]$	$\nu$	$=$	$0.20$	$[-]$
$\varphi_i^f$	$=$	$0.80$	$[-]$	$K$	$=$	$0.28\text{e-}3$	$[\text{mm}^4/\text{Ns}]$
$c^{\text{ex}}$	$=$	$0.15\text{e-}3$	$[\text{mmol}/\text{mm}^3]$	$c_i^{\text{fc}}$	$=$	$-0.2\text{e-}3$	$[\text{mmoleq}/\text{mm}^3]$

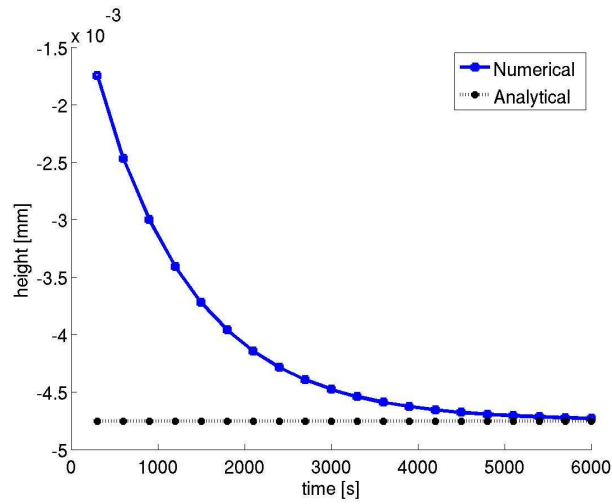


**Figure 2.5:** The change at the top of the column due to a change in salt concentration at the bottom in height. Dotted line is the analytical asymptotical height, the solid line denotes the transient numerical simulation.

## CHAPTER THREE

# Singularity solution for shear loading in saturated ionized porous media<sup>I</sup>.

---

<sup>I</sup> *Reproduced from:* F. Kraaijeveld, J. M. Huyghe, F. P. T. Baaijens, (2009). Singularity solution of osmoelasticity for verification of discontinuity simulations in soft tissues. *Journal of Biomech. Eng.* [51]

## Additional list of symbols

$\hat{*}$	$[[*]mm\ s]$	Laplace and Fourier transformed
$\bar{*}$	$[[*]mm]$	Fourier transformed
$C_0$	$[mmol/mm^3]$	Initial concentrations
$C_1$	$[mmol/mm^3]$	Deformation dependent change in concentrations
$d$	$[mm]$	Dislocation size
$E$	$[mm^2]$	Stress function
$erfc$	$[-]$	Complementary error function
$f(x)$	$[mm]$	Slip function
$k$	$[1/mm]$	Fourier parameter
$\kappa$	$[MPa]$	Bulk modulus
$L$	$[mm]$	Crack-tip $x$ -coordinate, $2L =$ crack length
$\mu^f$	$[MPa]$	Chemical potential w.r.t. initial state
$\bar{\mu}^f$	$[MPa]$	Chemical potential of the fluid
$S$	$[1/mm]$	Stress function
$s$	$[1/s]$	Laplace parameter

### 3.1 Introduction

Many diseases are associated with localized mechanical failure and damage of tissues. Examples are cartilage damage [110] and intervertebral disc herniation [111]. To determine tissue strength and local stresses, experimental studies (both clinical and animal) are supported by computational studies. Numerical methods have been developed to describe crack propagation in porous media [7,83,90]. Usually they are not verified by analytical solutions. The verification is often restricted to a qualitative comparison with experimental measurements. However, two uncertainties are involved in this comparison. One is whether the numerical model actually solves the equation it claims to solve. The other is whether the equation describes the physical reality of the experiment. In order to test separately the former question, an analytical solution is a must.

One important property of tissues is their swelling capacity. The presence of fixed charges in the tissues causes differences in ion concentrations with the surrounding fluid and therefore a Donnan-osmotic pressure [67,100]. Subsequently, the deformation of tissues depends not only on mechanical factors, but also on biochemical factors.

Osmotically swelling porous media have been modeled by many groups. Lanir [56] extended the Biot model [13] for incompressible constituents, namely the solid matrix and interstitial fluid, by including Donnan-osmotic pressure, but neglecting the influence of ion flow. Mow et al. [71] developed a biphasic model for articular cartilage. Lai et

al. [54] formulated a small deformations triphasic theory with ionic diffusion-convection included. Huyghe and Janssen [45] developed an electrochemomechanical model using four constituents. It has been implemented for finite deformations and verified for one-dimensional pressure tests by Frijns [35]. Van Loon et al. [102] implemented a 3D Finite Element model of the quadriphasic model. Van Meerveld [69] validated the quadriphasic model by analytical solutions.

The confined and unconfined compression test are common validation tools. Wilson et al. [108] compared the biphasic swelling model by Lanir [56] with the quadriphasic model by Huyghe et al. [44] and showed that the flow of ions indeed influences the pathway to equilibrium with the external fluid. Although the quadriphasic model is more realistic in transient behavior, Lanir's model is a reliable approximation for the modeling of ionized porous media, such as the intervertebral disc [92]. The last method is less complex and computationally less expensive than the former.

Some methods for validation have already been indicated above, however previous research has been restricted to continuous media. There are hardly any methods for validation of computational efforts of fractured porous media. Tests used in solid mechanics, like the three-point bending test or analytical solutions from linear fracture mechanics, are not suitable for porous media since the influence of fluid flow is not accounted for. crack-tip analysis and localization [8,58,62] have been topics of interest, but only give local trends.

Rice and Cleary developed an analytical solution for earthquake (shear faulting) predictions in 1976 [84], which has shown to predict aftershocks. Pure shearing mode of a crack is considered and special treatment of the crack is circumvented. Rice and Cleary's method uses Biot functions [14], which are similar to the Airy functions in solid linear fracture mechanics. However these functions can only be applied when there is compressibility in the model. Booker [15] calculated the dimensionless stress field along a shear fault for a fully saturated incompressible porous medium by decoupling the equations with stress functions according to McNamee and Gibson. [26,68,104] Rice [84] showed that both methods find the same result in the limiting case of incompressibility. The objective of this study is to establish a 2D method to study the performance of computational modeling of ionized porous media with cracks, namely an analytical solution suited for comparison with numerical calculations. In particular, the method by Booker [15,76] is generalized to ionized porous media.

## 3.2 Method

In this section the model by Lanir [56] is stated shortly. A perturbation on a homogeneous situation is considered, therefore the constitutive equations are linearized. The case of interest is given, after which the analytical solution is derived and numerical calculations are denoted.

### 3.2.1 Governing equations

Osmoelastic media have large negatively charged groups attached to the solid matrix. Counter charges are present in the fluid making the medium electrically neutral. Due to the fixed charges the total ion concentration inside the medium is higher than in the surrounding fluid. This excess of ion particles leads to an osmotic pressure difference, which causes swelling of the medium. Lanir's osmoelastic model [56] assumes that small ions are always in equilibrium with the external salt concentration. This means that ion contribution is neglected and the medium is described by two constituents only: the solid (s) and the fluid (f). The constituents are assumed to be incompressible. Infinitesimal deformations are assumed. The material is linear elastic, isothermal, isotropic, homogeneous and fully saturated. A full derivation is stated in chapter 2. Osmotic swelling is included by the introduction of the chemical potential of the fluid, which is a measure for the free energy of the fluid. The chemical potential of the fluid  $\bar{\mu}^f$  is defined per unit volume fluid and will be denoted by chemical potential:

$$\bar{\mu}^f = p - \pi. \quad (3.1)$$

with  $\pi$  the osmotic pressure and  $p$  the hydrostatic pressure. The osmotic pressure is determined by the empirical Van 't Hoff equation. This relation defines the osmotic pressure in terms of concentrations of free cations  $c^+$ , anions  $c^-$ , osmotic coefficient  $\Gamma$ , gas constant  $R$  and temperature  $T$ .

$$\pi = RT\Gamma(c^+ + c^-), \quad c^+ + c^- = \sqrt{(c^{fc})^2 + 4(c^{ex})^2} \quad (3.2)$$

This osmotic pressure holds outside as well as inside the medium, but outside the medium the fixed charge density  $c^{fc}$  is zero and the osmotic coefficient may be different. Electroneutrality holds, therefore the amount of negative charges are equal to the amount of positive charges:  $c^- + c^{fc} = c^+$ . Furthermore, the seepage flux  $\vec{q}$  follows Darcy's law in presence of concentration gradients. The total equations are given by (3.3).

$$\begin{array}{ll} \text{Momentum equations} & \vec{\nabla} \cdot \boldsymbol{\sigma} = \vec{\nabla} \cdot \boldsymbol{\sigma}_e - \vec{\nabla}(\mu^f + \pi) = \vec{0} \\ \text{Stress-strain relation} & \boldsymbol{\sigma}_e = 2\mu\boldsymbol{\epsilon} + \lambda \text{tr}(\boldsymbol{\epsilon})\mathbf{I} \\ \text{Mass balance} & \vec{\nabla} \cdot \frac{\partial \vec{u}}{\partial t} + \vec{\nabla} \cdot \vec{q} = 0 \\ \text{Darcy's law} & \vec{q} = -\mathbf{K} \cdot \vec{\nabla} \mu^f \\ \text{Swelling equation} & \pi = RT\Gamma \sqrt{(c^{fc})^2 + 4(c^{ex})^2} \\ \text{Fixed charge} & c^{fc} = \frac{\varphi_i^f c_0^{fc}}{\text{tr}(\boldsymbol{\epsilon}) + \varphi_i^f} \end{array} \quad (3.3)$$

The parameters  $\mu$  and  $\lambda = \kappa - 2\mu/3$  denote the Lamé constants.  $\nu$ ,  $\kappa$  and  $\mu$  are the Poisson's ratio, bulk modulus and shear modulus respectively. The parameter  $\lambda$  actually denotes the compressibility of the structure. The tensor  $\mathbf{K} = K\mathbf{I}$  denotes the permeability tensor and is assumed isotropic and constant in time and space.

The presence of ions fixed to the solid matrix results in prestress of the solid matrix at

initial condition. Constitutive relations hold at stress free configuration. Therefore  $\epsilon$  is the strain tensor, which includes the initial strain  $\epsilon_i$  and the deformation part such that  $\epsilon - \epsilon_i = 1/2\{\vec{\nabla}\vec{u} + (\vec{\nabla}\vec{u})^T\}$  holds. Similarly, the fixed charge density is calculated from the fixed charge density at stress-free configuration  $c_0^{\text{fc}}$  and initial volume fraction  $\varphi_i^f$ . Under assumption of small strains the swelling equation is linearized around the initial strain.

$$\begin{aligned}\pi &= \pi|_{\epsilon_i} + \frac{\partial\pi}{\partial\text{tr}(\epsilon)}|_{\epsilon_i}(\text{tr}(\epsilon) - \text{tr}(\epsilon_i)) \\ &= \pi|_{\epsilon_i} + \frac{\partial\pi}{\partial c^{\text{fc}}}\frac{\partial c^{\text{fc}}}{\partial\text{tr}(\epsilon)}|_{\epsilon_i}(\text{tr}(\epsilon) - \text{tr}(\epsilon_i)) \\ &= RT\Gamma\sqrt{(c_i^{\text{fc}})^2 + 4(c^{\text{ex}})^2} - RT\Gamma\frac{c_i^{\text{fc}}}{\sqrt{(c_i^{\text{fc}})^2 + 4(c^{\text{ex}})^2}}\frac{c_i^{\text{fc}}}{(\text{tr}(\epsilon_i) + \varphi_i^f)}(\text{tr}(\epsilon) - \text{tr}(\epsilon_i))\end{aligned}\quad (3.4)$$

with  $c_i^{\text{fc}}$  the initial fixed charge density and is used to compute the fixed charge density at stress-free state. For simplification we introduce the constants  $C_0 = \sqrt{(c_i^{\text{fc}})^2 + 4(c^{\text{ex}})^2}$ , the initial concentrations, and  $C_1 = \frac{(c_i^{\text{fc}})^2}{(\varphi_0^f + \text{tr}(\epsilon_i))C_0}$ , the change in concentrations due to unit strain. Then the osmotic pressure in terms of deformation becomes

$$\pi(\epsilon) = RT(C_0 - \text{tr}(\epsilon - \epsilon_i)C_1). \quad (3.5)$$

Subsequently, system (3.3) can be rewritten to

$$\begin{aligned}(\text{Momentum}) \quad & 2\mu\nabla^2\vec{u} + (c - 2\mu)\vec{\nabla}\text{tr}(\epsilon - \epsilon_i) - \vec{\nabla}\mu^f = 0 \\ (\text{Mass}) \quad & \frac{\partial\text{tr}(\epsilon - \epsilon_i)}{\partial t} - \vec{\nabla} \cdot (\mathbf{K}\vec{\nabla}\mu^f) = 0,\end{aligned}\quad (3.6)$$

with  $c = 2\mu + \lambda + RTC_1$ ,  $\mu^f = \bar{\mu}^f + RTC_0$ .

### 3.2.2 Singularity Case

In this section the problem is stated, that will be considered analytically and numerically. A rectangular piece of material is considered with a crack in the middle in the  $x, z$ -plane of length  $2L$ . The crack is closed. Fluid flow across the crack is allowed. Shear faulting is impulsively induced as a small displacement enforced on the upper and lower crack surface in opposite direction. This is shown in Fig. 3.1. The result is a steep increase of shear stress and fluid flow.

The upper crack surface is positioned at  $z = 0^+$  and the lower crack surface at  $z = 0^-$ . If we define  $\vec{u} = (u, w)^T$  as the displacement field, we can define the jump over the crack surface  $[u]$  as

$$[u](x, t) = u(x, 0^+, t) - u(x, 0^-, t). \quad (3.7)$$



Then the perturbation can mathematically be defined as

$$\begin{aligned} [u] &= f(x)\mathcal{H}(t) \\ f(x) &= d(\mathcal{H}(x-L) - \mathcal{H}(x+L)) = \begin{cases} 1 & \text{if } x \in [-L, L] \\ 0 & \text{otherwise} \end{cases} \end{aligned} \quad (3.8)$$

Here  $d$  denotes the magnitude of the dislocation and therefore the magnitude of the jump in shear direction.  $f(x)$  is called the slip function,  $\mathcal{H}$  is the Heaviside function. Since the crack is closed there is no jump in displacement in  $z$ -direction ( $[w] = 0$ ). Furthermore we have continuity of stresses ( $[\sigma_{\alpha\alpha}] = 0$ ,  $\alpha = x, z$ ).

We are interested in the shear stress at the crack surfaces, analytically and numerically.

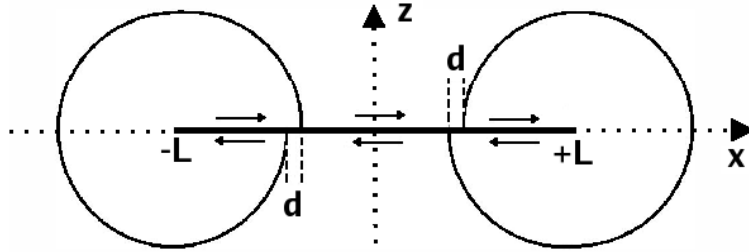


Figure 3.1: Two edge dislocations of magnitude  $d$  over crack length  $2L$ .

### 3.3 Analytical solution

The model (3.6) is strongly coupled. For the derivation of the analytical solution, decoupling of the total system of equations is needed. Following Booker [15], the solution is found using integral transformations of Laplace and Fourier. Except that the equations are not dimensionless, the derivations are not very different from Booker [15], because the osmolarity is lumped into the elasticity constant  $c$ . Discrepancies are pointed out.

#### 3.3.1 Decoupling

The system (3.6) can be decoupled by the introduction of stress functions (McNamee and Gibson [68]), appendix A. The stress function  $S(x, z, t)$  plays a role in the momentum equations and  $E(x, z, t)$  a larger role in the mass equation.

The stress function  $S(x, z, t)$  is introduced such that the function is harmonic, meaning  $\nabla^2 S = 0$  holds. The momentum equation is automatically satisfied, if for the chemical potential the next holds:

$$\mu^f = \text{ctr}(\epsilon) - 2\mu \frac{\partial S}{\partial z}. \quad (3.9)$$

The second stress function  $E(x, z, t)$  is introduced such that

$$\text{tr}(\epsilon - \epsilon_i) = \nabla^2 E. \quad (3.10)$$

Substituting Eqs. (3.9) and (3.10) in Eqs. (3.6), the system of equations is decoupled to the linear diffusion equations Eqs. (3.11) [68].

$$\begin{aligned} \nabla^2 S &= 0, \\ \nabla^2 \frac{\partial E}{\partial t} - cK \nabla^4 E &= 0. \end{aligned} \quad (3.11)$$

The number of equations has not been reduced, but the total system of equations, Eqs. (3.11), has been rewritten to decoupled partial differential equations, which are easier to solve. A complete overview is found in appendix A.

### 3.3.2 Governing equations in Laplace-Fourier domain

Any function can be split up into an even and an odd portion. McNamee and Gibson [68] only consider symmetric loading and therefore only use the symmetric part of Fourier transforms. To be able to consider more general cases, general Fourier and Laplace transformations are used (Booker [15]). Fourier (with variable  $k$ ) and Laplace (with variable  $s$ ) transformations are performed to reduce discontinuities to constant values (Appendix). Fourier transforms carry a tilde and depend on variables  $k$ ,  $z$  and  $t$ . Laplace-Fourier transforms carry a hat and depend on variables  $k$ ,  $z$  and  $s$ . Since a shear crack in the  $x, y$  plane is considered, the displacement jump will be over  $z = 0$  in the  $x$  direction, Fourier transformation along the crack is performed, thus over the  $x$  direction. See also appendix A. The forward Fourier transformation in  $x$  becomes (3.12).

$$\tilde{E}(k, z, t) = \int_{-\infty}^{\infty} E(x, z, t) e^{-ikx} dx. \quad (3.12)$$

Equivalently, the Laplace transformation is given by (3.13).

$$\hat{E}(k, z, s) = \int_0^{\infty} \tilde{E}(k, z, t) e^{-st} dt. \quad (3.13)$$

The result is a second order ordinary differential equation (ODE) for Laplace-Fourier transform  $\hat{S}$  of  $S$  and a fourth order ODE for Laplace-Fourier transform  $\hat{E}$  of  $E$ . The dependent and independent variables can be written in terms of the stress functions. From this, boundary conditions in the form of jump conditions are derived. In total the two boundary value problems (3.14) and (3.15) are found.

$$\begin{aligned} \left( \frac{\partial^2}{\partial z^2} - k^2 \right) \hat{S} &= 0 \\ [\hat{S}] &= 0 \quad \left[ \frac{\partial \hat{S}}{\partial z} \right] = \frac{ik}{s} \tilde{f}(k). \end{aligned} \quad (3.14)$$

and

$$\begin{aligned} (\frac{\partial^2}{\partial z^2} - k^2)(cK(\frac{\partial^2}{\partial z^2} - k^2) - s)\hat{E} &= 0, \\ [\hat{E}] &= \frac{-i}{ks}\tilde{f}(k) \quad [\frac{\partial \hat{E}}{\partial z}] = 0, \\ [\frac{\partial^2 \hat{E}}{\partial z^2}] &= -\frac{is}{cp}\tilde{f}(s)(c - 2\mu) \quad [\frac{\partial^3 \hat{E}}{\partial z^3}] = 0. \end{aligned} \quad (3.15)$$

with  $\tilde{f}(k)$  the Fourier transform of slip function  $f(x)$ :

$$\tilde{f}(k) = \int_{-L}^L de^{-ikx} dx = \frac{2d\sin(Lk)}{k}. \quad (3.16)$$

### 3.3.3 Solution

Previously the boundary value problem (BVP) in the Laplace-Fourier domain has been derived. This BVP is solved by splitting of the domain. The resulting solution is transformed from the Laplace domain to normal time domain. Since the interest lies in the shear stress around the crack-tip the equations are simplified by taking  $z = 0$ . Then back transformation from the Fourier domain to the normal  $x, z$  domain is performed. The inverse transform becomes (3.17).

$$E(x, z, t) = \frac{1}{2\pi} \int_{-\infty}^{\infty} \tilde{E}(k, z, t) e^{+ikx} dk \quad (3.17)$$

The inverse Laplace transformation is performed by the use of the mathematical formulas of Abramowitz and Stegun [1] and appendix A.

#### Solution in Laplace-Fourier domain

The solutions in Laplace-Fourier domain are derived by splitting the domain in an upper plane ( $z > 0$ :  $\hat{S}_+, \hat{E}_+$ ) and lower plane ( $z < 0$ :  $\hat{S}_-, \hat{E}_-$ ). Far from the crack the solution is not affected by the jump, so the solution has to approach zero for  $z \rightarrow \pm\infty$ . For stress function  $\hat{S}$  the general solution in the upper plane is given by  $\hat{S}_+ = \gamma_+ e^{-|k|z}$  and for lower plane  $\hat{S}_- = \gamma_- e^{+|k|z}$ . Then the jump condition reduces to

$$\begin{aligned} [\hat{S}] &= \lim_{z \downarrow 0} \hat{S} - \lim_{z \uparrow 0} \hat{S} \\ &= \hat{S}_+(k, 0, s) - \hat{S}_-(k, 0, s) = \gamma_+ - \gamma_-. \end{aligned} \quad (3.18)$$

Through linear algebra one can derive that the solution of (3.14) is given by (3.19)

$$\hat{S}(k, z, s) = \frac{-isign(k)}{2s} \tilde{f}(k) e^{-|k||z|}. \quad (3.19)$$

with  $sign(k) = \frac{k}{|k|}$ . A similar solution of the mass Eq. (3.15) is now determined and is given by (3.20)

$$\hat{E}(k, z, s) = -sign(z) \left\{ \left( \frac{ik\mu\tilde{f}(k)K}{s^2} + \frac{i\tilde{f}(k)}{2ks} \right) e^{-|k||z|} + \left( \frac{ik\mu\tilde{f}(k)K}{s^2} \right) e^{-\frac{1}{cK}\sqrt{k^2cK+s}|z|} \right\}, \quad (3.20)$$

It is unclear why Eqs. (3.19) and (3.20) and the general solutions are inconsistent with Booker [15], in between Eqs. (I2) and (I3).

### 3.3.4 Inverse transformation of the solution

The derived solutions are still in the Laplace-Fourier domain. Back transformations have to be performed. The solutions involve several terms dependent on Laplace variable  $s$ . The stress function  $\hat{S}$  contains only a factor  $1/s$  which becomes the Heaviside function by back transformation. So the inverse Laplace for stress function  $\hat{S}$  is

$$\tilde{S}(k, z, t) = -\frac{isign(k)}{2} \tilde{f}(k) e^{-|k||z|} \mathcal{H}(t). \quad (3.21)$$

The inverse Laplace of stress function  $\hat{E}$  is more difficult. It contains factors  $1/s$ ,  $1/s^2$  but also a factor  $e^{-\frac{|z|\sqrt{k^2cK+s}}{s^2}}$ . This latter term is not easy to invert. For deriving the inverse of the latter term we need to perform some mathematical manipulations, using the shift theorem and convolution theorem. This is done in the appendix. Again there are unexplainable differences with Booker [15], Eq. (A1). The result is

$$\tilde{E}(k, z, t) = -\frac{i\mu\tilde{f}(k)sign(z)}{2cK} \left\{ \left[ \frac{c}{\mu} + |z||k| \right] e^{-|k||z|} \mathcal{H}(t) - cK(k^2t + \frac{|z||k|}{2cK}) e^{|k||z|} erf c(\lambda^+) + cK(k^2t - \frac{|z||k|}{2cK}) e^{-|k||z|} erf c(\lambda^-) \right\}. \quad (3.22)$$

with  $\lambda^\pm = |k|\sqrt{cKt} \pm |z|/\sqrt{4cKt}$ . The shear stress is then given by

$$\begin{aligned} \tilde{\sigma}_{xz} &= 2\mu ik \left\{ \frac{\partial \tilde{E}}{\partial z} - z \frac{\partial \tilde{S}}{\partial z} \right\} \\ &= \frac{-\mu^2 \tilde{f}(k) |k|}{c} \left\{ \left[ -\left(1 - \frac{c}{\mu}\right) (1 - |z||k|) \right] e^{-|k||z|} \mathcal{H}(t) + cK(k^2t + \frac{|z||k|+1}{2cK}) e^{|k||z|} erf c(\lambda^+) + cK(k^2t - \frac{|z||k|-1}{2cK}) e^{-|k||z|} erf c(\lambda^-) - 2k^2 \frac{\sqrt{cKt}}{\sqrt{\pi}} e^{-(k^2cKt+z^2/(4cKt))} \right\} \end{aligned} \quad (3.23)$$

### 3.3.5 Shear stress

The expression (3.23) simplifies to (3.24) for  $z = 0$ , i.e. along the crack surface.

$$\begin{aligned} \tilde{\sigma}_{xz}|_{z=0} = & \frac{-\mu^2 \tilde{f}(k)|k|}{c} \left\{ \left[ -\left(1 - \frac{c}{\mu}\right) \right] \mathcal{H}(t) \right. \\ & \left. + (2k^2 c K t + 1) \operatorname{erfc}(|k| \sqrt{c K t}) - 2 \frac{\sqrt{k^2 c K t}}{\sqrt{\pi}} e^{-(k^2 c K t)} \right\} \end{aligned} \quad (3.24)$$

Back transformation from Fourier domain is performed by the use of the mathematical formulas of Abramowitz and Stegun [1], more specifically, the repeated integrals of the complementary error function (Appendix). Numerical Fourier integration is not possible since the integrand does not go to zero for increasing Fourier variable  $k$ .

The shear stress is given by Eq. (3.25)

$$\sigma_{xz}(x, 0, t) = -2\mu \frac{d\mathcal{H}(t)}{\pi(L^2 - x^2)} \left\{ L - \mu K F(x, t) \right\} \quad (3.25)$$

with

$$F(x, t) = 2t \left\{ \frac{(L-x)}{(L+x)^2} \left(1 - e^{-\frac{(L+x)^2}{4cKt}}\right) + \frac{(L+x)}{(L-x)^2} \left(1 - e^{-\frac{(L-x)^2}{4cKt}}\right) \right\} \quad (3.26)$$

The expansions (3.25) and (3.25) reduce to Eq. (16) of Booker if we replace expression  $c = 2\mu + \lambda + RTC_1$  by  $c = 2\mu + \lambda$ , i.e. if we neglect osmotic effects. When  $t \rightarrow \infty$ , the function  $F \rightarrow 0$  and the shear stress is at equilibrium. Using Taylor expansions, it is found that the shear stress at equilibrium is

$$\sigma_{xz}(x, 0, t_{equi}) = -\frac{2\mu d}{\pi(L^2 - x^2)} \left( L - \frac{\mu K L}{c K} \right). \quad (3.27)$$

The equilibrium stress also indicates a high singularity near the crack-tips. As expected the influence of the osmotic prestress is low on the shear stress at equilibrium, but is not negligible. Furthermore the osmotic prestress influences the behavior in time.

### 3.3.6 Chemical potential and flow

To find the distribution for the chemical potential and the flow, it is possible to numerically integrate Eq. (3.9), but it is also possible to derive an analytical expression for the chemical potential. The chemical potential does not only satisfies Eq. (3.9), but it also satisfies:

$$\left( \frac{\partial}{\partial t} - c K \nabla^2 \right) \mu^f = 2\mu \frac{\partial^2 S}{\partial z \partial t}. \quad (3.28)$$

This equation is found similar to Nur & Booker [76] for hydraulic pressure by substituting (3.9) into (3.11b) and using that  $S$  is harmonic. Since  $S$  is time independent the right side

of Eq. (3.28) is zero. Assuming almost circular diffusion from the crack-tip, the equation is solved using Hankel transformation [15,76] (appendix). The result is

$$\begin{aligned} \mu^f(x, z, t) = & \frac{\mu d z}{\pi} \left[ \frac{1}{(x-L)^2 + z^2} - \frac{1}{(x+L)^2 + z^2} \right] \\ & - \frac{\mu d z}{\pi} e^{-z^2/4cKt} \left[ \frac{e^{-(x-L)^2/4cKt}}{(x-L)^2 + z^2} - \frac{e^{-(x+L)^2/4cKt}}{(x+L)^2 + z^2} \right] \end{aligned} \quad (3.29)$$

From this we can derive the flow over the crack ( $\vec{n}$  vector normal to the crack,  $z = 0$ ):

$$\begin{aligned} \vec{q} \cdot \vec{n}(x, 0, t) = & -K \frac{\partial \mu^f}{\partial z}(x, 0, t) \\ = & -K \frac{\mu d}{\pi} \left[ \frac{1}{(x-L)^2} - \frac{1}{(x+L)^2} \right] \\ & + K \frac{\mu d}{\pi} \left[ \frac{e^{-(x-L)^2/4cKt}}{(x-L)^2} - \frac{e^{-(x+L)^2/4cKt}}{(x+L)^2} \right] \end{aligned} \quad (3.30)$$

and the flow along the crack ( $\vec{t}$  vector in direction of crack-tip  $x = +L$ ):

$$\vec{q} \cdot \vec{t}|_{z=0} = -K \frac{\partial \mu^f}{\partial x}(x, 0, t) = 0 \quad (3.31)$$

### 3.4 Numerical example

For simulations Finite Element package ABAQUS 6.4-5 has been used. Lanir's model is implemented by Wilson [109], but with a Neo-Hookean material law. This law reduces to the material as used here for small strains. The variational description is given in chapter 2. Quadrilateral linear elements are used. The mesh is given in Figs. 3.2 and 3.3. A crack is created bluntly by tying two meshes together except for the crack and crack-tips. A contact condition is imposed between the crack surfaces. The crack-tips are not restricted in  $x$ -direction in order to have a pure symmetric reaction left and right from the crack-tip. This also implies that for boundary conditions a pure Heaviside function cannot be imposed, but the heaviside function is approximated by change over a length  $\Delta x$ , i.e. the length of the unconstraint interval around the crack-tip. This way a piece of medium of size 8 mm  $\times$  6 mm with a fixed charge density of  $c_0^{fc} = 0.2$  mmol/ml, a bulk modulus of  $\kappa = 0.5$  MPa and a shear modulus of  $\mu = 0.375$  MPa is created. These properties approximate the properties of disc tissue [102,111]. The size is chosen sufficiently large that boundaries have no effect on the result using Eq. (3.29).

All boundaries are restricted in normal behavior, i.e. left side is restricted in  $x$ -direction, etc.. The result is that the crack location and length does not change under osmotic loading. The medium is in equilibrium with an external salt concentration. This means that at all boundaries fluid flow is free and  $\mu_{in}^f = \mu_{ex}^f$  holds, i.e. the chemical potential of the fluid in the medium at the boundaries are equal to the external chemical potential. To prevent the crack from opening, the nodes at the crack surface are fixed in  $z$ -direction. This is in agreement with the jump condition  $[w] = [u_z] = 0$ . After letting the medium reach equilibrium, an impulsive shear load is applied on the crack surfaces. A displacement smaller than the width of one element is imposed on the crack surfaces, namely a

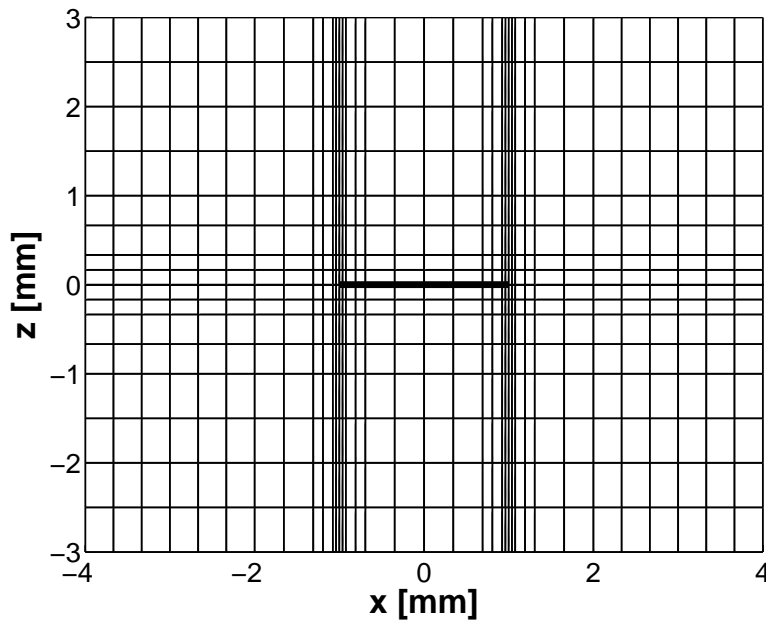


**Figure 3.2:** Mesh creation for 576 elements. Mesh is refined towards the areas of interest: the crack-tips.

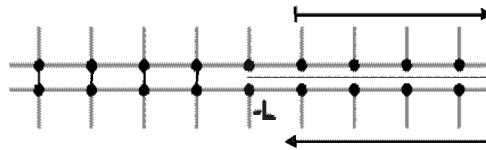


**Figure 3.3:** Close up mesh at crack-tip  $x = -L$ . Nodes are tied outside the crack ( $|x| > 1$ ). Contact is defined on the crack surfaces  $x < |L|$ ,  $z = 0^\pm$ . The crack-tips  $x = \pm L$  are free.

displacement of a magnitude of  $d/2$  for the upper crack surface in positive  $x$ -direction and lower surface in opposite direction.

Similar as in space, it is not possible to impose an impulsive loading in time, but it is approximated by changing the conditions over a time length  $\Delta t$ . The influence of time step is studied. After that, the calculations are run until steady state is reached. Shear stress in the nodes are calculated by averaging over the neighboring integration points. The change in shear stress is calculated by deducting the initial shear stress distribution from the state of interest. The effect of spatial discretization size is studied by considering three meshes from coarse to fine of mesh size 144 elements, 576 elements and 2304 elements. The parameters are given in table 3.1.

**Table 3.1:** Model parameters for numerical and analytical models.

$R$	$= 8.3145$	[N mm/mmol K]	$T$	$= 298$	[K]
$\mu$	$= 0.375$	[MPa]	$\nu$	$= 0.2$	[-]
$\kappa$	$= 0.5$	[MPa]			
$\varphi_i^f$	$= 0.8$	[-]	$K$	$= 0.28e-3$	[mm <sup>4</sup> /Ns]
$c_{ex}$	$= 0.15e-3$	[mmol/mm <sup>3</sup> ]	$c_i^{fc}$	$= -0.2e-3$	[mmoleq/mm <sup>3</sup> ]
$d$	$= 0.004$	[mm]	$L$	$= 1.0$	[mm]

## 3.5 Results

As the result of impulsive loading the medium reacts as if incompressible leading to high shear stress. Then the fluid flow starts and relaxation takes place. Consolidation takes place. This is seen in the Eq. (3.25), but also Fig. 3.4.

The dislocation causes compression above the crack and expansion underneath the crack

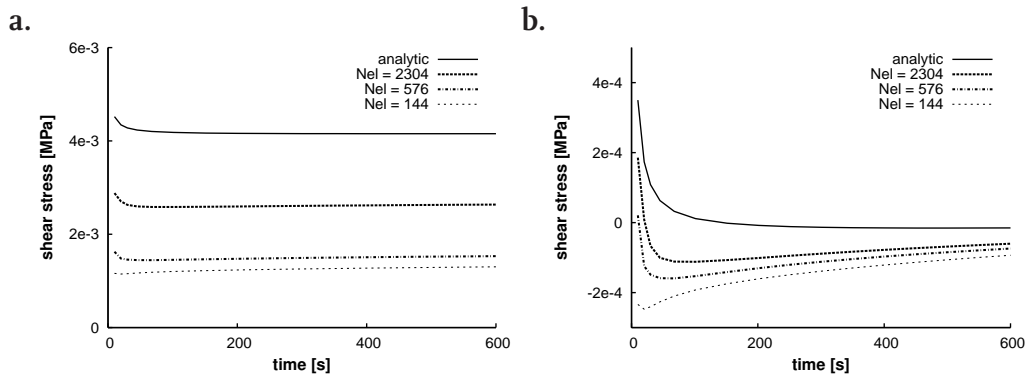


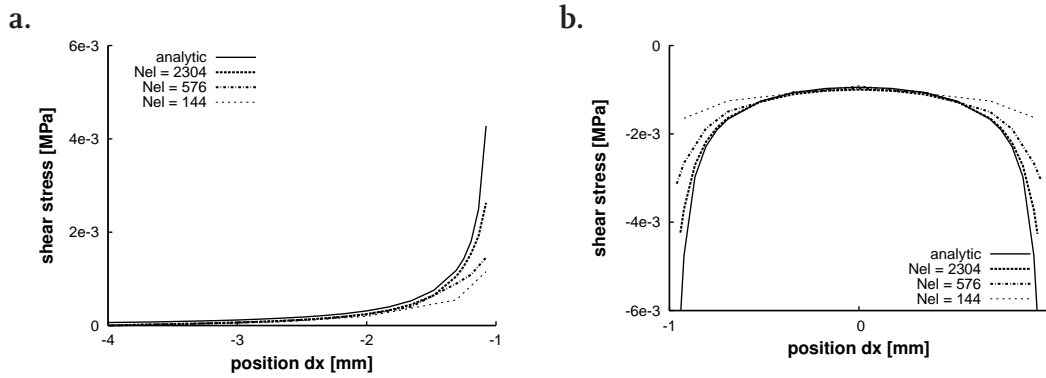
**Figure 3.4:** Consolidation for different calculations at  $x = 1.0769$  mm. With refinement, the time dependent behavior of the analytical solution is better approximated except for an offset. **a.** shows the data with the offset, **b.** without the offset.

for  $x > 0$  and viceversa for  $x < 0$ . The normal stresses are antisymmetric with respect to the  $z$ -axis. The shear stress is symmetric with respect to the  $z$ -axis and anti-symmetric with respect to the crack-tips (Fig. 3.5). The values left and right of the crack-tip are equal in magnitude (not sign), also for the numerical models. In the crack-tips the shear stress undergoes a high singularity ( $x = \pm 1$ ).

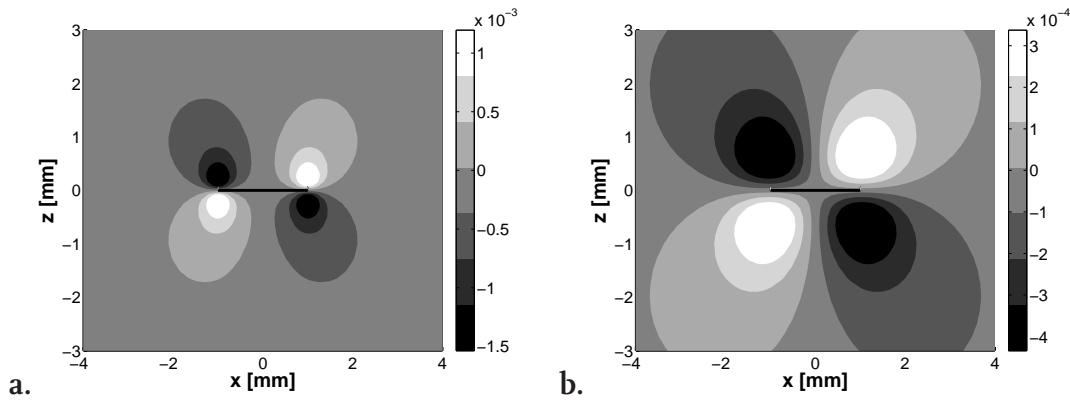
The dislocation causes for  $x > 0$  compression above the crack and expansion underneath the crack. The normal stresses and the chemical potential are antisymmetric to  $z$ -axis and  $x$ -axis. In Figs. 3.6a and 3.6b it is seen that at the crack-tips the compression produces a positive chemical potential and extension produces a negative chemical potential. Fluid flow is induced causing relaxation and spreading of the chemical potential.

Figure 3.7 shows the analytical flow and numerical approximations in plane of the crack. The dislocation causes flow over the crack surface and that increases towards the crack-





**Figure 3.5:** Shear stress distribution at  $t = 30.0$  s. A high singularity is seen in all cases. The stresses left (a.) and right (b.) from the crack-tip, are equal in magnitude. The numerical shear stress converges to the analytical shear stress upon refinement, except in vicinity of the crack-tips  $x = \pm 1$ .



**Figure 3.6:** Analytically calculated distribution of chemical potential (in MPa) at a.  $t = 30.0$  s and b. at  $t = 301.1$  s. Crack is indicated by solid line. Fields of high and low chemical potential values are seen in regions of compression and extension respectively. The chemical potential relaxes and diffuses over time.

tips.

To approximate the impulsive loading of the crack, a steep change in displacement was applied over a time length of  $\Delta t$  and over a length interval  $1 \pm \Delta x$ . There is no difference in result between  $\Delta t = 0.1$  s and  $\Delta t = 0.01$  s. The influence of the loading gradient is subsequently considered negligible for all calculations. Similar in space, the Heaviside was approximated by unconstrained nodes at the crack, Fig. 3.3, over an interval  $\Delta x$  around the crack-tip. In Fig. 3.8 it is seen that refinement overall increased accuracy and not so much the length of the unconstrained crack-tip region.

When the time distribution, as in Figs. 3.4 and 3.8, is considered more closely, it is clear that the numerical model has not reached equilibrium yet. Using that the stress at equilibrium satisfies Eq. (3.27) it is found that the analytical also has not reached equilibrium yet.

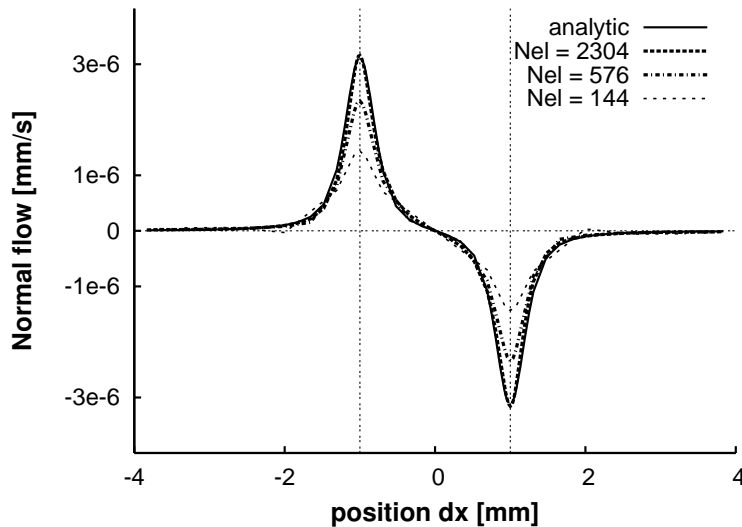


**Figure 3.7:** The numerically and analytically calculated flow over the crack surface (in mm/s) at  $t = 30.0$  s. With refinement the numerically calculated flow converges to the analytical flow.

The osmotic prestress influences the initial shear stress as the result of incompressible behavior, but it influences the time to equilibrium and shear stress at equilibrium too. A decrease in osmotic pressure causes a decrease in shear stress, Fig. 3.9. Numerically this effect is smaller than analytically.

Numerical and analytical chemical potential distributions match very well in distribution. Analytically, at time 30.0 s maximum and minimum chemical potential of  $\pm 1.50e-3$  MPa is found while numerically the chemical potential is a bit higher:  $\pm 1.58e-3$  MPa for 2304 elements and  $\pm 1.61e-3$  MPa for 576 elements. At time 301.1 s these values are  $\pm 4.18e-4$  MPa for the analytical minima and maxima and  $\pm 3.88e-4$  MPa for the numerical minima and maxima for 2304 elements and  $\pm 4.04e-4$  MPa for 576 elements.

## 3.6 Discussion

In this research an analytical solution for cracks in swelling porous media has been derived by considering a displacement driven dislocation. The dislocation is impulsively induced. The analytical solution has been derived by means of stress functions and Fourier and Laplace transformations. The solution is derived with physical units (i.e. not dimensionless) and can also be used when there is no osmotic swelling.

In the derivation of the analytical solution some important assumptions were made. A small perturbation is considered, therefore  $d \ll L$  must hold. The perturbation solution is additive to the initial state by linearization. This means that the initial state has a low influence. The jump over the  $z = 0$ -plane of the dependent and independent variables are the boundary conditions over the crack. The displacement jump in shear direction is

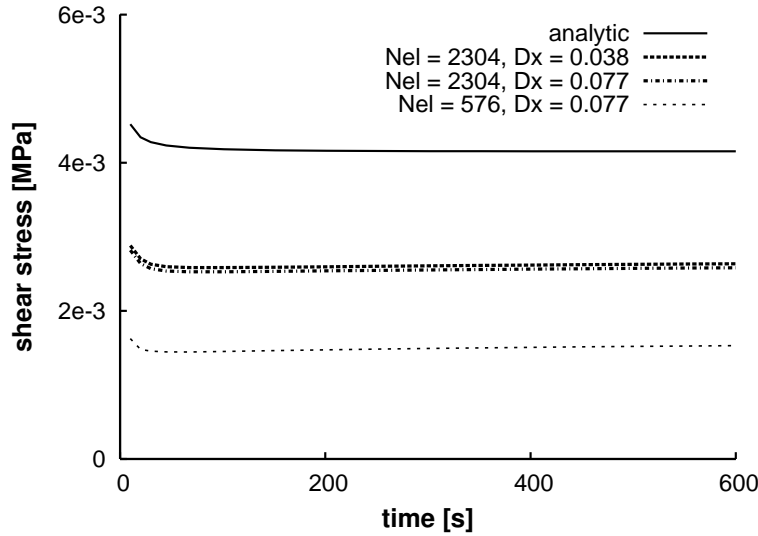


**Figure 3.8:** Consolidation of shear stress at  $x = 1.0769$  mm. Refinement has a much larger effect than increasing interval length for spatial loading  $\Delta x$  on the equilibrium stress.

given, other variables are continuous. This means that the shear stress response below and under the crack are symmetrical in the  $z = 0$  plane or values are zero on the plane. Another assumption is that far away from the crack the influence of the displacement at the crack is negligible.

In general the decoupling method works well and can be used to consider other problems. The restriction of this method lies in the boundary conditions. Using these decoupled equations in Fourier domain, it is not possible to calculate the shear stress distribution in case of a semi-infinite crack. A Wiener-Hopf procedure can not be applied like models decoupled in drained and undrained variables [8]. Back transformation by numerical integration cannot be applied either.

The shear stress distribution in plane of the crack and the distribution in chemical potential have been derived in full dimensions including the osmotic prestress. From these solutions it is possible to derive a few properties. The shear stress undergoes a singularity of the order  $\mathcal{O}(\frac{1}{(L^2-x^2)})$  and relaxes exponentially (Eq. (3.25)), but the high singularity at the crack-tips does not vanish. The chemical potential distribution is not singular, see Eq. (3.29). In the crack the chemical potential is zero. In time the chemical potential decreases exponentially, but also the extremes of the pressure field move away from the crack-tips in time parallel to the  $z$ -axis (the factor  $e^{-z^2/4cKt}$ ). The tangential flow along the crack is zero. The normal flow in the  $z = 0$ -plane, Eq. (3.30), has a singularity of the order  $\mathcal{O}(\frac{1}{(L^2-x^2)})$ . The flow is positive for  $x > 0$  (upwards) and negative for  $x < 0$  (downwards), and zero for  $x = 0$ .

The effect of parameters is apparent from Eq. (3.25)). Firstly, the stress is linearly dependent on the magnitude of the dislocation, but nonlinearly dependent on the length of the crack. The longer the crack the lower the shear stress produced by the dislocation, also in equilibrium. In general the term  $\mu KF(x, t)$  is initially not small, but decreases in time to

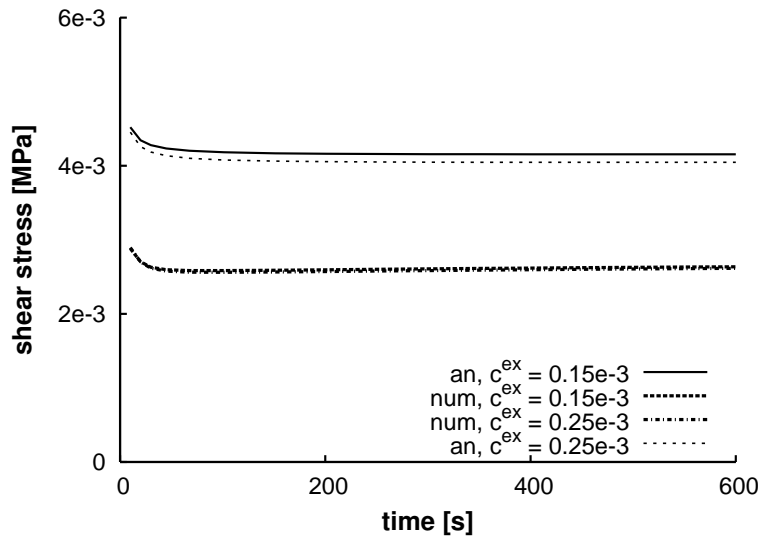


**Figure 3.9:** Shear stress evolution at  $x = 1.0769$  mm with  $c_{ex}$  in  $\text{mmol}/\text{mm}^3$ . A decrease in prestress decreases the shear stress analytically and numerically, but increases the time to equilibrium. The analytical change in shear stress is larger than the numerical change, but smaller than the difference between analytical and numerical results.

$\mu\text{L}/c$ .

Secondly, higher Lamé constants result in increasing shear stress. The shear stress distribution is initially nonlinear in the shear modulus but in equilibrium it is linear. A higher Lamé constant  $\lambda$  results in faster relaxation.

Finally, the response depends on external and internal ion concentrations. Increasing the external salt concentration decreases the prestress and decreases the shear stress response to the dislocation ( $C1$  decreases and therefore  $c$  decreases). The relaxation time is increased. Increasing the fixed charge concentration has the opposite reaction ( $c$  increases).

The analytical solution points out weaknesses of the numerical model and calculations. The numerical modeling has been validated by confined and unconfined pressure tests [109]. From the expression for the chemical potential Eq. (3.29) the mesh size was determined such that the chemical potential is zero at the boundaries for the time frame of interest. The boundary conditions have little influence on the local shear stress distribution as long as the shear stress is constant around the area of interest. While the analytical solution assumes an unrestricted domain, numerically the domain is restricted. The restriction of the domain does have an influence on the solution, but comparison with a domain twice as large showed the influence is negligible. The differences of the numerical and analytical maxima and minima in the distribution of the chemical potential are the result of the use of a coarse mesh away from the area of interest. Furthermore Fig. 3.7 shows that the finest mesh can capture the fluid flow very well.

Keeping the crack-tip node unrestricted has led to a perfectly anti-symmetrical shear-stress just as the analytical results, i.e. the shear stress left and right from the crack-tips are equal. Since the influence of time and spatial interval for reaching maximum values

is low (Fig. 3.8), it is reasonable to use this unrestricted node. Furthermore continuity in stresses holds, the stresses at the lower crack surface are equal to those at the upper crack surface.

The numerical model approximates the analytical solution very well, but in the very vicinity of the crack-tips the shear stress is underestimated by a factor 2, Fig. 3.5. The time dependency of the numerical results matches the analytical solution very well for the finest mesh except for an offset at a point ahead of the crack-tip and close to the singularity (3.4). It is found that the time behavior is even better at the current crack surface. Considering the steepness of the spatial curve close to the singularity (Fig. 3.5), a slight offset in horizontal plane would cause a large mismatch in Fig. 3.4. Therefore the offset in Fig. 3.4 should be interpreted as a minute horizontal shift of the numerical curves of Fig. 3.5 towards the singularity.

The importance of a good mesh and crack insertion is further emphasized when the effect of the osmotic prestress is considered, Fig. 3.9. The offset in the numerical calculations is larger than the change in shear stress perturbation as result of the change in osmotic prestress in absolute sense. The offset due to the horizontal shift of the numerical curve towards the singularity dominates other effects. In general the influence of osmotic prestress for shearing mode is expected to be low, but is not negligible, Eq. (3.27). These effects could be overlooked if cracks are not treated correctly. A greater influence of the osmotic prestress is expected when considering the opening mode [III]. The analytical solution is a benchmark for the performance of numerical models with singularities and is a step towards arbitrary loading.

## CHAPTER FOUR

# **Strong discontinuity model for the fluid for shear loading in saturated ionized porous media<sup>I</sup>.**

---

<sup>I</sup> *Reproduced from:* F. Kraaijeveld, J. M. Huyghe, J. J. C. Remmers, R. de Borst, F. P. T. Baaijens, (2009). Shear fracture in osmoelastic fully saturated media: a mesh-independent model. *Engng. Frac. Mech.* [53]

## 4.1 Introduction

The mechanical causes of intervertebral disc (IVD) degeneration and herniation are poorly known [100]. The presence of fixed charges in the collagen network of tissues causes differences in ion concentrations with the surrounding fluid and therefore Donnan-osmotic pressure. This gives the IVD its prestress and its protective nature against crack growth. During degeneration a loss of fixed charges and hydration occurs. Understanding and prediction of failure of the IVD asks for the combination of experiments and computational models. Although finite element models of failure of the disc exist, the modeling has usually been restricted to stress analysis studies [50,74] or inserting contact elements as a model for lesions [60]. Accurate modeling of the crack will improve the predictive behavior of those models. This is not only an issue in biomechanics, but there is a need for a good model for fracture in ionized porous media to study geotechnical issues as well.

In this thesis a macro fracture in a continuum is of interest and therefore a discrete fracture model is used. Herniation is not perfectly brittle. The macro-crack is preceded by a zone with small-scale yielding and micro-cracking (Fig. 1.7). This process zone is simulated by a cohesive zone model, where the decrease of strength in the zone is lumped into a discrete line (in 2D modeling) and a stress-displacement relationship across this line. There are several discrete methods available for simulating the cohesive zone.

Barenblatt [10], Dugdale [30] and Hillerborg [40], were the pioneers to cohesive fracture in solids. This cohesive zone can be introduced as a geometrical entity using interface elements at all element boundaries [112] or in the path of interest [86,88]. This method is suitable if the crack path is known a priori, since it requires alignment of the element with the crack path a priori. A downside is that a high dummy stiffness is needed to prevent deformation in the interface before initiation and the introduction of length scales, but the hottest is mesh-dependency [23].

Alternatively, remeshing procedures [20] can be used to explicitly model the discontinuity. Based on this concept fracture in porous media has been investigated by Boone [16] and Schrefler and followers [89]. Strong discontinuities in the porous media framework have been introduced to study strain localization, i.e. shear bands.

Strong discontinuities are considered the final failure mechanism within localization problems. Larsson et al. [58] introduced a discontinuity in the fluid by a regularized Delta Dirac function. Armero et al. [7] assumes only discontinuous displacement. Steinmann [97] extended these embedded discontinuity models based on enhanced strains concepts, without the restriction of locally drained or undrained behavior by a new interface law based on Darcy's law.

To eliminate mesh dependency and artificial length scales, Babuska and Melenk introduced a discontinuity in a mesh free way by adding an enhanced field on top of the standard displacement (and pressure) field, in this case by a Heaviside, function using the partition of unity property of the Finite Element shape functions [9]. The number of degrees of freedom at the nodes whose support is crossed by a discontinuity,

is increased. Therefore no new nodes are added during propagation. Belytschko [12] introduced this method for a solid together with an asymptotic enhancement of the displacement field at the crack-tip. Wells et al. [107] introduced cohesive segments within the finite elements followed by Remmers et al. [80] who modeled the crack not as a single entity, but as a collection of overlapping cohesive segments. A practical benefit of the method is that standard discretization is used and crack propagation is independent of the discretization. A downside of this method is that it is difficult to implement in commercial codes.

Gasser and Holzapfel have applied the partition of unity method to tissues, namely the fracture of bone [37] and dissection of an aorta wall [36]. Nevertheless, fluid flow in the tissue was not accounted for. Réthoré et al. [82] considered shear banding by using partition of unity with crack-tip singularity for the solid phase and without crack-tip singularity for the fluid phase, suggesting a discontinuity in the pressure field in case of shearing, combined with Darcy's law similar to the enhanced strains models. A diaphragm with low permeability at the discontinuity is assumed.

The above work has shown that the partition of unity approach is promising for crack propagation in porous media. Much discussion is still on the treatment of the fluid phase, because there is no comparison to a benchmark solution. In this research we emphasize on the inclusion of osmotic effects and insist on a more physical way of relating discontinuity deformation and fluid flow. Unlike earlier approaches, this approach is tested by comparison to an analytical solution of a two-edge dislocation [51].

For the modeling of the osmoelastic behavior of the material, Lanir's plane strain model [56] for small deformations is used. Lanir assumes incompressible constituents, namely the solid matrix and interstitial fluid, and neglects the influence of ion flow. Lanir's model coincides with Biot's model if osmotic effects are neglected. This model is implemented with the cohesive segments model by Remmers et al. [24,80] for the solid phase assuming quasi-brittle crack growth. In the fluid phase a pressure discontinuity is introduced similarly to the displacement discontinuity in the solid phase, but the discontinuity relaxes due to a permeability across the interface which alters depending on the time since opening.

## 4.2 Governing equations

The governing equations consist of equations for the bulk and for the discontinuity, dominated by mass balance, momentum balance and constitutive behavior. Figure 4.1 shows a body  $\Omega$  with external boundary  $\Gamma$  with a traction force on  $\Gamma_t$  and fluid supply on  $\Gamma_f$ , with  $\vec{n}$  the normal unit vector on the boundary  $\Gamma$  directed outwards. The body is cut by a discontinuity  $\Gamma_d$  in two domains,  $\Omega^+$  and  $\Omega^-$ . The normal of the discontinuity  $\vec{n}_\Gamma$  is directed towards  $\Omega^+$ .



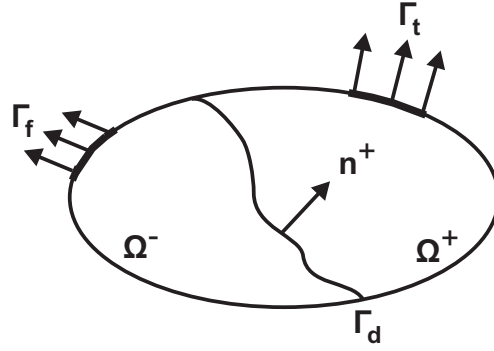


**Figure 4.1:** Schematic representation of the body  $\Omega$ : the two parts are  $\Omega^+$  and  $\Omega^-$ , separated by crack  $\Gamma_d$ . A traction force holds on  $\Gamma_t$  and fluid supply at  $\Gamma_f$ .

### 4.2.1 Bulk behavior

For osmoelastic media have large negatively charged groups fixed to the solid matrix, the fixed charge. Counter charges are present in the fluid for electro-neutrality. Due to the fixed charges the total ion concentration inside the medium is higher than in the surrounding fluid. This leads to an osmotic pressure difference and therefore swelling of the medium. To simulate osmotically swelling porous media Lanir's model is used in plane strain (chapter 2) and is repeated here shortly. Lanir's osmoelastic model [56] assumes that free ions are always in equilibrium with the external salt concentration. Ion contribution is therefore neglected and the medium is described by two constituents only: the solid (s) and the fluid (f). The constituents are assumed to be incompressible. The material is assumed linear-elastic, isothermal, isotropic, homogeneous and fully saturated. The presence of the fixed charge causes a deformation dependent pressure difference between the sample and surrounding fluid. Osmotic pressure is determined by the empirical Van 't Hoff equation. Van 't Hoff relation defines the osmotic pressure in terms of concentrations of free cations,  $c^+$ , anions  $c^-$ , gas constant  $R$  and temperature  $T$  and depends indirectly on the fixed charge density  $c^{fc}$  and the external salt concentration  $c^{ex}$ .

$$\Delta\pi = \pi - \pi^{ex} = RT\sqrt{(c^{fc})^2 + 4(c^{ex})^2} - 2RTc^{ex} \quad (4.1)$$

Not hydrostatic pressure, but the chemical potential of the fluid is the driving force for fluid flow. Chemical potential is a measure for the free energy of the fluid. The chemical potential of the fluid  $\mu^f$  is defined per unit volume fluid

$$\bar{\mu}^f = p - \pi. \quad (4.2)$$

with  $\pi$  the osmotic pressure and  $p$  the hydrostatic pressure. The osmotic pressure is determined by the empirical Van 't Hoff equation. Van 't Hoff relation defines the osmotic pressure in terms of concentrations of free cations  $c^+$ , anions  $c^-$ , gas constant  $R$  and temperature  $T$ .

$$\pi = RT(c^+ + c^-), \quad c^+ + c^- = \sqrt{(c^{fc})^2 + 4(c^{ex})^2} \quad (4.3)$$

This osmotic pressure holds outside as well as inside the medium, but outside the medium the fixed charge density  $c^{\text{fc}}$  is zero and the osmotic coefficient may be different. Electro-neutrality holds, therefore the amount of negative charges are equal to the amount of positive charges:  $c^- + c^{\text{fc}} = c^+$ . Furthermore we introduce  $\Delta\pi = \pi - \pi^{\text{ex}}$ . The seepage flux  $\vec{q}$  follows Darcy's law in presence of concentration gradients. The total equations are given by Eqs. (4.4)-(4.9).

$$\text{Momentum equations} \quad \vec{\nabla} \cdot \boldsymbol{\sigma} = \vec{\nabla} \cdot \boldsymbol{\sigma}_e - \vec{\nabla}(\mu^{\text{f}} + \Delta\pi) = \vec{0} \quad (4.4)$$

$$\text{Stress-strain relation} \quad \boldsymbol{\sigma}_e = 2\mu\boldsymbol{\epsilon} + \lambda \text{tr}(\boldsymbol{\epsilon})\mathbf{I} \quad (4.5)$$

$$\text{Mass balance} \quad \vec{\nabla} \cdot \frac{\partial \vec{u}}{\partial t} + \vec{\nabla} \cdot \vec{q} = 0 \quad (4.6)$$

$$\text{Darcy's law} \quad \vec{q} = -\mathbf{K} \cdot \vec{\nabla} \mu^{\text{f}} \quad (4.7)$$

$$\text{Swelling equation} \quad \Delta\pi = RT \sqrt{(c^{\text{fc}})^2 + 4(c^{\text{ex}})^2} - 2RTc^{\text{ex}} \quad (4.8)$$

$$\text{Fixed charge} \quad c^{\text{fc}} = \frac{\varphi_i^{\text{f}} c_0^{\text{fc}}}{\text{tr}(\boldsymbol{\epsilon}) + \varphi_i^{\text{f}}} \quad (4.9)$$

The parameters  $\mu = \frac{E}{2(1+\nu)}$  and  $\lambda = \mu \frac{2\nu}{(1-2\nu)}$  are the Lamé constants.  $E$ ,  $\nu$  and  $\mu$  are the Young's modulus, Poisson's ratio, bulk modulus and shear modulus respectively. The tensor  $\mathbf{K} = KI$  denotes the permeability tensor and is assumed isotropic and constant in time and space.

The presence of ions fixed to the solid matrix results in prestress of the solid matrix at initial condition. Constitutive relation Eq. (4.4) holds relative to stress free configuration. Therefore,  $\boldsymbol{\epsilon}$  is the strain tensor is separated in an initial strain  $\boldsymbol{\epsilon}_i$  and the deformation from initial to current state,  $\boldsymbol{\epsilon}_\Delta = \boldsymbol{\epsilon} - \boldsymbol{\epsilon}_i = \vec{\nabla}^s \vec{u} = 1/2\{\vec{\nabla} \vec{u} + (\vec{\nabla} \vec{u})^T\}$ . Similarly, the fixed charge density is calculated from the fixed charge density at stress-free configuration  $c_0^{\text{fc}}$  and initial volume fraction  $\varphi_i^{\text{f}}$ . Equations (4.4)-(4.8) are reduced to (4.10).

$$\begin{aligned} \frac{\partial \text{tr}(\boldsymbol{\epsilon})}{\partial t} - \vec{\nabla}^s \cdot (\mathbf{K} \cdot \vec{\nabla}^s \mu^{\text{f}}) &= 0 \\ 2\mu \vec{\nabla}^s \cdot \boldsymbol{\epsilon} + \lambda \vec{\nabla}^s \text{tr}(\boldsymbol{\epsilon}) - \vec{\nabla}^s(\mu^{\text{f}} + \Delta\pi(\boldsymbol{\epsilon})) &= 0. \end{aligned} \quad (4.10)$$

The boundary conditions and initial conditions are given by ( $\Gamma_t \cup \Gamma_u = \Gamma$ ,  $\Gamma_t \cap \Gamma_u = \emptyset$  and  $\Gamma_f \cup \Gamma_\mu = \Gamma$ ,  $\Gamma_f \cap \Gamma_\mu = \emptyset$ )

$$\begin{aligned} \vec{u}(\vec{x}, 0) &= \vec{u}_0(\vec{x}), & \vec{x} &\in \Omega, & \mu^{\text{f}}(\vec{x}, 0) &= \mu_0^{\text{f}}(\vec{x}), & \vec{x} &\in \Omega, \\ \vec{u}(\vec{x}, t) &= \vec{u}_\gamma(\vec{x}, t), & \vec{x} &\in \Gamma_u, & \mu^{\text{f}}(\vec{x}, t) &= \mu_\gamma^{\text{f}}(\vec{x}, t), & \vec{x} &\in \Gamma_\mu, \\ (\boldsymbol{\sigma}_e - (\mu^{\text{f}} + \Delta\pi)\mathbf{I}) \cdot \vec{n} &= \vec{t}_t(\vec{x}, t), & \vec{x} &\in \Gamma_t & \vec{q} \cdot \vec{n} &= f_f(\vec{x}, t), & \vec{x} &\in \Gamma_f \end{aligned} \quad (4.11)$$

If the initial state is an unloaded state, where the material is in contact with a filter ( $\mu_{\text{in}}^{\text{f}} = \mu_{\text{ex}}^{\text{f}}$ ), the next holds

$$\boldsymbol{\sigma}_e(\boldsymbol{\epsilon}_i) - \Delta\pi(\boldsymbol{\epsilon}_i)\mathbf{I} = \mathbf{O} \quad (4.12)$$

provided that the medium is homogeneous. Then the initial strain is given by

$$\begin{aligned} \epsilon_i &= \epsilon_i \mathbf{I}, \\ \epsilon_i &= \frac{\Delta\pi_i}{2\mu+2\lambda}, \quad \Delta\pi_i = RT \sqrt{(c_i^{\text{fc}})^2 + 4(c_i^{\text{ex}})^2} - 2RTc_i^{\text{ex}} \end{aligned} \quad (4.13)$$

In the case that the swelling in one direction is obstructed, for instance by adjacent vertebrae, the initial strain is not isotropic.

## 4.2.2 Discontinuous kinematics

A set basis or shape functions  $\{N\}_{i=1}^n$ , with  $n$  the number of integration points, form a partition of unity since  $\sum_{i=1}^n N_i = 1$ . A field  $v$  is interpolated as (4.14)

$$v(\vec{x}, t) = \sum_{i=1}^n N_i(\vec{x})(a_i(t) + \sum_{k=1}^m \psi_k(\vec{x})b_{ik}(t)) \quad (4.14)$$

with  $a_i$  the regular degrees of freedom (DOFs),  $\{\psi\}_{k=1}^m$  additional basis functions and  $b_{ik}$  additional degrees of freedom [9]. These additional basis functions may not originate from the span of the original set of basis functions.

Using these extra basis functions, the displacement field and the chemical potential distribution are separated into two different scales: the bulk behavior (standard field) and crack behavior (enhanced field). The opening or sliding of a crack can be incorporated as a jump in the displacement. A jump in displacement is mathematically represented by a function operating on a smooth continuous function: the Heaviside function. We assume that the strain field is defined everywhere even at the surface across which the jump occurs. Then the displacement field  $\vec{u}$  of the body can be additively decomposed into the continuous part  $\hat{\vec{u}}$  and the enhanced part  $\tilde{\vec{u}}$  [80].

$$\vec{u}(\vec{x}) = \hat{\vec{u}}(\vec{x}, t) + \mathcal{H}_{\Gamma_d}(\vec{x})\tilde{\vec{u}}(\vec{x}, t) \quad (4.15)$$

The Heaviside function  $\mathcal{H}_{\Gamma_d}$  is defined by (4.16) with the jump at the discontinuity.

$$\mathcal{H}_{\Gamma_d} = \begin{cases} -h/2 & \vec{x} \in \Omega^+ \\ +h/2 & \vec{x} \in \Omega^- \end{cases} \quad (4.16)$$

The Heaviside function is acting on the smooth function  $\tilde{\vec{u}}(\vec{x}, t)$  keeping the crack surface continuous. The jump at the discontinuity  $\Gamma_d$  is given by  $[\vec{u}]$  and represents the opening of the crack.

$$[\vec{u}(\vec{x}, t)] = h\tilde{\vec{u}}(\vec{x}, t), \quad \vec{x} \in \Gamma_d. \quad (4.17)$$

This is represented in 1D by Fig. 4.2. The strain becomes Eq. (4.18).

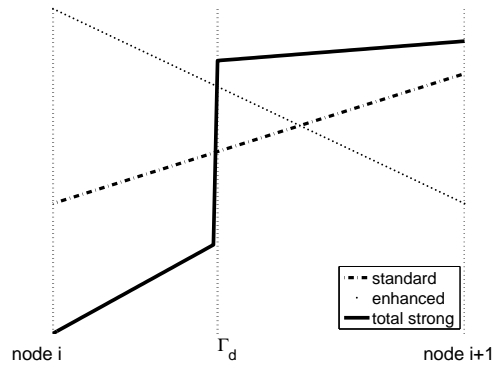


**Figure 4.2:** A 1-D representation of the effect of the Heaviside function. The total field built from the standard field and the enhanced field around the crack  $\Gamma_d$ .

$$\epsilon = \vec{\nabla}^s \vec{u} = \vec{\nabla}^s \hat{u} + \mathcal{H}_{\Gamma_d} \vec{\nabla}^s \tilde{u} + \delta_{\Gamma_d} (\tilde{u} \vec{n}^+)^s \tag{4.18}$$

with  $\vec{n}^+$  the normal at the crack surface directed inwards. The last term only has a contribution in the variational description at the discontinuity.

Figure 4.3 shows in two steps what happens at the crack. On initial growth a small opening arises, i.e. small displacement jump, and a steep gradient in the chemical potential occurs over a small transition zone (case A). While the opening grows, the gradient in the chemical potential decreases in magnitude and spreads over a wider transition zone. High gradients as result of shear loading are approximated by a jump  $\tilde{\mu}^f(\vec{x}, t)$  over the

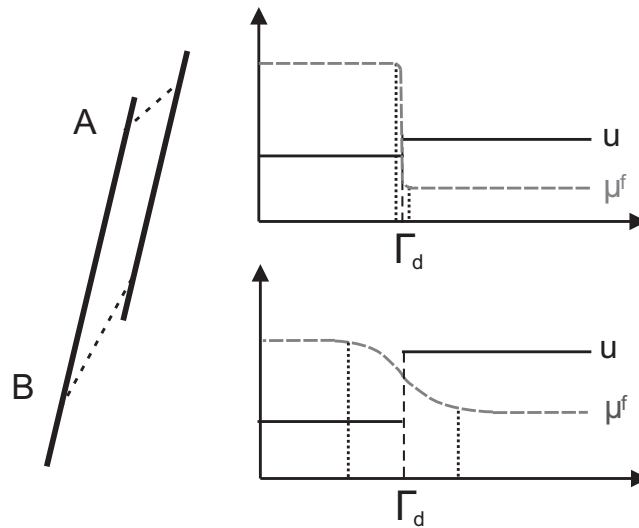


**Figure 4.3:** When the crack grows, the displacement jump becomes nonzero and a large gradient in chemical potential arises with a small transition zone (A). With time, the displacement jump grows, the gradient in chemical potential decreases and the transition zone decreases.

crack surfaces, Fig. 4.4.

In this case the decomposition becomes

$$\mu^f(\vec{x}) = \hat{\mu}^f(\vec{x}, t) + \mathcal{H}_{\Gamma_d}(\vec{x}) \tilde{\mu}^f(\vec{x}, t) \quad (4.19)$$

and the difference in chemical potential at the discontinuity is given by  $[\mu^f]$ :

$$[\mu^f(\vec{x}, t)] = h \tilde{\mu}^f(\vec{x}, t), \quad \vec{x} \in \Gamma_d. \quad (4.20)$$

The gradient in the chemical potential becomes

$$\vec{\nabla}^s \mu^f = \vec{\nabla}^s \hat{\mu}^f + \mathcal{H}_{\Gamma_d} \vec{\nabla}^s \tilde{\mu}^f + h \delta_{\Gamma_d} (\tilde{\mu}^f \vec{n}^+) \quad (4.21)$$

### 4.2.3 Local behavior

The governing equations for the bulk material and discontinuity kinematics are related by constitutive modeling at the discontinuity in the shape of boundary conditions. A local coordinate system  $(n, s)$  is introduced where  $n$  is in the direction of the normal vector to  $\Omega^+$  and  $s$  is orthogonal in the direction of propagation. This means a displacement jump is decoupled into

$$[\vec{u}] = [\vec{u}]_n \vec{n}^+ + [\vec{u}]_s \vec{t}^+ \quad (4.22)$$

with  $\vec{n}^+ = -\vec{n}^-$  directed into the body and  $\vec{t}^+$  is directed along the crack surface in direction of propagation. We define crack surfaces  $\Gamma_d^+ = \partial\Omega^+ \cap \Gamma_d$  and  $\Gamma_d^- = \partial\Omega^- \cap \Gamma_d$ .

#### Local mass balance

Deformation at the discontinuity induces fluid flow. The contribution of flow along the discontinuity is negligible in case of shear failure. The fluid flow across the crack surfaces is not. Figure 4.4 shows a schematic overview of the local mass balance. The flow across each of the crack surfaces ( $f_{\Gamma}^{\pm}$ ) are equal and depend on the local pressure gradient and material properties.

Because of the coarseness of the mesh, the local pressure gradient is unresolved and the pressure gradient is modeled as a jump:

$$\vec{q} \cdot \vec{n}^+ = f_{\Gamma}^+(\vec{x}, t) = -f_{\Gamma}^-(\vec{x}, t) = -K \frac{\mu^{f+} - \mu^{f-}}{2\Delta x} \quad (4.23)$$

where  $\Delta x$  is the distance the fluid flow has overcome and depends on the time  $\Delta t$  since discontinuity developed at that place, the bulk permeability  $K$  and aggregate modulus of the material ( $c = 2\mu + \lambda - \frac{\delta\pi}{\delta tr(\epsilon)}$ ), namely  $2\Delta x^2 \approx \Delta t K c$ . Then

$$f_{\Gamma}^+ = -k_d (\mu^{f+} - \mu^{f-}) = -k_d [\mu^f] = -h k_d \tilde{\mu}^f \quad (4.24)$$

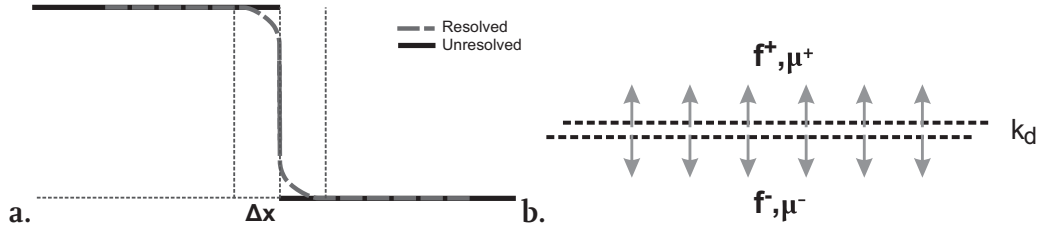


**Figure 4.4:** a. Representation of the gradient in the chemical potential near a discontinuity approximated by a jump. b. Schematic representation of the fluid flow at the crack surface.

Equation (4.24) is Darcy's equation on the unresolved scale and should correspond to the same equation on the resolved scale Eq. (4.23). This is true if - unlike the paper [82] where a diaphragm in the crack is assumed - we choose the unresolved hydraulic permeability.

$$k_d = \sqrt{\frac{K}{c\Delta t}}. \quad (4.25)$$

The unresolved hydraulic permeability is therefore derived from intrinsic material properties.

### Local momentum balance

A discrete crack is preceded by local damage. This micro-damage is lumped into one constitutive relation (cohesive zone) and projected on the crack [80], Fig. 1.7. The model relates the decohesion, i.e. softening of the traction forces, as result of opening of the crack. For the traction forces at each surface holds  $\sigma \cdot \vec{n}^+ = \vec{t}_\Gamma^+ = -\vec{t}_\Gamma^- = -\sigma \cdot \vec{n}^-$ .

$$(\sigma_e - (\mu^f + \Delta\pi)\mathbf{I})^\pm \cdot \vec{n}^\pm = \vec{t}_\Gamma^\pm(\vec{x}, t), \quad \vec{x} \in \Gamma^\pm \quad (4.26)$$

The cohesive law holds locally and is described in local coordinate system of the discontinuity. The cohesive zone model is usually nonlinear and acts on the effective stress. The system is linearized in order to use the Newton-Rhapson procedure. Locally holds for the change in traction forces w.r.t. previous step ( $\Delta\vec{t}_d$ ) the following equation

$$\Delta\vec{t}_d = (\vec{n}^+ \vec{t}^+) \underline{t}_d, \quad \Delta\underline{t}_d = h\underline{T}_d \underline{u}_d \quad (4.27)$$

with  $\underline{t}_d$  column vector of the traction forces and  $\underline{u}_d$  column vector of displacement in local coordinates. Matrix  $\underline{T}_d$  is the tangent stiffness of the cohesive zone model. A transition of local to global coordinates is made to express the traction forces in terms of nodal displacements. The change in traction forces  $\Delta\vec{t}_\Gamma^\pm$  in global coordinates is given by

$$\Delta\vec{t}_d^\pm = (\vec{e}_1 \vec{e}_2) \Delta\underline{t}_d^\pm. \quad (4.28)$$

Then the transition from local coordinates to global coordinates occurs through a mapping  $\underline{Q}$

$$(\vec{e}_1 \vec{e}_2) = (\vec{n}^+ \vec{t}^+) \underline{Q}^T. \quad (4.29)$$

The change in traction forces  $\Delta \vec{t}_\Gamma^+$  in local coordinates is expressed in terms of enhanced nodal displacements.

$$\Delta \vec{t}_\Gamma^+ = \underline{Q} \vec{t}_d^+ - (\mu^f + \Delta\pi)^+ \vec{n}^+ = \underline{Q} \underline{T}_{e,d} \underline{Q}^T \vec{u} - (\mu^f + \Delta\pi)^+ \vec{n}^+ \quad (4.30)$$

Then the tangent stiffness in element coordinates is given by  $\underline{T}_e = \underline{Q} \underline{T}_{e,d} \underline{Q}^T$ . Furthermore for the osmotic forces at the crack surfaces holds

$$\pi^+ = 2RTc^{\text{ex}}, \Delta\pi^+ = 0, \quad (4.31)$$

as the ionic concentration in the crack is the same as in the external reservoir.

### Yield criterion

Crack growth is determined by damage in the solid matrix. Therefore the yield criterion, next to the cohesive zone, is related to the effective stress. The effective stress at the crack-tip varies locally, therefore the critical effective stress state is calculated nonlocally using Gaussian functions following Wells et al. [107], Fig. B.5.

$$\begin{aligned} \sigma_{tip} &= \sum_{i=1}^{n_{tot}} \frac{w_i}{w_{tot}} \sigma_i \\ w_{tot} &= \sum_{j=1}^{n_{tot}} w_j \\ w_i &= \frac{(2\pi)^{2/3}}{l_a^3} e^{-\frac{r_i^2}{2l_a^2}}. \end{aligned} \quad (4.32)$$

with  $r_i$  the distance between integration point  $i$  and the crack-tip and  $l_a$  is a length scale parameter which determines the influence of a sample point.

Crack propagation is initiated when maximum shear stress ( $\tau_{max}$ ) is larger than the critical value  $\tau_{ult}$  (Tresca criterion). The maximum shear stress and associated angle  $\alpha_t$  is calculated from the stress state according to

$$\begin{aligned} \tau_{max} &= -\frac{\sigma_{xx} - \sigma_{yy}}{2\sigma_{xy}} \\ \alpha_t &= \frac{1}{2} \text{atan}(\tau_{max}) \end{aligned} \quad (4.33)$$

This orientates the interface in direction of maximum shear stress.

## 4.3 Numerical description

The weak form for the Finite Element Method is derived by standard Galerkin approach. Then the weak equations are discretized leading to a time-dependent, non-linear system. This is solved using a Crank-Nicholson scheme for time-integration and Newton-Rhapson iteration within each time increment.

### 4.3.1 Weak form

The momentum balance and mass balance are multiplied by test functions and subsequently integrated over the domain  $\Omega$ . These test functions are taken of the same form as the shape functions for the independent variables and therefore consisting for a standard and enhanced field.

$$\vec{\eta} = \hat{\eta} + \mathcal{H}_{\Gamma_d} \tilde{\eta}, \quad \varphi = \hat{\varphi} + \mathcal{H}_{\Gamma_d} \tilde{\varphi}. \quad (4.34)$$

Using integration by parts the discontinuity is introduced as a boundary integral. This means that Dirac-terms in strain (4.18) has no contribution anymore in the integration over the body.

#### Momentum balance

The momentum equation becomes

$$\int_{\Omega^+ \cup \Omega^-} \vec{\nabla}^s (\hat{\eta} + \mathcal{H}_{\Gamma_d} \tilde{\eta}) : \sigma d\Omega = \int_{\Gamma_t} (\hat{\eta} + \mathcal{H}_{\Gamma_d} \tilde{\eta}) \cdot \vec{t}_t d\Gamma - \int_{\Gamma_d} \tilde{\eta} \cdot h(\vec{t}_\Gamma^+ + \vec{t}_\Gamma^-) / 2 d\Gamma \quad (4.35)$$

This equation must hold for all variations of test functions, therefore it hold also if  $\hat{\eta} = \vec{0}$  or if  $\tilde{\eta} = \vec{0}$ . Both options are separately applied. This results in two equations. The first equation denotes the bulk behavior.

$$\int_{\Omega^+ \cup \Omega^-} \vec{\nabla}^s \hat{\eta} : \sigma d\Omega = \int_{\Gamma_t} \hat{\eta} \cdot \vec{t}_t d\Gamma \quad (4.36)$$

Filling in the traction forces leads to Eq. (4.37).

$$\begin{aligned} & \int_{\Omega^+ \cup \Omega^-} \mathcal{H}_{\Gamma_d} \vec{\nabla}^s \tilde{\eta} : \sigma d\Omega + h \int_{\Gamma_d^+} \tilde{\eta} \cdot (\vec{t}_d^+ - \mu^{f+} \vec{n}^+) d\Gamma \\ & = \int_{\Gamma_t} \mathcal{H}_{\Gamma_d} \tilde{\eta} \cdot \vec{t}_t d\Gamma \end{aligned} \quad (4.37)$$



### Mass balance

Similarly, the variational equations for mass balance are derived. Note that  $\vec{\nabla} \cdot \vec{u} = tr(\epsilon)$ . Then mass balance for bulk behavior becomes

$$\int_{\Omega^+ \cup \Omega^-} \vec{\nabla} \varphi \cdot \vec{q} d\Omega - \int_{\Omega^+ \cup \Omega^-} \varphi (tr(\dot{\epsilon}) + \mathcal{H}_{\Gamma_d} tr(\dot{\epsilon})) d\Omega = \int_{\Gamma_f} \varphi f_f d\Gamma \quad (4.38)$$

The variational equation for mass balance at the discontinuity becomes

$$\begin{aligned} & \int_{\Omega^+ \cup \Omega^-} \mathcal{H}_{\Gamma_d} \vec{\nabla} \varphi \cdot \vec{q} d\Omega - \int_{\Omega^+ \cup \Omega^-} \varphi (tr(\dot{\epsilon}) + \mathcal{H}_{\Gamma_d} tr(\dot{\epsilon})) d\Omega \\ &= \int_{\Gamma_f} \mathcal{H}_{\Gamma_d} \varphi f_f d\Gamma - h \int_{\Gamma_d} \varphi \vec{q} \cdot \vec{n}^+ d\Gamma \end{aligned} \quad (4.39)$$

with

$$\int_{\Gamma_d} \varphi \vec{q} \cdot \vec{n}^+ d\Gamma = -h \int_{S_d} \varphi k_d \hat{\mu}^f d\Gamma \quad (4.40)$$

In equation (4.39) the seepage flux at the discontinuity is related to deformation of the discontinuity. This combination forms the mass balance at the discontinuity and results into a symmetry with the traction forces in the stiffness matrix for the numerical simulations. The weak form is provided by equations (4.36), (4.37), (4.38) and (4.39). Constitutive behavior at the crack are introduced as a boundary condition.

## 4.3.2 Discretization

### Spatial discretization

A discretized form is derived by dividing body  $\Omega$  into elements  $\Omega_e, e = 1..n_e$  ( $\Omega = \bigcup_1^{n_e} \Omega_e$ ). The result is that also the discontinuity is discretized in elements  $S_d$  and the boundary in elements  $S_e$ . A transition from tensor to matrix notation is made introducing columns. The displacements, the chemical potential and their variations are discretized similarly (Bubnov-Galerkin approach) by

$$\begin{aligned} \hat{u} &= \vec{N}^T \underline{a}_u, & \tilde{u} &= \vec{N}^T \underline{b}_u \\ \hat{\mu}^f &= \underline{m}^T \underline{a}_\mu, & \tilde{\mu}^f &= \underline{m}^T \underline{b}_\mu \end{aligned} \quad (4.41)$$

where  $\vec{N} = [N_x \ N_y]$  contains the shape functions, which are the same in  $x$ - and  $y$ -direction. The columns  $\underline{a}_u$  and  $\underline{b}_u$  contain the nodal values for bulk part and enhanced part, resp.. Similar are  $\underline{m}$ ,  $\underline{a}_\mu$  and  $\underline{b}_\mu$  columns of shape functions and nodal values. Then strain is discretized by

$$\vec{\nabla}^s \epsilon = \underline{B} \underline{a}_u + \mathcal{H}_{\Gamma_d} \underline{B} \underline{b}_u \quad (4.42)$$

The first order differential operator on the displacement shape functions is denoted by  $\underline{B} = [\underline{L}N_x \ \underline{L}N_y]$  The matrix  $\underline{L}$  contains the differential operators:

$$\underline{L} = \begin{pmatrix} \frac{\partial}{\partial x} & 0 \\ 0 & \frac{\partial}{\partial y} \\ \frac{\partial}{\partial y} & \frac{\partial}{\partial x} \end{pmatrix} \quad (4.43)$$

Furthermore  $\underline{C} = \underline{L}^T(\vec{l}m^T)$  a  $2 \times m$  matrix is defined with  $\vec{l} = (1 \ 1 \ 0)^T$ . Then  $\underline{B}^T \cdot (\vec{l}m^T) = \vec{N}\underline{C}$  holds and  $\vec{\nabla}\mu^f = \underline{C}a_\mu + \mathcal{H}_{\Gamma_d}Cb_\mu$ .

Finally the stress and flux are defined. The stress consists of the effective stress and the chemical potential. The effective stress in vector notation is given by  $\underline{\sigma}_e = (\sigma_{e,xx}, \sigma_{e,yy}, \sigma_{e,xy})^T$ . The stress is linearized to the vector of nodal values such that a Newton-Rhapson scheme can be used.

$$\begin{aligned} \underline{\sigma} &= \frac{\partial \sigma}{\partial \underline{\epsilon}} \frac{\partial \underline{\epsilon}}{\partial \underline{a}_u} \underline{a}_u + \frac{\partial \sigma}{\partial \underline{\epsilon}} \frac{\partial \underline{\epsilon}}{\partial \underline{b}_u} \underline{b}_u + \frac{\partial \sigma}{\partial \underline{a}_\mu} a_\mu + \frac{\partial \sigma}{\partial \underline{b}_\mu} b_\mu \\ &= \underline{DB}\underline{a}_u + \mathcal{H}_{\Gamma_d}\underline{DB}\underline{b}_u - (\vec{l}m^T)a_\mu - \mathcal{H}_{\Gamma_d}(\vec{l}m^T)b_\mu \end{aligned} \quad (4.44)$$

Here  $\underline{D}$  is a  $(3 \times 3)$  matrix for 2-D. The matrix  $\underline{D}$  is defined as follows ( $c = 2\mu + \lambda + \frac{\partial \Delta \pi}{\partial \text{tr}(\underline{\epsilon})}$ ).

$$\underline{D} = \begin{pmatrix} c & (c - 2\mu) & 0 \\ (c - 2\mu) & c & 0 \\ 0 & 0 & 2\mu \end{pmatrix} \quad (4.45)$$

Furthermore the total traction forces at the discontinuity  $S_d$  are defined as

$$(\underline{\sigma}_e - (\mu^f + \Delta \pi)\underline{I}) \cdot \vec{n}^+ = \vec{t}_\Gamma^+ = h\underline{T}\vec{N}^T \underline{b}_u - \vec{n}^+ (m^T a_\mu + \frac{h}{2} m^T b_\mu) \quad (4.46)$$

with  $\underline{T} = \underline{T}_e$  the tangent stiffness including osmotic forces. The seepage flux is linearized by

$$\begin{aligned} \vec{q} &= \frac{\partial \vec{q}}{\partial \underline{a}_u} \underline{a}_u + \frac{\partial \vec{q}}{\partial \underline{b}_u} \underline{b}_u + \frac{\partial \vec{q}}{\partial a_\mu} a_\mu + \frac{\partial \vec{q}}{\partial b_\mu} b_\mu \\ &= -\underline{K}C a_\mu - \mathcal{H}_{\Gamma_d} \underline{K}C b_\mu \end{aligned} \quad (4.47)$$

### Time discretization

The introduction of fluid flow does demands a time stepping algorithm. Time stepping here is therefore driven by diffusion of the fluid and not dissipation of energy [80]. The solution is sensitive to the magnitude of the time increment (time step). A large time step leads to underestimation of fluid pressure in confined compression. Taking too

small steps leads to initial oscillation. For stable time integration the next law has to be satisfied [103]:

$$\Delta t > \frac{\Delta x^2}{cK} \quad (4.48)$$

A Cranck-Nicholson scheme is used. This means that differential terms are approximated linearly by looking at the difference between the new and old step and values of the independent variables are weighted results of the new and old time step. Define  $\vec{c}_u = (\vec{a}_u^T \vec{b}_u^T)^T$  and  $\vec{c}_\mu = (\vec{a}_\mu^T \vec{b}_\mu^T)^T$  and  $\vec{c} = (\vec{c}_u^T \vec{c}_\mu^T)^T$ . The next holds

$$\begin{aligned} \frac{\partial \vec{c}}{\partial t} &= \frac{\vec{c}^{n+1} - \vec{c}^n}{\Delta t} \\ \vec{c} &= \theta \vec{c}^{n+1} + (1 - \theta) \vec{c}^n \end{aligned} \quad (4.49)$$

Stabilization is reached if implicit time stepping is used, i.e.  $\theta \geq 0.5$ . Taking  $\theta = 1$  reduces the method to Euler implicit.

### 4.3.3 Total system

Although the bulk material is assumed linear elastic, the presence of damage introduces nonlinearity. The system is therefore solved iteratively at each time step. Define  $\vec{c}_u = (\vec{a}_u^T \vec{b}_u^T)^T$  a  $4n \times 1$  vector and  $\vec{c}_\mu = (\vec{a}_\mu^T \vec{b}_\mu^T)^T$  a  $2m \times 1$  vector.

In the equations subscript  $i$  denotes the temporary solution  $\vec{c}_i$  in iteration step  $i$  and superscript  $n$  denotes the solution  $\vec{c}^n$  of previous time step  $n$ .

---

#### Newton-Rhapson solution procedure with Cranck-Nicholson

- **Step 0:**  $\vec{c}_0 = \vec{c}^n$
- **Step i+1:**
  - If no convergence solve
 
$$\begin{pmatrix} \underline{K}_{uu,i} & -\underline{K}_{u\mu} \\ -\underline{K}_{\mu u} & -\Delta t \theta \underline{K}_{\mu\mu} \end{pmatrix} \delta \vec{c}_i = \begin{pmatrix} f_{\text{ext},u} - f_{\text{int},u} \\ \Delta t f_{\text{ext},-}^\theta - \Delta t f_{\text{int},-}^\theta \end{pmatrix} \quad (4.50)$$
  - $\vec{c}_{i+1} = \vec{c}_i + \delta \vec{c}_i, i = i + 1$
- **Final iteration step:**  $\vec{c}^{n+1} = \vec{c}^n + \sum_i \delta \vec{c}_i$

The matrices involved are given below.

$$\begin{aligned}
\underline{K}_{uu,i} &= \begin{pmatrix} \int_{\Omega_e} \underline{B}^T \underline{D}_i \underline{B} d\Omega & \int_{\Omega_e} \mathcal{H}_{\Gamma_d} \underline{B}^T \underline{D}_i \underline{B} d\Omega \\ \int_{\Omega_e} \mathcal{H}_{\Gamma_d} \underline{B}^T \underline{D}_i \underline{B} d\Omega & \int_{\Omega_e} \mathcal{H}_{\Gamma_d}^2 \underline{B}^T \underline{D}_i \underline{B} d\Omega + \underline{M}_{uu,i} \end{pmatrix} \\
\underline{K}_{\mu\mu,i} &= \begin{pmatrix} \int_{\Omega_e} \underline{C}^T \underline{K}_i \underline{C} d\Omega & \int_{\Omega_e} \mathcal{H}_{\Gamma_d} \underline{C}^T \underline{K}_i \underline{C} d\Omega \\ \int_{\Omega_e} \mathcal{H}_{\Gamma_d} \underline{C}^T \underline{K}_i \underline{C} d\Omega & \int_{\Omega_e} \mathcal{H}_{\Gamma_d}^2 \underline{C}^T \underline{K}_i \underline{C} d\Omega + \underline{M}_{\mu\mu,i} \end{pmatrix} \\
\underline{K}_{u\mu} &= \begin{pmatrix} \int_{\Omega_e} \underline{N} \underline{C} d\Omega & \int_{\Omega_e} \mathcal{H}_{\Gamma_d} \underline{N} \underline{C} d\Omega \\ \int_{\Omega_e} \mathcal{H}_{\Gamma_d} \underline{N} \underline{C} d\Omega + \underline{M}_{u\mu,i} & \int_{\Omega_e} \mathcal{H}_{\Gamma_d}^2 \underline{N} \underline{C} d\Omega + h \underline{M}_{u^-,i} / 2 \end{pmatrix} \\
\underline{K}_{\mu u}^T &= \begin{pmatrix} \int_{\Omega_e} \underline{N} \underline{C} d\Omega & \int_{\Omega_e} \mathcal{H}_{\Gamma_d} \underline{N} \underline{C} d\Omega \\ \int_{\Omega_e} \mathcal{H}_{\Gamma_d} \underline{N} \underline{C} d\Omega & \int_{\Omega_e} \mathcal{H}_{\Gamma_d}^2 \underline{N} \underline{C} d\Omega \end{pmatrix},
\end{aligned} \tag{4.51}$$

$$\begin{aligned}
\underline{M}_{uu,i} &= h^2 \int_{S_d} \underline{\tilde{N}} \underline{T}_i \underline{\tilde{N}}^T d\Gamma = h^2 \int_{S_d} \underline{\tilde{N}} \underline{T}_{e,i} \underline{\tilde{N}}^T d\Gamma \\
\underline{M}_{\mu\mu,i} &= h^2 \int_{S_d} k_{d,i} \underline{m} \underline{m}^T d\Gamma \\
\underline{M}_{u^-} &= h \int_{S_d} \underline{\tilde{N}} \underline{\tilde{n}}^+ \underline{m}^T d\Gamma
\end{aligned} \tag{4.52}$$

and

$$\begin{aligned}
\underline{f}_{\text{int},u} &= \begin{pmatrix} \int_{\Omega_e} \underline{B}^T \underline{\sigma}_i d\Omega \\ \int_{\Omega_e} \mathcal{H}_{\Gamma_d} \underline{B}^T \underline{\sigma}_i d\Omega + \int_{\Gamma_d} \underline{\tilde{N}} \underline{\tilde{t}}_{\Gamma,i}^+ d\Gamma \end{pmatrix} \\
\underline{f}_{\text{int},^-}^\theta &= \begin{pmatrix} \int_{\Omega_e} \underline{C}^T (\theta \underline{\tilde{q}}_i + (1-\theta) \underline{\tilde{q}}^n) d\Omega - \int_{\Omega_e} \underline{C}^T \underline{\tilde{N}}^T \frac{\underline{\tilde{u}}_i - \underline{\tilde{u}}^n}{\Delta t} d\Omega \\ \int_{\Omega_e} \mathcal{H}_{\Gamma_d} \underline{C}^T (\theta \underline{\tilde{q}}_i + (1-\theta) \underline{\tilde{q}}^n) - \frac{\underline{\tilde{u}}_i - \underline{\tilde{u}}^n}{\Delta t} d\Omega + \int_{\Gamma_d} \underline{m} (\theta f_{\Gamma,i}^+ + (1-\theta) f_{\Gamma}^{+,n}) d\Gamma \end{pmatrix} \\
\underline{f}_{\text{ext},u} &= \begin{pmatrix} \int_{\Gamma_t} \underline{\tilde{N}} \underline{\tilde{t}}_t^{n+1} d\Gamma \\ \int_{\Gamma_t} \mathcal{H}_{\Gamma_d} \underline{\tilde{N}} \underline{\tilde{t}}_t^{n+1} d\Gamma \end{pmatrix} \\
\underline{f}_{\text{ext},^-}^\theta &= \begin{pmatrix} \int_{\Gamma_f} \underline{m} (\theta f_f^{n+1} - (1-\theta) f_f^n) d\Gamma \\ \int_{\Gamma_f} \mathcal{H}_{\Gamma_d} \underline{m} (\theta f_f^{n+1} - (1-\theta) f_f^n) d\Gamma \end{pmatrix}
\end{aligned} \tag{4.53}$$

The same matrix relations hold for bulk behavior, discontinuity behavior and their connections plus some additive linking.

Babuska-Brezzi stability criterion is met if displacement is linearly interpolated and the chemical potential is defined in the middle of the element. This is not possible since the crack will get too close to the node and robustness is lost. Another possibility is to interpolate displacements quadratically and the chemical potential linearly. As result, element integration is more difficult. Since Réthoré et al. [82] do not suffer from these issues while violating the Babuska-Brezzi criterion, here also bilinear basis functions are used. The model has been programmed using the Jem/Jive finite element toolkit which has been developed by Habanera. For implementation aspects like the tracking of the crack-tip, increasing the degrees of freedom or other propagation issues we refer to Remmers et al. [78,80,81] and appendix B.

## 4.4 Numerical examples

Two examples are considered. Firstly, a static crack under shear loading is studied for verification. Secondly, quasi-static crack growth due to confined compression is viewed.

### 4.4.1 Verification

A sample of size 8 mm  $\times$  6 mm is considered with in the middle a crack of length  $2L = 2$  mm. The crack is impulsively loaded by a two-edge dislocation [51]. The crack surfaces are assumed friction free. This loading leads to a high shear stress at the crack-tips, which relaxes due to redistribution of the fluid. Figure 3.1 shows the loading. The analytical solution for shear stress distribution in plane of the crack is given by Eq. (3.25) and for flow by Eq. (3.30). The distribution for the chemical potential over the complete material is given by Eq. (3.29).

In contradiction to chapter 3, there are no element edges in plane of the crack. This results in a slightly different mesh than in Fig. 3.2. For the numerical simulations three meshes are considered: 112 elements (denoted by  $N = 1$ ), 510 elements (denoted by  $N = 2$ ) and 2170 (denoted by  $N = 4$ ). Each mesh is a refinement of the previous. All sides are restricted in movement: upper and lower sides in  $y$ -direction and left and right sides in  $x$ -direction. Furthermore at all sides fluid flow is free and therefore  $d\mu^f = 0$ . The material properties are given in Tab. 4.1.

Table 4.1: Material properties for verification.

$R$	$= 8.3145$	[N mm/mmol K]	$T$	$= 298$	[K]
$E$	$= 0.9$	[MPa]	$\nu$	$= 0.20$	[-]
$\varphi_i^f$	$= 0.80$	[-]	$K$	$= 0.24e-3$	[mm <sup>4</sup> /Ns]
$c^{ex}$	$= 0.15e-3$	[mmol/mm <sup>3</sup> ]	$c_1^{fc}$	$= -0.2e-3$	[mmoleq/mm <sup>3</sup> ]
$d$	$= 0.0040$	[mm]	$L$	$= 1.0$	[mm]

### 4.4.2 Compression test

Until now a static crack is considered. As far as we know, there seems to be no benchmark for discrete shear failure in porous media, let alone for ionized porous media. To show that in shearing the osmotic prestress plays an important role a compression test is considered. For the compression test the sample is boxed except for the contact area with the piston. On the right the sample is in contact with a filter, which causes an equilibrium with an external salt solution ( $\mu_{in}^f = \mu_{ex}^f$ ). An initial crack is imposed away from element interfaces (Fig. 4.6).

For the cohesive damage model an exponential law similar to Xu and Needleman [112] is used, Fig 4.5. This law denotes the softening behavior after reaching the critical stress

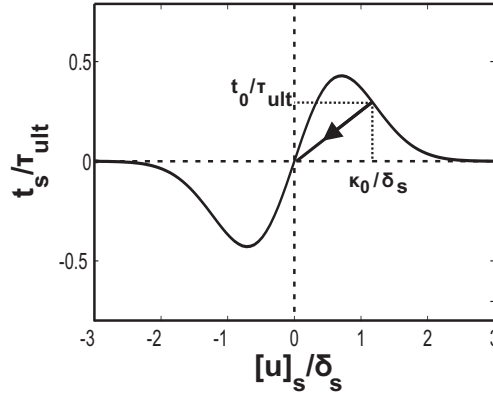


**Figure 4.5:** Normalized distribution of the exponential cohesive law for shearing related traction forces and displacement.

state. Defined is critical length  $\delta_s = \mathcal{G}_c / \tau_{ult}$ , with  $\tau_{ult}$  the ultimate traction forces and  $\mathcal{G}_c$  fracture toughness. The cohesive law is then

$$t_s = \tau_{ult} \frac{[u]_s}{\delta_s} e^{-\left(\frac{[u]_s}{\delta_s}\right)^2} \quad (4.54)$$

Note that the surface underneath the curve is the fracture toughness  $\mathcal{G}_c$ :

$$\begin{aligned} \int_{-\infty}^{\infty} t_s d[u]_s &= \int_{-\infty}^{\infty} t_s d[u]_s \\ &= \tau_{ult} \delta_s 2 \int_0^{\infty} \frac{r}{2} e^{-r^2} dr = \tau_{ult} \delta_s = \mathcal{G}_c. \end{aligned} \quad (4.55)$$

A history parameter  $\kappa$  is introduced in case of unloading each time step the current opening  $\kappa_0$  and traction  $\tau_0$  are remembered. When the new opening is smaller than previous, then unloading takes place according to

$$t_s = \frac{\tau_0}{\kappa_0} [u]_s. \quad (4.56)$$

Damage is defined as

$$D = 1 - \frac{|t_s|}{\tau_{ult}} \quad (4.57)$$

Macro crack is developed when the local damage approaches maximum ( $D = 1$ ) and therefore when the exponential approaches zero. When locally the opening decreases compared to previous time step unloading takes place. The cohesive law parameters  $\mathcal{G}_c$  and  $\tau_{ult}$  can be obtained from experimental data. The material properties are given in table 4.2. External load is applied through the piston. The piston is moved with constant speed  $v = 0.15e-3$  mm/s. Three types of prestress are considered (Fig. 4.7).

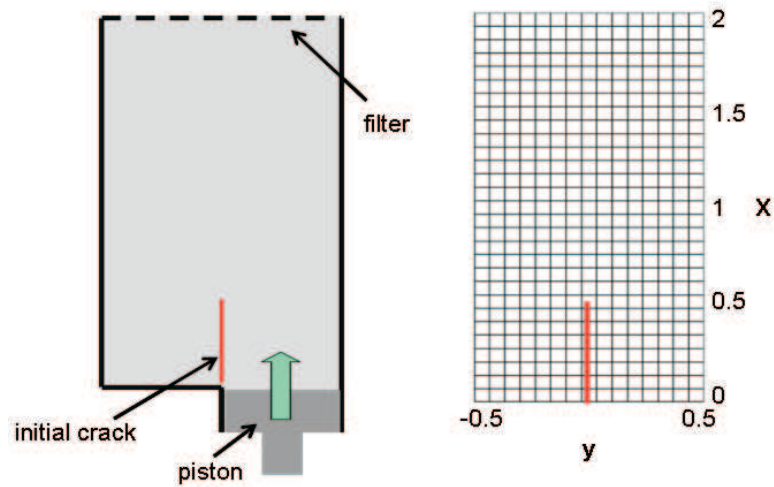


**Figure 4.6:** Left: Schematic representation of the compression test. Right: Representation of the mesh for the compression test.

**Table 4.2:** Material properties for compression test.

$R$	$= 8.3145$	$[\text{N mm}/\text{mmol K}]$	$T$	$= 298$	$[\text{K}]$
$E$	$= 90.0$	$[\text{MPa}]$	$\nu$	$= 0.20$	$[-]$
$\varphi_i^f$	$= 0.80$	$[-]$	$K$	$= 0.28\text{e-}3$	$[\text{mm}^4/\text{Ns}]$
$c^{\text{ex}}$	$= 0.15\text{e-}3$	$[\text{mmol}/\text{mm}^3]$	$c_i^{\text{fc}}$	$= -0.2\text{e-}3$	$[\text{mmoleq}/\text{mm}^3]$
$K_d$	$= 0.28\text{e-}3$	$[\text{mm}^3/\text{Ns}]$			
$\mathcal{G}_c$	$= 2.0$	$[\text{J}/\text{m}^2]$	$\tau_{ult}$	$= 0.4$	$[\text{MPa}]$
$l_a$	$= 0.2$	$[\text{mm}]$	$v$	$= 1.5\text{e-}3$	$\text{mm}/\text{s}$

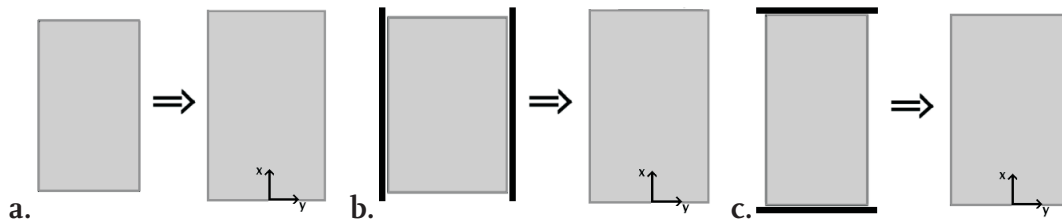


**Figure 4.7:** Representation of the three different types of prestress, namely as result of free swelling a. in both directions, b. in  $x$ -direction and c. in  $y$ -direction.

## 4.5 Results

### 4.5.1 Verification

The dislocation causes a high shear stress just after the crack-tip and a reaction shear stress just before the crack-tip. Furthermore for  $x > 0$  a compressive zone (i.e. positive chemical potential) just above the crack-tip arises and expansion just below the crack. The same behavior is seen at the other crack-tip, but then mirrored.

#### Shear stress distribution

The numerical simulations can be compared to the analytical solution, by averaging the stress over the integration points. Numerically the stress is underestimated at the crack-tips, but this improves upon mesh refinement (Fig. 4.8). Decreasing the space discretization leads to higher underestimation of the stress and larger oscillations.

The impulsive loading of the medium results initially in isochoric deformation and high shear stress. Then the fluid flow redistributes and the shear stress relaxes. Consolidation takes place. This behavior is seen analytically as well as numerically in Fig. 4.9. With refinement, the time dependent behavior of the analytical solution is better approximated. In all numerical calculations oscillations take place. Initially the time discretization deter-

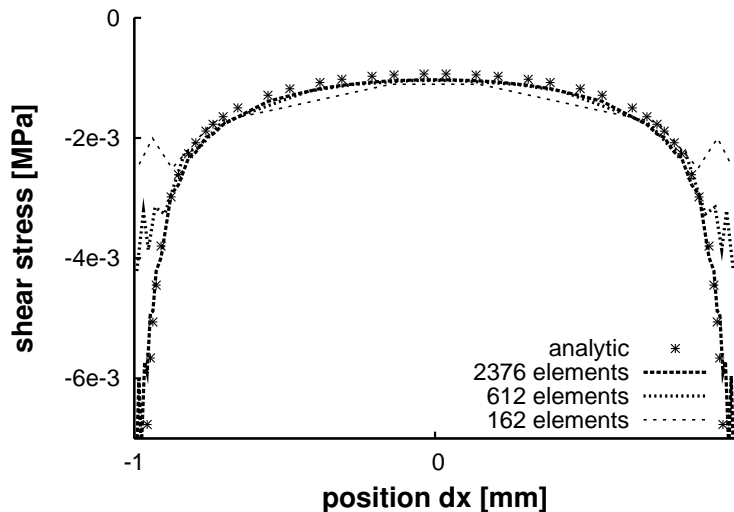


**Figure 4.8:** Numerical shear stress distribution for three different meshes and analytical shear stress distribution at  $y = 0$  for  $t = 32$  s. High singularity at crack-tips  $x \pm 1$  mm is seen.

mines the accuracy of the consolidation behavior. Changing the permeability at the crack has little influence on the solid behavior, Fig. 4.10. The flow across the crack surface shows the influence of the mass balance at the crack.



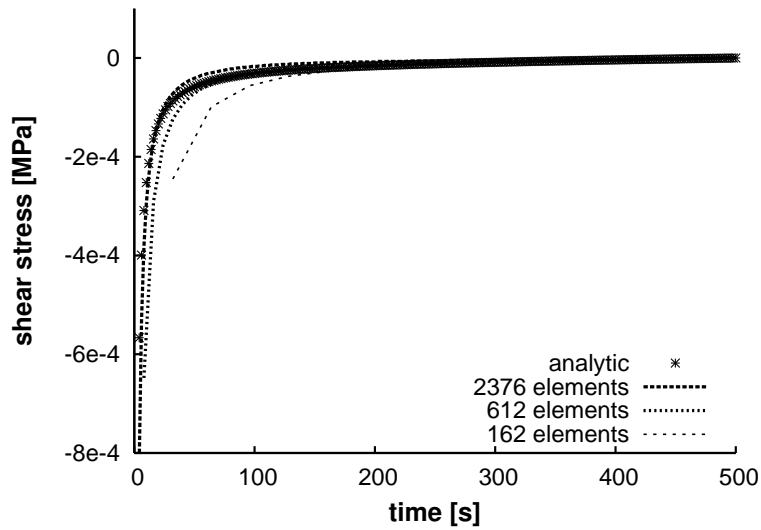


Figure 4.9: Consolidation for different calculations at  $x \approx -0.95$  mm corrected by the equilibrium solution. With refinement, the time dependent behavior of the analytical solution is better approximated.

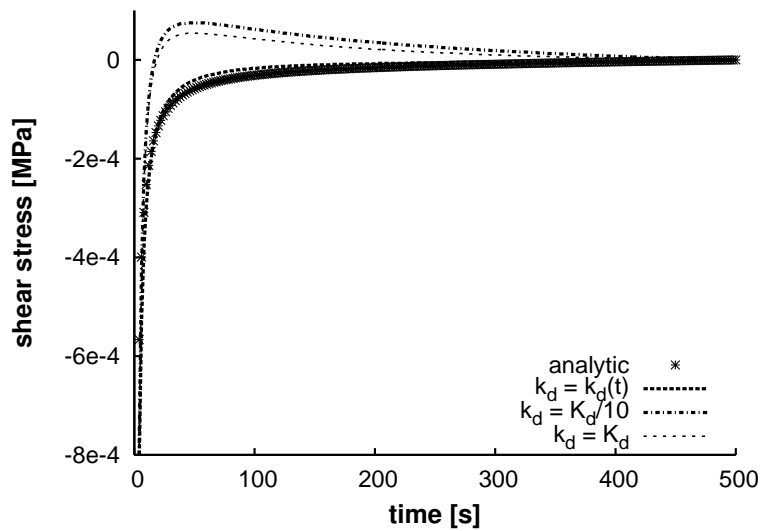
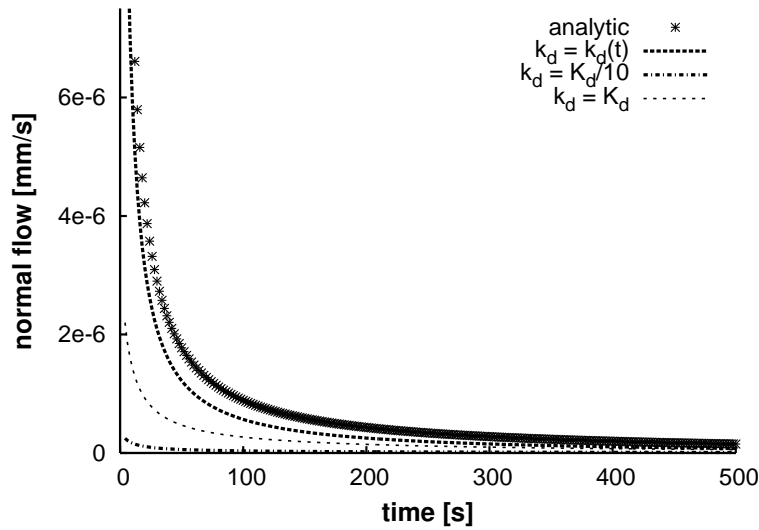


Figure 4.10: Numerically and analytically calculated shear stress at  $x = -0.957$  mm for finest mesh. The influence of  $k_d$  is low, but constant permeability seems to give a little overshoot.

### Flow distribution

Firstly, Fig. 4.11 compares the flow across the crack in time with the analytical solution for three cases: non-constant permeability Eq. (4.25),  $k_d = k_d(t)$ , constant permeability,  $k_d = K_d$ , and a much smaller constant hydraulic permeability,  $k_d = K_d/10$ . The case of a non-constant permeability is closer to the analytical solution because it has a faster flow redistribution than the other cases. In space though, the flow near the crack-tip is



**Figure 4.11:** Numerically and analytically calculated flow ( $\vec{q} \cdot \vec{n}^+$ ) over the crack in time at  $x = -0.923$  mm. The case with crack permeability  $k_d = k_d(t)$  is closest to the analytical solution. A low permeability  $k_d = K_d/10$  prevents flow across the crack surfaces.

underestimated (Fig. 4.12). Comparison of the constitutive discontinuity mass balance, Fig. 4.12a, with the averaged flow at the discontinuity, Fig. 4.12b, shows that the introduced constitutive behavior results in a close match between local constitutive and global constitutive behavior. Comparing partition of unity method (PUM) with other methods

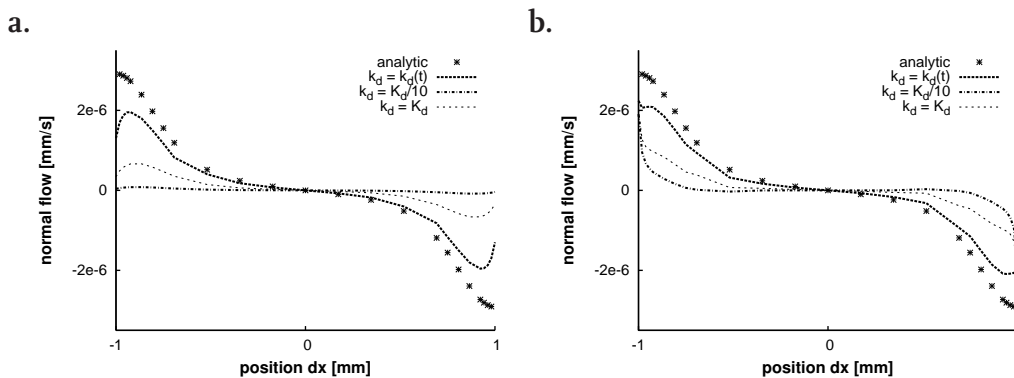


**Figure 4.12:** Numerically and analytically calculated flow over the crack in space for  $t = 32$  s. **a.** Flow as result of local constitutive relation Eq. (4.24) **b.** Averaged flow of global constitutive behavior. The case with unresolved hydraulic permeability  $k_d = k_d(t)$  is closest to the analytical solution. Furthermore, the local flow and averaged flow match well in this case.

shows that PUM captures the shear stress near the crack-tips better than ABAQUS [51], Fig. 4.13a. Taking the pressure field continuous gives poor results with respect to the other methods, Fig. 4.13b.

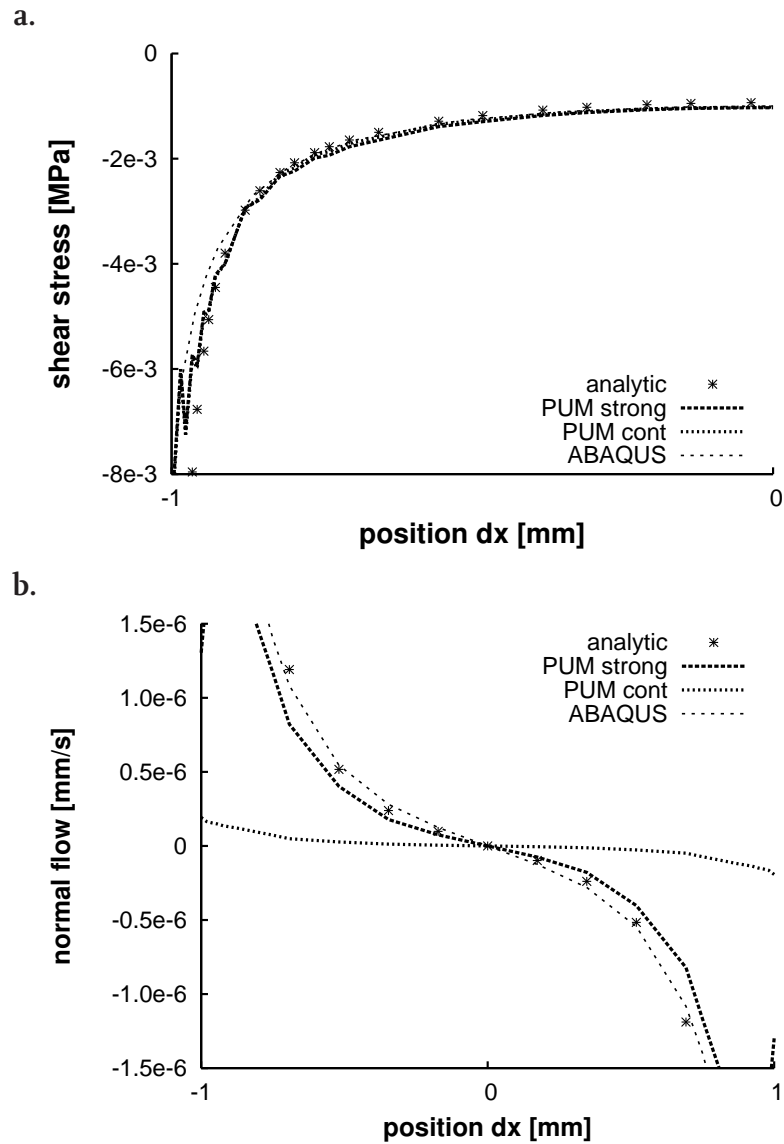


**Figure 4.13:** Resulting numerically and analytically calculated shear stress (a.) and flow (b.) for different methods ( $t = 32$  s). ABAQUS calculations [51] perform less than PUM calculations for stress distributions. Taking the pressure field continuous give the worse results for the fluid flow.

### 4.5.2 Compression test

Crack growth is investigated in a free swollen sample. The initial size of the sample is the result of free swelling in both directions. The resulting pre-strain is  $\epsilon_{ix} = \epsilon_{iy} = 1.2e-3$ . In Fig. 4.14b the distribution of the chemical potential is given at different time points. The movement of the piston results in initially straight crack growth which after a while deflects. At the crack-tip a pressure gradient over the crack exists. Four states of pre-

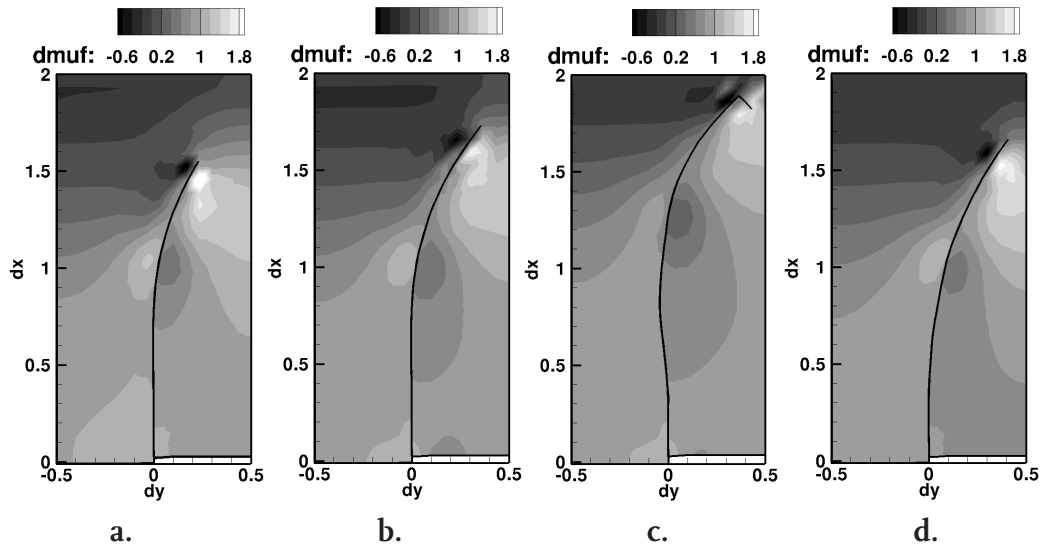


**Figure 4.14:** Distribution of chemical potential **a.** for no fixed charges ( $\epsilon_i = 0$ ,  $dt = 12.5$  s), and for prestress in **b.** both directions ( $\epsilon_i \ll 0$ ,  $dt = 16.6$  s) **c.**  $x$ -direction only ( $\epsilon_{ix} \ll 0$ ,  $dt = 23.3$  s) **d.**  $y$ -direction only ( $\epsilon_{iy} \ll 0$ ,  $dt = 18.9$  s). Crack-path is independent of mesh. Results depend on prestress.

stress is shown: no fixed charges, free swelling, constrained swelling in  $y$ -direction only ( $\epsilon_{iy} = 1.5e-3$  and  $\epsilon_{ix} = 0$ ) and constrained swelling in  $x$ -direction ( $\epsilon_{ix} = 1.5e-3$  and  $\epsilon_{iy} = 0$ ) are considered. With prestress in  $y$  direction, the crack propagates relatively straight longer than with prestress in  $x$ -direction only. Considering the total load the piston exhibits, Fig. 4.16a, it is seen that to displace the piston, the load needed increases nonlinearly.

A closer look to freeze the fields at the crack at time point  $dt = 15$  s gives extra information on the field, Fig. 4.15. In all cases a wave in chemical potential is seen.

For the prestress in only  $y$ -direction more load is needed to reach the same displacement, but the specimen fails faster too, 4.16b. Prestress in both directions or none at all have a growth pattern in between and hardly deviate from each other in crack path. The cases with prestress start with negative load. Finally in all cases failure occurs, i.e. load is not transferred anymore. The fluid flow evolution in case of free swelling is considered across the crack  $\vec{q} \cdot \vec{n}^+$  for two points, in the initial crack ( $dx = 0.28$  mm) and in the crack ( $dx = 0.48$  mm), Fig. 4.17. The flow in the initial crack is nonzero. Every time the

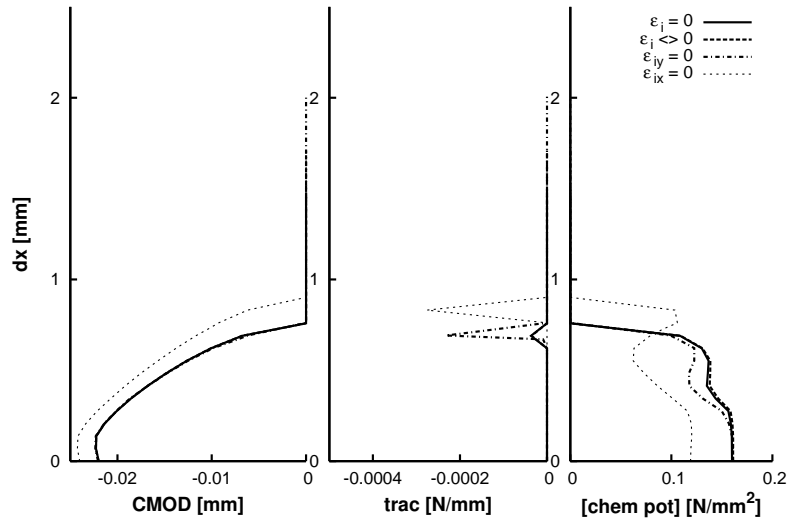


**Figure 4.15:** Distribution of crack mouth opening displacement (CMOD), traction forces (trac) and chemical potential (chem pot) for delamination in space at  $dt = 100$  s.

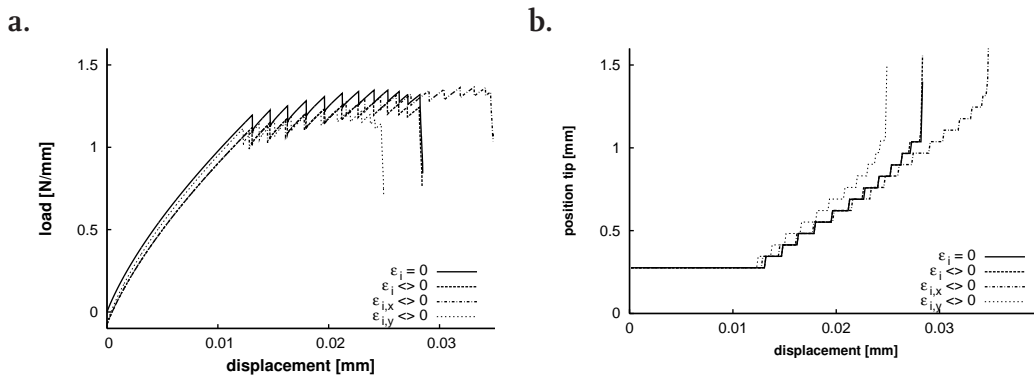


**Figure 4.16:** a. Piston displacement versus load. Prestress in  $x$ -direction only grows longest. b. Piston displacement versus crack length. Prestress in only  $y$ -direction causes a faster growth, but shorter crack path.

crack propagates a peak in flow takes place which is also felt in the already existing crack. The crack grows for several elements after which stress is built up again and in which the flow relaxes. The fluid flow is nonzero from start. When the local permeability is taken constant and similar to bulk permeability ( $k_d = K_d$ ), the overall crack propagation is not changed much, but fluid exchange is lower and more slowly initiated. When the permeability is taken much lower, there is hardly any fluid flow.

Loading with a larger rate (0.06 N/mm/s) needs a larger load to displace the piston than in the standard case with rate 0.03 N/mm/s, but the specimen fails earlier. Crack growth causes higher peaks in flow when the rate is increased. There are two types of discretization sensitivity: in time and in space. Decreasing the time discretization by a factor 4 does not have any influence on bulk and crack behavior. Therefore the time step is sufficiently

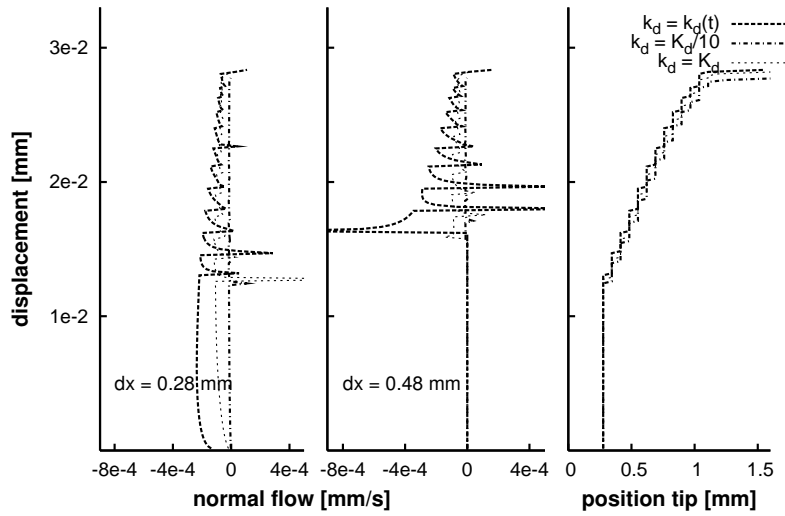


**Figure 4.17:** Normal flow for free swelling along the crack at points  $dx = 0.28$  mm and  $dx = 0.48$  mm. Crack growth causes a peak in flow after which relaxation takes place. The use of the unresolved hydraulic permeability ( $k_d = k_d(t)$ ) results in a nonzero initial flow and high peaks in case of growth followed by relaxation.

small. Decreasing the mesh discretization size by a factor two, does not have a negligible effect. Decreasing the mesh size, but keeping the nonlocal length  $l_a$  (Eq. (4.32)) constant, increases the amount of integration points over which the stress at the crack-tip is averaged. The result is that the stress at the crack-tip is lower and therefore crack growth is slightly slower, but more constant. This has effect on the fluid flow. Decreasing the nonlocal length and the discretization size by a factor 2 causes faster crack growth.

## 4.6 Discussion

A small strains framework has been derived to investigate shear fracture in ionized porous media. The method has been verified by analytical solution, showing its capabilities and limitations. Crack propagation is demonstrated to alternate with pressure diffusion across the crack resulting in a stepwise propagation of the fracture. The initial state of swelling affects the rate and the direction of crack propagation.

Two important factors are different with respect to other papers [7,82]. Firstly, osmotic conditions and prestress have been taken into account in the model. Secondly, the unresolved permeability is introduced to allow fluid flow across the crack surfaces.

A strong assumption has been made on the enhanced chemical potential field. A jump in the chemical potential has been assumed to account for steep gradients near borders. The verification method shows that a jump as approximation for steep gradients seems reasonable. Réthoré [82] confirms that this assumption is physically feasible, since forcing pressure discontinuity zero leads to cavities. Using jumps as approximation for

steep gradient contributes to robustness of the calculations. The role of the chemical potential in the traction forces, equation (4.26) was not taken into account in the work by Réthoré [82]. This term is negligible in shear loading. Some robustness was lost by the use of bilinear elements in space and linear in pressure. The influence of this was not seen in testing of the continuum element, nor is the effect seen in discontinuous elements. Improving the element might improve accuracy and robustness.

The bulk behavior has been verified by a 1-D confined compression test and a 2-D unconfined compression test. For the verification of the implementation of the material including crack and the constitutive model, a two-edge dislocation is impulsively induced by prescribing the displacement at the crack. Figure 4.8 shows oscillations. Changing the time discretization did not decrease the oscillations. A remedy against oscillations could be the use of asymptotic crack-tip solutions.

The plotted stress is the stress at the integration points. This results in a slight numerical underestimation of the shear stress. A better approximation would be the use of Gaussian interpolation as used for yield stress analysis. Nevertheless, with mesh refinement the numerical solution converges to the analytical shear stress. Spatial and time distribution is captured well for the finest mesh, Figs. 4.8 and 4.9.

The influence of the unresolved hydraulic permeability is low on the shear stress distribution in space, although the consolidation behavior is affected largely. Figure 4.10 shows that overshoot takes place when unresolved hydraulic permeability is taken constant. The performance of the mass balance at the crack is genuinely tested when the flow over the crack surface is considered. Behavior in time, Fig. 4.11, shows that the use of a unresolved hydraulic permeability with relaxation, Eq. (4.25), performs better than the use of a constant permeability. It captures the flow better, but there is a difference in maximum flow. This is the result of the error in space.

The method is prepared for crack propagation with cohesive zone modeling. With cohesive zone model stress singularity is decreased by damage evolution. Therefore the (cohesive) crack-tip is not enhanced, i.e. jumps are zero. The effect of zero jump in the chemical potential at the crack-tip (Fig. 4.12) enforces an underestimation of the flow across the crack surface compared to the analytical solution. While for the analytical solution the flow is maximum at the crack-tips, numerically it is zero since  $q_{\mu,i} = 0$  for the nodes of the crack tips. The numerical crack is therefore actually smaller than the analytical crack length. The constitutive relation of the flow at the discontinuity matches the averaged (resolved) flow at the discontinuity well. This confirms flow over the crack surfaces has been enabled. The match can be further improved by adding a factor in the local constitutive behavior Eq. (4.25). The results show that the numerical flow matches the analytical flow as well as previous calculations [51], but the singularity of the shear stress is captured better, Fig. 4.13. Since the shear stress drives the propagation, a large improvement has been made.

The two-edge dislocation test is a test which causes a higher singularity at the crack-tip than usually used in fracture mechanics. It does show that capturing a dislocation in a solid is difficult, but capturing the fluid flow as result of the dislocation is even more difficult. It also shows that fluid flow over the crack is possible.

A compression test was considered to investigate the effect of fluid flow and prestress on the crack growth. For this purpose an exponential cohesive law was used to mimic micro damage ahead of the crack-tip. The choice of cohesive law has a small influence on crack propagation. This is a property of the cohesive zone [20]. The cohesive zone model has to be validated with experiments.

Maximum shear stress criterion was used to initiate damage. This criterion does not differentiate between compression and tension. In this case failure takes place under compression. This is not uncommon in soils, for example failure of soils under a concrete pile. Furthermore, compression tests are the most common tests for soil experiments [64]. Mesh-dependency was not overcome completely, but trends were similar. Especially the nonlocal length, Eq. (4.32), had a large influence on crack growth. This is logical, since this length determines the singularity of the stress field at the crack-tip.

The pressure distributions in Fig. 4.14, show that crack path is mesh-independent. While a structured rectangular mesh has been used, the crack path undergoes a curvature. The angle of growth is clearly not prescribed. The result is strongly dependent on prestress, this has also been seen in solids [77]. A prestress in only  $x$ -direction causes the crack to grow straight longer. Prestress in only  $y$ -direction causes the crack to grow earlier but also to be shorter (Fig. 4.16), since it deflects faster. Prestress in both directions or none at all does not give rise to different crack patterns. The prestress hardly influences crack growth in homogeneous case, has a clear influence when the prestress is not homogeneously distributed.

Previous results were general results which mostly depended on the constitutive modeling of the solid, locally and globally. When the unresolved hydraulic permeability in the mass balance at the discontinuity is considered, Fig. 4.17, it is seen that the choice for the unresolved hydraulic permeability does not influence the crack growth rate so much, but it has a large influence on the fluid flow.

A low and constant hydraulic permeability results in zero flow over the crack. In the other cases, growth causes a peak in flow, which is felt before the crack-tip, decreasing with length to the current crack-tip. The time-dependent unresolved hydraulic permeability  $k_d = k_d(t)$  causes a nonzero flow over the crack surface in the initial crack ( $dx = 0.28$  mm) which resolves in time. For  $k_d = K_d$  this flow is initially zero and grows to a magnitude much lower than the previous case except for a large peak arises when crack growth takes place for the first time. The time-dependent unresolved hydraulic permeability  $k_d = k_d(t)$  causes a nonzero flow over the crack surface in the initial crack ( $dx = 0.28$  mm) which resolves in time. Under compression, effective stress is built up and the fluid is pushed away. Upon growth, stress is released and with that pressure. The fluid flows back. Crack growth alternates with fluid relaxation.





## CHAPTER FIVE

# Weak discontinuity model for the fluid for tensile loading in saturated ionized porous media<sup>I</sup>.

---

<sup>I</sup> *To be published*: F. Kraaijeveld, J. M. Huyghe, J. J. C. Remmers, R. de Borst, F. P. T. Baaijens, (2009). A mesh-independent model for mode-I fracture in osmoelastic saturated porous media. *Int. J. Num. Meth. Eng.* [52]

## 5.1 Introduction

In the previous chapter fracture growth in ionized porous media has been studied for shear failure. In this chapter the focus is on tensile failure. In tensile loading, fluid flow in the crack occurs due to deformation of the bulk material and opening of the crack. Examples of tensile failure are delamination, such as in the annulus of the intervertebral disc or in material test experiments, failure of concrete dams, pressurized well bores and hydraulic fracturing. In all these cases a strong coupling exists between fluid pressure and crack propagation. Numerical simulation techniques describing the fracture propagation coupled to the fluid exchange between the fracture and the formation are highly desirable to enhance the understanding of the process of tensile failure.

An example of failure in ionized porous media is intervertebral disc (IVD) herniation. The etiology of intervertebral disc herniation is largely unknown. IVD tissue is avascular and therefore ages relatively fast [100]. During ageing, the disc changes in size, structure and osmotic prestress. Furthermore the number of cracks grow [3,100]. While some papers suggest that herniation is the result of weakening of the disc due to ageing [42,95,96], others believe that fast ageing is the cascading effect of an initial disruption [19,113]. Genetic studies actually suggest that occupation (i.e. loading history) is of less influence than familiarity [11,105]. Wognum et al. [111] showed that cracks open under decreasing osmotic pressure (i.e. ageing) which causes stress localization at the crack-tip.

This could also be a mechanism for borehole instability [33], a second example for failure in ionized porous media.

Fluid-driven fracture propagation in ionized porous media is an example for failure in porous media which is desired. The fracturing of tight sand is needed in order to win gas at commercial rates. For the modeling of fluid-driven fractures analytical solutions have been developed [25,41,84]. More specifically, hydraulic fracturing in porous media [17,34] is considered a benchmark. Detournay and Garagash [27] combined analytical and numerical analysis to show that fluid-driven fracture depends on permeability and propagation velocity for unsaturated porous media. Derivations of these solutions demanded simplifications, such as no or minimal fluid exchange between crack and material.

Understanding of the relation between fracture and fluid flow is needed for commercial and medical applications.

Homogenization and upscaling techniques in porous media have been used [28,49], but these are suitable to study damage evolution when there is no prominent crack to be distinguished. Full fracture calculations for a macro crack in porous media were performed in a FE setting from the 1990s. Boone et al. [17] introduced interface elements equipped with the cohesive zone model by Dugdale [30] and Barenblatt [10] for the fracturing process in a poro-elastic setting. They studied stress testing with water to initiate micro-cracking for a known path. The use of interface elements is suitable if the crack path is known a priori, since it requires a priori alignment of the element with the

crack path.

Adaptive remeshing methods have been combined cohesive zone models [89,94]. These methods are able to capture fracture evolution in nonhomogeneous porous materials without assumptions about the singularities of the solid and fluid fields. Unfortunately, the adaptive remeshing schemes are computationally expensive and require suitable mapping procedures [89,93].

Alternatively, fractures are introduced in a mesh free way by exploiting the partition of unity property of the finite element shape functions [9]. Fractures are represented by a discontinuity in the displacement field. A discontinuity is introduced in the FEM by adding an enhanced (discontinuous) field to the standard displacement field. The number of degrees of freedom at the nodes whose support is crossed by a discontinuity, are increased. Therefore no new nodes are added during propagation and no dummy stiffness is required. Belytschko [12] introduced this method together with an asymptotic enhancement of the displacement field at the crack-tip. Practical benefits of exploiting the partition of unity method are that standard discretization is used and that crack propagation is independent of the discretization.

The partition of unity approach has been combined in solid mechanics with cohesive zone models allowing the cohesive zone run through the continuum elements [70,80,107].

Strong discontinuity concept has been introduced in porous media by Larsson et al. [58,59] by the introduction of a regularized Dirac distribution function to the pressure field at the location of the discontinuity for shear banding in an enhanced strains approach. In a different approach, Armero and Callari [7] assume continuous flow and have suggested that a dilatant response of the discontinuity would result into a discontinuity in the fluid flow.

Along the same lines, Roels et al. [85] used the partition of unity method to simulate crack propagation in the solid part combined with moisture transfer scheme. The progress of the moisture front in the fracture is calculated separately from the mechanical behavior by a quasi-static pressure equation together with a Darcian flux equation with permeability related to opening. Results show that the solution for the fluid phase smoothed upon mesh refinement, since a fine mesh is needed to capture the steep change increase of capillary pressure field and corresponding decrease in permeability.

Al-Khoury et al. [4] used the partition of unity approach in combination with a strong discontinuity for the solid phase combined with a double porosity model for the fluid phase. The equations solved as one single system. The fluid flow in the crack is coupled to fracture in the solid phase by a leakage term. Unfortunately only one-dimensional examples have been addressed. It is unclear how the model will behave in two dimensions. Réthoré et al. [22,83] used partition of unity approach with strong discontinuity model for the solid phase and a weak discontinuity model for the fluid phase. Fracture and fluid flow is related by a cavity model, which relates the opening to flow in the fracture assuming viscous fluid in the cavity. Only static cases have been considered, but they show mesh-independency of the fluid phase.

All aforementioned papers have shown that the partition of unity approach is suitable for

studying crack growth in porous media. While treatment of the solid phase is straightforward, there is no consensus on the treatment of the fluid flow as result of a displacement discontinuity, nor have osmotic forces been taken into account.

In this chapter a framework for mesh-independent fracturing in ionized porous media under tensile loading is introduced. Lanir's plane strain osmoelastic model [56] for small deformations is used to model the bulk material. This model represents the bulk effect of the presence of ions, but assumes that the ion flow is fast compared to fluid diffusion. For this paper the partition of unity approach is used to introduce strong discontinuities in the displacement field. The strong gradients in the pressure at fractures made us decide to introduce a weak discontinuity for the chemical potential field. This approach is combined with cohesive zone modeling [80] for damage evolution. A direct coupling between fluid flow in the crack, in the formation and between the formation and the crack, and coupling to ionization is formulated. Several examples are considered, both with and without an external mechanical load. The effect of prestress in the bulk material on fracture propagation is considered.

## 5.2 Governing equations

The governing equations consist of equations for the bulk and for the discontinuity, dominated by mass balance, momentum balance and constitutive behavior. Figure 4.1 shows a body  $\Omega$  with external boundary  $\Gamma$  with a traction force on  $\Gamma_t$  and fluid supply on  $\Gamma_f$ , with  $\vec{n}$  the normal unit vector on the boundary  $\Gamma$  directed outwards. The body is cut by a discontinuity  $\Gamma_d$  in two domains,  $\Omega^+$  and  $\Omega^-$ . The normal of the discontinuity  $\vec{n}^+$  is directed towards  $\Omega^+$ .

Ionized porous media is dominated by deformation, i.e. displacement  $\vec{u}$ , and fluid flow, i.e. the chemical potential  $\mu^f$ . The governing equations for the bulk are defined in section 4.2 and chapter 2.

### 5.2.1 Discontinuity kinematics

By exploiting the partition of unity principle [9], the displacement field and the chemical potential distribution is separated into two different scales: the bulk behavior (standard field) and crack behavior (enhanced field). The partition of unity principle is given by equation (4.14). As in chapter 4, the displacement field  $\vec{u}$  of the body is additively decomposed into the standard or continuous part  $\hat{\vec{u}}$  and the enhanced part  $\tilde{\vec{u}}$ .

$$\vec{u}(\vec{x}) = \hat{\vec{u}}(\vec{x}, t) + \mathcal{H}_{\Gamma_d}(\vec{x})\tilde{\vec{u}}(\vec{x}, t) \quad (5.1)$$

The Heaviside function  $\mathcal{H}_{\Gamma_d}$  is defined by (5.2) with the jump at the middle of the discontinuity.

$$\mathcal{H}_{\Gamma_d} = \begin{cases} +h/2 & \vec{x} \in \Omega^+ \\ -h/2 & \vec{x} \in \Omega^- \end{cases} \quad (5.2)$$

The Heaviside function is acting on smooth function  $\tilde{u}(\vec{x}, t)$  and allows for continuity of the crack surface. The jump at the discontinuity  $\Gamma_d$  is given by  $[\vec{u}]$  and represents the opening of the crack (shear or normal opening).

$$[\vec{u}(\vec{x}, t)] = h\tilde{u}(\vec{x}, t), \quad \vec{x} \in \Gamma_d. \quad (5.3)$$

with  $h = \mathcal{H}_{\Gamma_d}^+ - \mathcal{H}_{\Gamma_d}^-$  the magnitude of the jump of the Heaviside function.

Opening of a crack causes a high gradient in the chemical potential at both crack surfaces. In opening mode there is no pressure difference between the crack surfaces but a pressure difference between the crack surface and the middle of the crack, as shown in Fig. 5.1. Using the partition of unity property, a distance function  $\mathcal{D}_{\Gamma_d}$  similar to Réthoré

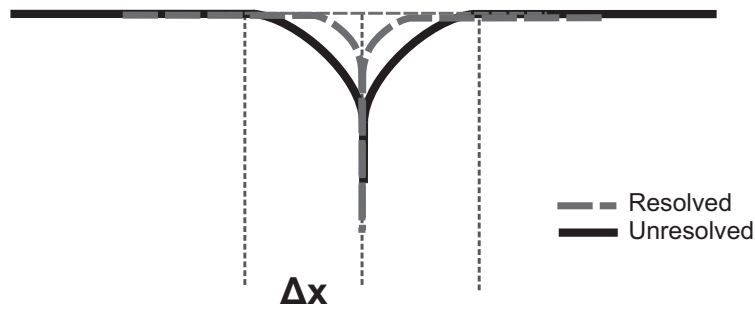


**Figure 5.1:** Distribution of chemical potential as result of crack growth. Crack growth causes an instant peak in flow at the location of the crack (dark grey). This is approximated by a weak discontinuity (lighter grey).

et al. [83] (Fig. 5.2) is introduced. This function allows for the natural introduction of steep gradients without enforcing it. In this case the decomposition becomes

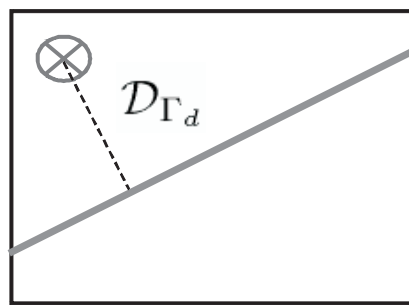


**Figure 5.2:** Distance function for simulating a weak discontinuity.

$$\mu^f(\vec{x}) = \hat{\mu}^f(\vec{x}, t) + \mathcal{D}_{\Gamma_d}(\vec{x})\tilde{\mu}^f(\vec{x}, t) \quad (5.4)$$

The distance function is defined with respect to the coordinates of the crack  $\vec{x}_\Gamma$ , namely by

$$\mathcal{D}_{\Gamma_d} = \frac{h}{2}|(\vec{x} - \vec{x}_\Gamma) \cdot \vec{n}^+|, \quad \vec{x} \in \Omega \quad (5.5)$$

with  $h$  the magnitude of the Heaviside jump. The gradient of the distance function  $\vec{\partial}\mathcal{D}$  is given by

$$\vec{\partial}\mathcal{D} = \vec{\nabla}^s \mathcal{D}_{\Gamma_d} = \begin{cases} \frac{h}{2}\vec{n}^+ & \vec{x} \in \Omega^+ \\ \frac{h}{2}\vec{n}^- & \vec{x} \in \Omega^- \end{cases} = \mathcal{H}_{\Gamma_d} \vec{n}^+ \quad (5.6)$$

where  $\vec{\nabla}^s \vec{u} = 1/2\{\vec{\nabla}\vec{u} + (\vec{\nabla}\vec{u})^T\}$  holds. The effect of the strong and discontinuous functions are represented in 1D by Fig. 5.3. The Heaviside function causes the a discontinuous distribution with a jump at the location of the crack and a linear distribution away from the crack (Fig. 5.3a). The distance function causes a continuous distribution of the chemical potential with a nonlinear distribution of the chemical potential away from the crack.

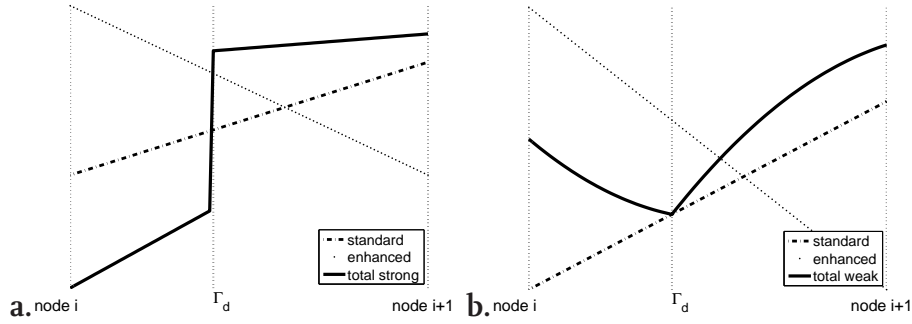


**Figure 5.3:** A 1-D representation of the effect of **a.** the Heaviside function and **b.** the distance function. The total field is the additive result of the standard field and the enhanced field.

## 5.2.2 Local behavior

A local coordinate system  $(n,s)$  is introduced where index  $n$  denotes the normal component directed to  $\Omega^+$  and  $t$  denotes the tangential component directed towards direction of propagation. A displacement jump is decoupled into

$$[\vec{u}] = [u]_n \vec{n}^+ + [u]_s \vec{t}^+ \quad (5.7)$$

with  $\vec{n}^+ = -\vec{n}^-$  directed into the body and  $\vec{t}^+$  is directed along the crack surface in direction of propagation. We define crack surfaces  $\Gamma^+ = \partial\Omega^+ \cap \Gamma_d$  and  $\Gamma^- = \partial\Omega^- \cap \Gamma_d$ .

### Local mass balance

Deformation around the discontinuity is strongly linked to fluid flow. Fluid flow takes place at the surface of the discontinuity from the medium into the crack and a flow along the crack when opening of the crack increases. When the crack is closed, the normal fluid flow  $f_c^\pm$  over surface  $\Gamma_d^\pm$  determines the amount of fluid exchange. When the crack opens, additional terms are included. Figure 5.4 shows a schematic overview of the local mass balance. In case of tensile mode, there is a balance between tangential flow and

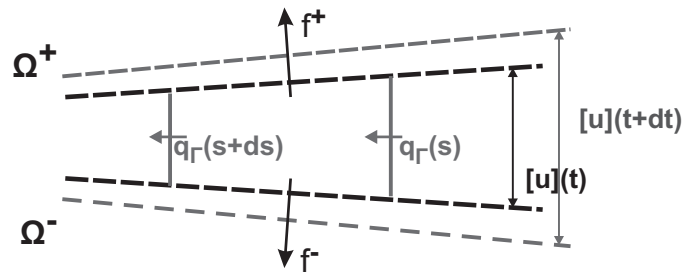


**Figure 5.4:** Schematic representation of the fluid flow at the crack surface with parameter  $s$  the distance along the crack.

normal flow.

$$\begin{aligned} \vec{q}_\Gamma \cdot \vec{n}^+ + \vec{q}_\Gamma \cdot \vec{n}^- &= f_\Gamma^+ + f_\Gamma^- = -\frac{\partial \vec{q}_\Gamma \cdot \vec{t}^+}{\partial s} - [\dot{u}]_n, \\ \vec{q}_\Gamma \cdot \vec{t}^+ &= -|[u]_n|^k K_d \frac{\partial \mu_\Gamma^f}{\partial s}. \end{aligned} \quad (5.8)$$

where  $s$  represents the distance along the crack, with  $s = 0$  the crack-tip and  $s$  positive in direction of  $\vec{t}^+$ . Tangential flow is assumed Couette flow.

### Local momentum balance

A discrete crack is preceded by local damage. This micro-damage is lumped into one constitutive relation (cohesive zone) and projected on the crack [80], Fig. 1.7. The model relates the decohesion, i.e. softening of the traction forces, as result of opening of the crack. At each crack surface, the following relation holds

$$(\sigma_e - (\mu^f + \Delta\pi)\mathbf{I})^\pm \cdot \vec{n}^\pm = \vec{t}_\Gamma^\pm(\vec{x}, t), \quad \vec{x} \in \Gamma^\pm \quad (5.9)$$

This is represented in Fig. 5.5. The cohesive law holds locally and is described in local coordinate system of the discontinuity. The cohesive zone model is nonlinear and a function of the effective stress. The system is linearized in order to use the Newton-Rhapson procedure. The transition from local coordinates to global coordinates occurs through a mapping  $\underline{Q}$ , Eq. (4.29). The change in traction forces  $\Delta \vec{t}_\Gamma^\pm$  in local coordinates is expressed in terms of enhanced nodal displacements.

$$\Delta \vec{t}_\Gamma^+ = \underline{Q} \underline{T}_{e,d} \underline{Q}^T \vec{u} - (\mu^f + \Delta\pi)^+ \vec{n}^+ \quad (5.10)$$



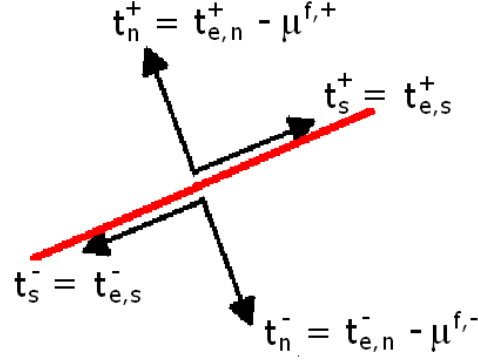


Figure 5.5: Schematic representation of the traction forces at the crack surface

Then the tangent stiffness in element coordinates is given by  $\underline{T}_e = \underline{Q}\underline{T}_{e,d}\underline{Q}^T$ , Eq. (5.10). Furthermore for the osmotic forces in the crack surfaces holds that the ionic concentration in the crack is the same as in the external reservoir.

$$\mu_\Gamma^f = p_\Gamma - 2RTc^{\text{ex}}, \Delta\pi^+ = 0, \quad (5.11)$$

with  $p_\Gamma$  hydraulic pressure in the crack.

### Yield criterion

Crack growth is determined by the stress state in the solid matrix. Therefore the yield criterion, next to the cohesive zone, is related to the effective stress. The effective stress at the crack-tip varies locally, therefore the critical effective stress state is calculated non-locally using Eq. (4.32) from the stress states around the crack-tip. A length scale  $l_a$  is introduced which determines the influence radius and steepness of surrounding stress states.

The damage takes place in the solid part, therefore the cohesive law only applies to the effective stress. The crack-tip is assumed drained. According to the principle of normality, fracture will initiate perpendicular to maximum principal stress. This principal stress criterion has shown to be effective, but does not differentiate between compressive and tensile stresses. Furthermore the contribution of shear stresses and tensile stresses are of equal importance.

Therefore Remmers et al. [80] introduced a different yield law based on Camacho and Ortiz [20]. The principal stresses and associated angle  $\alpha_n$  is calculated from the effective stress state according to

$$\sigma_{e1,2} = \frac{\sigma_{\text{ex}} - \sigma_{\text{ey}}}{2} \pm \sqrt{\left(\frac{\sigma_{\text{ex}} - \sigma_{\text{ey}}}{2}\right)^2 + \sigma_{\text{exy}}^2} \quad (5.12)$$

The stress state is transformed into normal and shear traction forces  $t_{e,n} = \vec{n}^+ \cdot \sigma_e \cdot \vec{n}^+$  and  $t_{e,s} = \vec{t}^+ \cdot \sigma_e \cdot \vec{t}^+$ . An equivalent traction  $t_{\text{eq}}(\alpha)$ , with  $\alpha$  the to be determined angle,

is introduced such that

$$t_{e,eq}(\alpha) = \sqrt{\langle t_{e,n}(\alpha) \rangle^2 + \frac{1}{\beta} \langle t_{e,s}(\alpha) \rangle^2}, \quad (5.13)$$

with  $\langle x \rangle$  McCauley brackets, i.e.  $x = 0$  if  $x < 0$ .  $\beta$  is typically set to 2.3 [20] and the angle is limited to  $0 < \alpha < \pi$ . Crack propagation is initiated when the equivalent traction force ( $t_{eq}$ ) is larger than the critical value  $t_{ult}$ . In the examples the contribution of the tangential traction forces will be low.

## 5.3 Numerical description

The weak form for the Finite Element Method is derived by standard Galerkin approach. Then the weak equations are discretized leading to a time-dependent, non-linear system. This is solved using a Crank-Nicholson scheme for time-integration and Newton-Rhapson iteration within each time increment.

### 5.3.1 Weak form

The momentum balance and mass balance are multiplied by test functions and subsequently integrated over the domain  $\Omega$ . These test functions are taken of the same form as the shape functions for the independent variables and therefore consisting for a continuous and discontinuous field. The displacements are enhanced with a strong discontinuity function. The chemical potential is enhanced with a weak discontinuity function.

$$\vec{\eta} = \hat{\eta} + \mathcal{H}_{\Gamma_d} \tilde{\eta}, \quad \varphi = \hat{\varphi} + \mathcal{D}_{\Gamma_d} \tilde{\varphi}. \quad (5.14)$$

Using integration by parts the discontinuity is introduced as a boundary integral. This is more elaborated at the specific balance equations in the next section.

### Momentum balance

The momentum equation after applying integration by parts is given by

$$\begin{aligned} \int_{\Omega^+ \cup \Omega^-} \vec{\nabla}^s (\hat{\eta} + \mathcal{H}_{\Gamma_d} \tilde{\eta}) : \sigma d\Omega &= \int_{\Gamma_t} (\hat{\eta} + \mathcal{H}_{\Gamma_d} \tilde{\eta}) \cdot \vec{t}_t d\Gamma \\ - \int_{\Gamma_d^+} (\hat{\eta} + \mathcal{H}_{\Gamma_d} \tilde{\eta}) \cdot \vec{t}_\Gamma^+ d\Gamma &- \int_{\Gamma_d^-} (\hat{\eta} + \mathcal{H}_{\Gamma_d} \tilde{\eta}) \cdot \vec{t}_\Gamma^- d\Gamma \end{aligned} \quad (5.15)$$

with  $\sigma = \sigma_e - p\mathbf{I}$ ,  $p = \mu^f + \Delta\pi$ . Note that  $\vec{n}$  is directed outward and  $\vec{n}^\pm$  inward. This equation must hold for all variations of test functions, therefore it holds also if  $\hat{\eta} = \vec{0}$  or if  $\tilde{\eta} = \vec{0}$ . Both options are separately applied. This results in two equations. The

first equation denotes the standard or continuous field behavior (taking  $\tilde{\eta} = \vec{0}$  and momentum balance demands  $\vec{t}_\Gamma^+ = -\vec{t}_\Gamma^-$ ). Then in total the next momentum balance for continuous field is found

$$\int_{\Omega^+ \cup \Omega^-} \vec{\nabla}^s \hat{\eta} : \sigma d\Omega = \int_{\Gamma_t} \hat{\eta} \cdot \vec{t}_t d\Gamma \quad (5.16)$$

The second equation denotes the behavior of the enhanced field (taking  $\hat{\eta} = \vec{0}$ ). With  $t_\Gamma^\pm = \vec{t}_e^\pm - \mu_\Gamma^f \vec{n}^\pm$ , the momentum balance for enhanced field is:

$$\int_{\Omega^+ \cup \Omega^-} \mathcal{H}_{\Gamma_d} \vec{\nabla}^s \tilde{\eta} : \sigma d\Omega + \int_{\Gamma_d^+} \tilde{\eta} \cdot h(\vec{t}_e^+ - \mu_\Gamma^f \vec{n}^+) d\Gamma = \int_{\Gamma_t} \mathcal{H}_{\Gamma_d} \tilde{\eta} \cdot \vec{t}_t d\Gamma \quad (5.17)$$

The result is similar to the case of shear fracture, with the total chemical potential at the crack surface equal to the chemical potential of the fluid in the crack.

### Mass balance

The variational mass balance is given by

$$\begin{aligned} & \int_{\Omega^+ \cup \Omega^-} \vec{\nabla}(\hat{\phi} + \mathcal{D}_{\Gamma_d} \tilde{\phi}) \cdot \vec{q} d\Omega - \int_{\Omega^+ \cup \Omega^-} (\hat{\phi} + \mathcal{D}_{\Gamma_d} \tilde{\phi}) \vec{\nabla} \cdot \dot{u} d\Omega \\ & = \int_{\Gamma_f} (\hat{\phi} + \mathcal{D}_{\Gamma_d} \tilde{\phi}) f_t d\Gamma - \int_{\Gamma_d^+} (\hat{\phi} + \mathcal{D}_{\Gamma_d} \tilde{\phi}) \vec{q} \cdot \vec{n}^+ d\Gamma - \int_{\Gamma_d^-} (\hat{\phi} + \mathcal{D}_{\Gamma_d} \tilde{\phi}) \vec{q} \cdot \vec{n}^- d\Gamma \end{aligned} \quad (5.18)$$

Taking  $\tilde{\phi} = 0$ , the mass balance for the continuous field becomes

$$\begin{aligned} & \int_{\Omega^+ \cup \Omega^-} \vec{\nabla} \hat{\phi} \cdot \vec{q} d\Omega - \int_{\Omega^+ \cup \Omega^-} \hat{\phi} \vec{\nabla} \cdot \dot{u} d\Omega + \int_{\Gamma_d^+} \hat{\phi} \vec{q} \cdot \vec{n}^+ d\Gamma \\ & + \int_{\Gamma_d^-} \hat{\phi} \vec{q} \cdot \vec{n}^- d\Gamma = \int_{\Gamma_f} \hat{\phi} f_t d\Gamma \end{aligned} \quad (5.19)$$

For the flow around the crack holds (5.8). In variational form this reduces to:

$$\int_{\Gamma_d^+} \hat{\phi} \vec{q} \cdot \vec{n}^+ d\Gamma + \int_{\Gamma_d^-} \hat{\phi} \vec{q} \cdot \vec{n}^- d\Gamma = - \int_{\Gamma_d} \hat{\phi} \frac{\partial q_\Gamma}{\partial s} d\Gamma - \int_{\Gamma_d^+} \hat{\phi} [\dot{u}] \cdot \vec{n}^+ d\Gamma \quad (5.20)$$

The term with tangential flow is simplified using divergence theorem

$$\int_{\Gamma_d} \hat{\phi} \frac{\partial q_\Gamma}{\partial s} d\Gamma = - \int_{\Gamma_d} \frac{\partial \hat{\phi}}{\partial s} q_\Gamma d\Gamma + \hat{\phi} q_\Gamma |_{s_d} \quad (5.21)$$

Combining Eqs. (5.20) and (5.21) with (5.19), the mass balance for continuous field is found:

$$\begin{aligned} & \int_{\Omega^+ \cup \Omega^-} \vec{\nabla} \hat{\phi} \cdot \vec{q} d\Omega - \int_{\Omega^+ \cup \Omega^-} \hat{\phi} \vec{\nabla} \cdot \dot{u} d\Omega \\ & + \int_{\Gamma_d} \frac{\partial \hat{\phi}}{\partial s} q_\Gamma d\Gamma - \int_{\Gamma_d} \hat{\phi} [\dot{u}] \cdot \vec{n}^+ d\Gamma = \int_{\Gamma_f} \hat{\phi} f_t d\Gamma + \hat{\phi} q_\Gamma |_{s_d} \end{aligned} \quad (5.22)$$

The local mass balance arises in this case in the continuous mass equations, while in case of shear loading, chapter 4, the local mass balance arises in the enhanced mass equations. This means that the mass balance at the crack contributes to the total mass balance of the continuous field. This result is not surprising since the chemical potential field is continuous across the crack.

Using  $\hat{\varphi} = 0$  and  $\mathcal{D}_{\Gamma_d} = 0$  on  $\Gamma_d$ , the mass balance for the enhanced field is equal to

$$\int_{\Omega^+ \cup \Omega^-} \vec{\nabla}(\mathcal{D}_{\Gamma_d} \varphi) \cdot \vec{q} d\Omega - \int_{\Omega^+ \cup \Omega^-} (\mathcal{D}_{\Gamma_d} \varphi) \text{tr}(\dot{\epsilon}) d\Omega = \int_{\Gamma_f} (\mathcal{D}_{\Gamma_d} \varphi) f_f d\Gamma \quad (5.23)$$

### 5.3.2 Discretization

The discretization is separated into two parts, in space and in time.

#### Spatial discretization

The weak form is provided by equations (5.16), (5.17), (5.22) and (5.23). Discretized forms are derived by dividing body  $\Omega$  into elements  $\Omega_e, e = 1..n_e$  ( $\Omega = \bigcup_1^{n_e} \Omega_e$ ). The result is that the discontinuity is discretized in elements  $S_d$  and the boundary in elements  $S_e$ . The displacements, the chemical potential and their variations are discretized similarly (Bubnov-Galerkin approach) by

$$\begin{aligned} \hat{u} &= \vec{N}^T \vec{a}_u, & \tilde{u} &= \vec{N}^T \vec{b}_u \\ \hat{\mu}^f &= \vec{m}^T \vec{a}_\mu, & \tilde{\mu}^f &= \vec{m}^T \vec{b}_\mu \end{aligned} \quad (5.24)$$

where  $\vec{N} = [N_x \ N_y]$  contains the shape functions, which are the same in  $x$ - and  $y$ -direction. The columns  $\vec{a}_u$  and  $\vec{b}_u$  contain the nodal values for bulk part and enhanced part, resp.. Similar are  $\vec{m}$ ,  $\vec{a}_\mu$  and  $\vec{b}_\mu$  columns of shape functions and nodal values. Then strain is discretized by

$$\vec{\nabla}^s \epsilon = \underline{B} \vec{a}_u + \mathcal{H}_{\Gamma_d} \underline{B} \vec{b}_u \quad (5.25)$$

The first order differential operator on the displacement shape functions is denoted by  $\underline{B} = [\underline{L} N_x \ \underline{L} N_y]$  The matrix  $\underline{L}$  contains the differential operators:

$$\underline{L} = \begin{pmatrix} \frac{\partial}{\partial x} & 0 \\ 0 & \frac{\partial}{\partial y} \\ \frac{\partial}{\partial y} & \frac{\partial}{\partial x} \end{pmatrix} \quad (5.26)$$

Furthermore  $\underline{C} = \underline{L}^T (\vec{l} m^T)$  a  $2 \times m$  matrix is defined with  $\vec{l} = (1 \ 1 \ 0)^T$ . Then  $\underline{B}^T \cdot (\vec{l} m^T) = \vec{N} \underline{C}$  holds and  $\vec{\nabla} \mu^f = \underline{C} \vec{a}_\mu + \mathcal{H}_{\Gamma_d} \underline{C} \vec{b}_\mu$ .

Finally the stress and flux are discretized. The stress consist of the effective stress and the chemical potential. The effective stress in vector notation is given by  $\underline{\sigma}_e = (\sigma_{e,xx}, \sigma_{e,yy}, \sigma_{e,xy})^T$ . The stress is linearized with respect to the column of nodal values such that a Newton-Rhapson scheme can be used.

$$\begin{aligned}\underline{\sigma} &= \frac{\partial \sigma}{\partial \underline{\epsilon}} \frac{\partial \underline{\epsilon}}{\partial \underline{a}_u} \underline{a}_u + \frac{\partial \sigma}{\partial \underline{\epsilon}} \frac{\partial \underline{\epsilon}}{\partial \underline{b}_u} \underline{b}_u + \frac{\partial \sigma}{\partial \underline{a}_\mu} a_\mu + \frac{\partial \sigma}{\partial \underline{b}_\mu} b_\mu \\ &= \underline{DB} \underline{a}_u + \mathcal{H}_{\Gamma_d} \underline{DB} \underline{b}_u - (\underline{l} \underline{m}^T) a_\mu - \mathcal{H}_{\Gamma_d} (\underline{l} \underline{m}^T) b_\mu\end{aligned}\quad (5.27)$$

Here  $\underline{D}$  is a (3x3) matrix for 2-D. The matrix  $\underline{D}$  is defined as follows ( $c = 2\mu + \lambda + \frac{\partial \Delta \pi}{\partial \text{tr}(\underline{\epsilon})}$ ).

$$\underline{D} = \begin{pmatrix} c & (c - 2\mu) & 0 \\ (c - 2\mu) & c & 0 \\ 0 & 0 & 2\mu \end{pmatrix}\quad (5.28)$$

The traction forces at the discontinuity  $S_d$  are discretized as

$$(\underline{\sigma}_e - (\mu^f + \Delta \pi) \mathbf{I}) \cdot \underline{n}^+ = \underline{t}_\Gamma^+ = h \underline{T} \underline{N}^T \underline{b}_u - \underline{n}^+ \underline{m}^T a_\mu\quad (5.29)$$

with  $\underline{T}_e = \underline{Q} \underline{T}_{e,d} \underline{Q}$  the tangent stiffness of the cohesive zone. The seepage flux is linearized by

$$\begin{aligned}\Delta \underline{q} &= \frac{\partial \underline{q}}{\partial \underline{a}_u} \cdot \underline{a}_u + \frac{\partial \underline{q}}{\partial \underline{b}_u} \cdot \underline{b}_u + \frac{\partial \underline{q}}{\partial a_\mu} a_\mu + \frac{\partial \underline{q}}{\partial b_\mu} b_\mu \\ &= -\underline{K} \underline{C} a_\mu - \underline{K} (\underline{D}_{\Gamma_d} \underline{C} + \partial \underline{D}_{\Gamma_d} \underline{m}^T) b_\mu\end{aligned}\quad (5.30)$$

Finally, linearization of the local mass elements, results is the next elements.

$$\begin{aligned}\int_{S_d^+} \frac{\partial \varphi}{\partial \eta} \underline{q}_\Gamma \cdot \underline{t}^+ d\Gamma &= \int_{S_d^+} \frac{\partial \underline{m}}{\partial \eta} |[\underline{u}_i]^T \underline{n}^+|^k K_d \frac{\partial \underline{m}}{\partial \eta} d\Gamma a_\mu \\ &\quad + \int_{S_d^+} \frac{\partial \underline{m}}{\partial \eta} K_d \frac{\partial \mu_i^f}{\partial \eta} k |[\underline{u}_i]^T \underline{n}^+|^{k-1} \text{sgn}([\underline{u}_i] \cdot \underline{n}^+) (\underline{n}^+)^T \underline{N}^T d\Gamma \underline{b}_u \\ \varphi \underline{q}_\Gamma \cdot \underline{t}^+ |_{S_d^+} &= \underline{m} \underline{q}_\Gamma \cdot \underline{t}^+ |_{S_d^+}\end{aligned}\quad (5.31)$$

### Time discretization

To solve the system of equations, a time stepping algorithm is required. The solution is sensitive to the magnitude of the time increment (time step). A large step leads to under estimation of fluid pressure in confined compression. Taking too small steps leads to initial oscillation. For stable time integration the next law has to be satisfied [103]:

$$\Delta t > \frac{\Delta x^2}{cK}.\quad (5.32)$$

While the time needed for the fluid to propagate a distance  $\Delta x$  is related to the the square of the distance, permeability of the framework and the stiffness of the framework. In this model the Cranck-Nicholson scheme is used. This means that differential terms are approximated linearly by looking at the difference between the new and old step

$$\frac{\partial *}{\partial t} = \frac{(*)^{n+1} - (*)^n}{\Delta t} \quad (5.33)$$

and values of the independent variables are weighted results of the new and old time step

$$(*) = \theta(*)^{n+1} + (1 - \theta)(*)^n \quad (5.34)$$

Furthermore stabilization is reached if implicit time stepping is used ( $\theta \geq 0.5$ , for instance by taking the first time increment  $\theta = 1$  and the rest  $\theta = 0.5$ . Taking  $\theta = 1$  reduces the method to Euler implicit.

### 5.3.3 Total system

The governing equations and discontinuity equations reduce to system (5.35). Although the bulk material is assumed linear elastic, the presence of damage introduces nonlinearity. The system is therefore solved iteratively at each time step. The solution procedure is driven by time. In the examples the displacement is increased monotonically. Snap-back can occur due to non-uniqueness of the solution. Define  $\vec{c}_u = ( \vec{a}_u^T \quad \vec{b}_u^T )^T$  a  $4n \times 1$  vector and  $\vec{c}_\mu = ( \vec{a}_\mu^T \quad \vec{b}_\mu^T )^T$  a  $2m \times 1$  vector.

In the equations subscript  $i$  denotes the temporary solution  $\vec{c}_i$  in iteration step  $i$  and superscript  $n$  denotes the solution  $\vec{c}^n$  of previous time step  $n$ .

---

#### Newton-Rhapson solution procedure with Cranck-Nicholson

- **Step 0:**  $\vec{c}_0 = \vec{c}^n$

- **Step i+1:**

– If no convergence solve

$$\begin{pmatrix} \underline{K}_{uu,i} & -\underline{K}_{u^-,i} \\ -\underline{K}_{-u,i} & -\Delta t \theta \underline{K}_{-,i} \end{pmatrix} \delta \vec{c}_i = \begin{pmatrix} f_{\text{ext},u} - f_{\text{int},u} \\ \Delta t f_{\text{ext},-}^\theta - \Delta t f_{\text{int},-}^\theta \end{pmatrix} \quad (5.35)$$

–  $\vec{c}_{i+1} = \vec{c}_i + \delta \vec{c}_i, i = i + 1$

- **Final iteration step:**  $\vec{c}^{n+1} = \vec{c}^n + \sum_i \delta \vec{c}_i$
-

The matrices involved are given below.

$$\begin{aligned}
\underline{K}_{uu,i} &= \begin{pmatrix} \int_{\Omega_e} \underline{B}^T \underline{D}_i \underline{B} d\Omega & \int_{\Omega_e} \mathcal{H}_{\Gamma_d} \underline{B}^T \underline{D}_i \underline{B} d\Omega \\ \int_{\Omega_e} \mathcal{H}_{\Gamma_d} \underline{B}^T \underline{D}_i \underline{B} d\Omega & \int_{\Omega_e} \mathcal{H}_{\Gamma_d}^2 \underline{B}^T \underline{D}_i \underline{B} d\Omega + \underline{M}_{uu,i} \end{pmatrix} \\
\underline{K}_{-i} &= \begin{pmatrix} \int_{\Omega_e} \underline{C}^T \underline{K}_i \underline{C} d\Omega + \underline{M}_{-i} & \int_{\Omega_e} \underline{C}^T \underline{K}_i (\mathcal{D}_{\Gamma_d} \underline{C} + \partial \vec{\mathcal{D}} \underline{m}^T) d\Omega \\ \int_{\Omega_e} (\mathcal{D}_{\Gamma_d} \underline{C} + \partial \vec{\mathcal{D}} \underline{m}^T)^T \underline{K}_i \underline{C} d\Omega & \int_{\Omega_e} (\mathcal{D}_{\Gamma_d} \underline{C} + \partial \vec{\mathcal{D}} \underline{m}^T)^T \underline{C}^T \underline{K}_i (\mathcal{D}_{\Gamma_d} \underline{C} + \partial \vec{\mathcal{D}} \underline{m}^T) d\Omega \end{pmatrix} \\
\underline{K}_{u\mu} &= \begin{pmatrix} \int_{\Omega_e} \vec{N} \underline{C} d\Omega & \int_{\Omega_e} \vec{N} (\mathcal{D}_{\Gamma_d} \underline{C} + \partial \vec{\mathcal{D}} \underline{m}^T) d\Omega \\ \int_{\Omega_e} \mathcal{H}_{\Gamma_d} \vec{N} \underline{C} d\Omega + \underline{M}_{u\mu,i} & \int_{\Omega_e} \mathcal{H}_{\Gamma_d} \vec{N} (\mathcal{D}_{\Gamma_d} \underline{C} + \partial \vec{\mathcal{D}} \underline{m}^T) d\Omega \end{pmatrix} \\
\underline{K}_{\mu u} &= \begin{pmatrix} \int_{\Omega_e} \underline{C}^T \vec{N}^T d\Omega & \int_{\Omega_e} (\mathcal{D}_{\Gamma_d} \underline{C} + \partial \vec{\mathcal{D}} \underline{m}^T)^T \vec{N}^T d\Omega + \underline{M}_{u\mu,i}^T + \underline{M}_{\mu u,i} \\ \int_{\Omega_e} \mathcal{H}_{\Gamma_d} \underline{C}^T \vec{N}^T d\Omega & \int_{\Omega_e} \mathcal{H}_{\Gamma_d} (\mathcal{D}_{\Gamma_d} \underline{C} + \partial \vec{\mathcal{D}} \underline{m}^T)^T \vec{N}^T d\Omega \end{pmatrix},
\end{aligned} \tag{5.36}$$

$$\begin{aligned}
\underline{M}_{uu,i} &= h^2 \int_{S_d} \vec{N} \underline{T}_i \vec{N}^T d\Gamma = h^2 \int_{S_d} \vec{N} \underline{T}_{e,i} \vec{N}^T d\Gamma \\
\underline{M}_{u\mu,i} &= h \int_{S_d} \vec{N} \vec{n}^+ \underline{m}^T d\Gamma \\
\underline{M}_{\mu\mu,i} &= \int_{S_d} \frac{\partial \underline{m}}{\partial \eta} |[\vec{u}]^T \vec{n}^+|^k K_d \frac{\partial \underline{m}^T}{\partial \eta} d\Gamma \\
\underline{M}_{\mu u,i} &= h \int_{S_d} \frac{\partial \underline{m}}{\partial \eta} K_d \frac{\partial \underline{m}_i^T}{\partial \eta} k |[\vec{u}]^T \vec{n}^+|^{k-1} \text{sgn}([\vec{u}_i]^T \vec{n}^+) (\vec{n}^+)^T \vec{N}^T d\Gamma
\end{aligned} \tag{5.37}$$

and

$$\begin{aligned}
\underline{f}_{int,u} &= \begin{pmatrix} \int_{\Omega_e} \underline{B}^T \bar{\sigma}_i d\Omega \\ \int_{\Omega_e} \mathcal{H}_{\Gamma_d} \underline{B}^T \bar{\sigma}_i d\Omega + \int_{\Gamma_d} \vec{N} \bar{t}_{\Gamma,i}^+ d\Gamma \end{pmatrix} \\
\underline{f}_{int,\mu}^\theta &= \begin{pmatrix} \int_{\Omega_e} \underline{C}^T (\theta \vec{q}_i + (1-\theta) \vec{q}^n) d\Omega - \int_{\Omega_e} \underline{C}^T \frac{\vec{u}_i - \vec{u}^n}{\Delta t} d\Omega \\ - \int_{S_d} \underline{C}^T \frac{[\vec{u}] \cdot \vec{n}^+ - [\vec{u}]^n \cdot \vec{n}^+}{\Delta t} d\Gamma + \int_{S_d} \frac{\partial \underline{m}}{\partial s} (\theta q_{\Gamma,i} + (1-\theta) q_\Gamma^n) d\Gamma \end{pmatrix}, \\
\underline{f}_{ext,u} &= \begin{pmatrix} \int_{\Gamma_t} \vec{N} \bar{t}_t^{n+1} d\Gamma \\ \int_{\Gamma_t} \mathcal{H}_{\Gamma_d} \vec{N} \bar{t}_t^{n+1} d\Gamma \end{pmatrix} \\
\underline{f}_{ext,-}^\theta &= \begin{pmatrix} \int_{S_f} \underline{m} (\theta f_f^{n+1} - (1-\theta) f_f^n) d\Gamma + \theta \underline{m} q_\Gamma^{n+1}|_{S_d} + (1-\theta) \underline{m} q_\Gamma^n|_{S_d} \\ \int_{\Gamma_f} \mathcal{D}_{\Gamma_d} \underline{m} (\theta f_f^{n+1} - (1-\theta) f_f^n) d\Gamma \end{pmatrix}
\end{aligned} \tag{5.38}$$

Newton-Rhapson iterations are stopped when the error  $\epsilon_{ex}$  is less than the given precision  $\epsilon_{in}$ , using an euclidian norm  $\|x\| = \sqrt{\sum_i x_i^2}$

$$\begin{aligned}
\underline{Res} &= \underline{f}_{int} - \underline{f}_{ext}' \\
\epsilon_{ex} &= \begin{cases} \|\underline{Res}\| / \|\underline{f}_{int}\| & \text{if } \|\underline{f}_{int}\| > 0 \\ \|\underline{Res}\| * \|\underline{f}_{int}\| & \text{if } \|\underline{f}_{int}\| \leq 0 \end{cases}
\end{aligned} \tag{5.39}$$

Even though matrices  $\underline{D}$ ,  $\underline{K}$ ,  $\underline{T}_e$  are symmetric,  $\underline{M}_{\mu u,i}$  and  $\underline{M}_{u\mu,i}$  cause asymmetry of the system. This is not a problem for the solution method.

The model has been programmed using the Jem/Jive finite element toolkit which has been developed by Habanera. For implementation aspects like the tracking of the crack-tip, increasing the degrees of freedom or other propagation issues we refer to Remmers et al. [78,80,81] and appendix B.

## 5.4 Numerical examples

In the example a cohesive law is used for the damage evolution, i.e. softening behavior after reaching the critical stress state. Defined is critical length  $\delta_n = \mathcal{G}_c / \tau_{ult}$ , with  $\tau_{ult}$  the ultimate traction forces and  $\mathcal{G}_c$  fracture toughness. The cohesive law is then for positive opening

$$t_n = \tau_{ult} e^{-\left(\frac{[u]_n}{\delta_n}\right)}, [u]_n \geq 0. \quad (5.40)$$

This is shown in Fig. 5.6. Note that the surface underneath the curve is the fracture

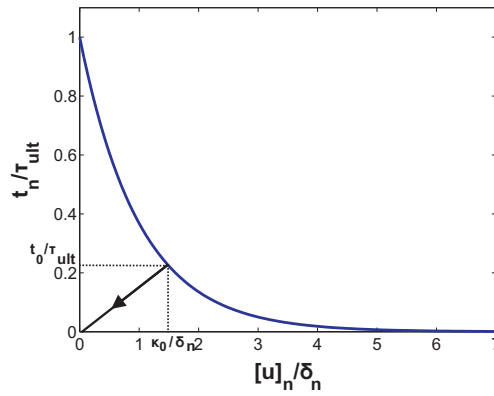


**Figure 5.6:** Normalized distribution of the exponential cohesive law for tensile loading related traction forces and displacement.

toughness  $\mathcal{G}_c$ :

$$\begin{aligned} \int_{-\infty}^{\infty} t_n d[u]_n &= \int_0^{\infty} t_n d[u]_n \\ &= \tau_{ult} \delta_n \int_0^{\infty} e^{-r} dr = \tau_{ult} \delta_n = \mathcal{G}_c. \end{aligned} \quad (5.41)$$

A history parameter  $\kappa$  is introduced in case of unloading each time step the current opening  $\kappa_0$  and traction  $\tau_0$  are remembered. When the new opening is smaller than previous, then unloading takes place according to

$$t_n = \frac{\tau_0}{\kappa_0} [u]_n. \quad (5.42)$$

Damage is defined as

$$D = 1 - \frac{t_n}{\tau_{ult}} \quad (5.43)$$

Macro crack is developed when the local damage approaches maximum ( $D = 1$ ), i.e. when the cohesive law approaches zero. When locally the opening decreases compared to previous time step unloading takes place. The cohesive law parameters  $\mathcal{G}_c$  and  $\tau_{ult}$  can be obtained from experimental data.



### 5.4.1 Delamination test

A delamination test is performed with a predefined angle of  $0^\circ$ . An initial defect of length 13 mm is inserted on the lefthandside, Fig. 5.7. The sample is fixed on the righthandside and is in contact with a filter ( $\mu^f = 0$ ). Crack propagation is initiated by pulling the sample on the top and bottom over approximate 8 mm with a fixed velocity of  $1.0e-3$  mm/s. The local fluid distribution is determined by Eq. 5.8.

The exact material properties are given in table 5.1. This means that  $2RT\Gamma c^{\text{ex}} =$

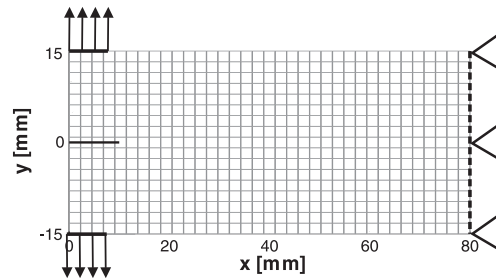


**Figure 5.7:** The mesh and boundary conditions for delamination consisting of 575 elements. Material is pulled at the top and bottom on the left and is on the right in contact with a filter.

$4.96 \text{ N/mm}^2$  holds. A time step of 0.1 s is used.

The influence of mesh refinement, prestress and local boundary conditions on the crack

**Table 5.1:** Material properties for delamination test.

$R$	$= 8.3145$	$[\text{N mm mmol}^{-1} \text{K}^{-1}]$	$T$	$= 298$	$[\text{K}]$
$E$	$= 1.4e+4$	$[\text{N/mm}^2]$	$\nu$	$= 0.33$	$[-]$
$\varphi_i^f$	$= 0.10$	$[-]$	$K$	$= 2.0e-1$	$[\text{mm}^4 \text{N}^{-1} \text{s}^{-1}]$
$c^{\text{ex}}$	$= 1.0e-3$	$[\text{mmol/mm}^3]$	$c_i^{\text{fc}}$	$= -1.0e-3$	$[\text{mmoleq/mm}^3]$
$K_d$	$= 2.0e-1$	$[\text{mm}^4 \text{N}^{-1} \text{s}^{-1}]$	$k$	$= 2$	$[-]$
$\mathcal{G}_c$	$= 0.020$	$[\text{N/mm}]$	$\tau_{ult}$	$= 1.1$	$[\text{N/mm}^2]$
$l_a$	$= 7.8$	$[\text{mm}]$	$v$	$= 1.0e-3$	$[\text{mm/s}]$

is considered on crack propagation and flow around the crack. For the mesh refinement, the mesh of Fig.5.7 is refined to 2701 elements. The corresponding time step is a quarter of the time step of the coarse mesh. For the influence of prestress four cases are compared, no prestress, prestress in both directions and prestress in either  $x$  or  $y$ -direction (Fig. 4.7). The modes of prestress are the result of different initial swellings, not the result of uneven distribution of fixed charges. Furthermore, the influence of local mass balance is considered by decreasing the local permeability with respect to the standard case or prescribing the chemical potential in the crack.

### 5.4.2 Pull test

In the second case a pull test is considered with yield criterion based on optimal principal stress. An initial defect of approximately 22 mm is inserted in the middle, Fig. 5.8. The material is fixed at the bottom and is pulled at the top with constant speed. The material is in contact with a filter at the sides ( $\mu^f = 0$ ). Crack propagation is initiated by loading the sample over the complete width with a fixed velocity of  $5.0e-4$  mm/s. A time step of  $dt = 0.1$  s is used. In this second case the angle of growth is not prescribed. To ensure

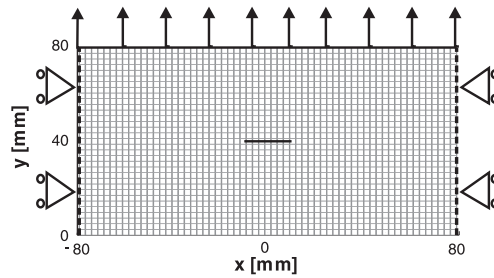


**Figure 5.8:** The mesh and boundary conditions for pull test: material is pulled at the top with bottom fixed and at sides in contact with a filter.

**Table 5.2:** Material properties for pull test.

$R$	$= 8.3145$	$[\text{N mm mmol}^{-1} \text{K}^{-1}]$	$T$	$= 298$	$[\text{K}]$
$E$	$= 1.4e+3$	$[\text{N/mm}^2]$	$\nu$	$= 0.33$	$[-]$
$\varphi_i^f$	$= 0.10$	$[-]$	$K$	$= 1.0e-3$	$[\text{mm}^4 \text{N}^{-1} \text{s}^{-1}]$
$c^{\text{ex}}$	$= 1.0e-3$	$[\text{mmol/mm}^3]$	$c_i^{\text{fc}}$	$= -1.0e-3$	$[\text{mmoleq/mm}^3]$
$K_d$	$= 1.0e-3$	$[\text{mm}^4 \text{N}^{-1} \text{s}^{-1}]$	$k$	$= 2$	$[-]$
$\mathcal{G}_c$	$= 2.0e-2$	$[\text{N/mm}]$	$\tau_{ult}$	$= 1.1$	$[\text{N/mm}^2]$
$l_a$	$= 7.8$	$[\text{mm}]$	$v$	$= 5.0e-4$	$[\text{mm/s}]$

growth only under tension, equivalent traction forces are used, with  $\beta = 2.3$ , Eq. (5.13). Similarly to delamination, the influence of prestress and local mass balance is considered.

### 5.4.3 Osmolarity test

As a last example, a test is performed in which the effect of decreasing osmotic pressure is considered on a crack with length  $\approx 18$  mm at the rim of the material. For that purpose the external salt concentration is increased, i.e. the chemical potential on the boundaries is decreased. The material is fixed at the top, right side and bottom to a filter which alters the chemical potential by  $-0.4e-3$  N/mm<sup>2</sup>.

$$\Delta\mu^f = \Delta\pi(c_i^{\text{ex}} + \Delta c^{\text{ex}}) - \Delta\pi(\Delta c^{\text{ex}}). \quad (5.44)$$

This means that the external salt concentration is increased from initial state by  $\Delta c^{\text{ex}} = 4.82e-7t$ . A time step of 8.0 s is used. The exact material properties are given in table 5.3.

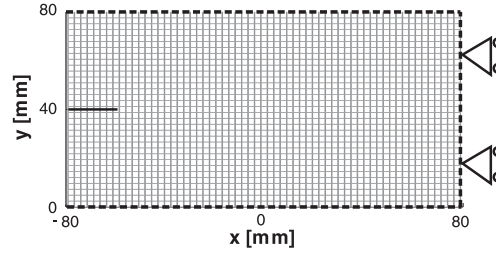


**Figure 5.9:** The mesh and boundary conditions for the osmolarity test: the material is fixed at bottom, right and top and is in contact with a filter at these sides.

The influence of prestress is considered on crack propagation and flow around the crack.

**Table 5.3:** Material properties for osmolarity test.

$R$	$=$	8.3145	$[\text{N mm mmol}^{-1} \text{K}^{-1}]$	$T$	$=$	298	$[\text{K}]$
$E$	$=$	90.0	$[\text{N/mm}^2]$	$\nu$	$=$	0.2	$[-]$
$\varphi_i^f$	$=$	0.80	$[-]$	$K$	$=$	2.8e-4	$[\text{mm}^4 \text{N}^{-1} \text{s}^{-1}]$
$c^{\text{ex}}$	$=$	0.15e-3	$[\text{mmol/mm}^3]$	$c_i^{\text{fc}}$	$=$	-0.2e-3	$[\text{mmoleq/mm}^3]$
$K_d$	$=$	2.8e-4	$[\text{mm}^4 \text{N}^{-1} \text{s}^{-1}]$	$k$	$=$	2	$[-]$
$\mathcal{G}_c$	$=$	0.2e-2	$[\text{N/mm}]$	$\tau_{ult}$	$=$	0.25	$[\text{N/mm}^2]$
$l_a$	$=$	7.8	$[\text{mm}]$	$\Delta\mu^f$	$=$	-0.4e-3	$[\text{N/mm}^2]$

## 5.5 Results

### 5.5.1 Delamination test

The presence of fixed charges causes an initial strain of  $\epsilon_{i,x} = \epsilon_{i,y} = 1.9\text{e-}5$  in case of prestress in both direction and an initial strain of  $2.8\text{e-}5$  when only prestressed in one direction. A weak interface criterion causes straight growth for all cases.

Considering the chemical potential distribution, Fig. 5.10, the figures show localization at the crack-tip with a negative chemical potential. This low chemical potential is relaxed by fluid redistribution towards the crack-tip. The chemical potential is largest at the left due to largest opening of the crack.

Figure 5.11 shows the fracture length versus the pull displacement. Crack growth occurs

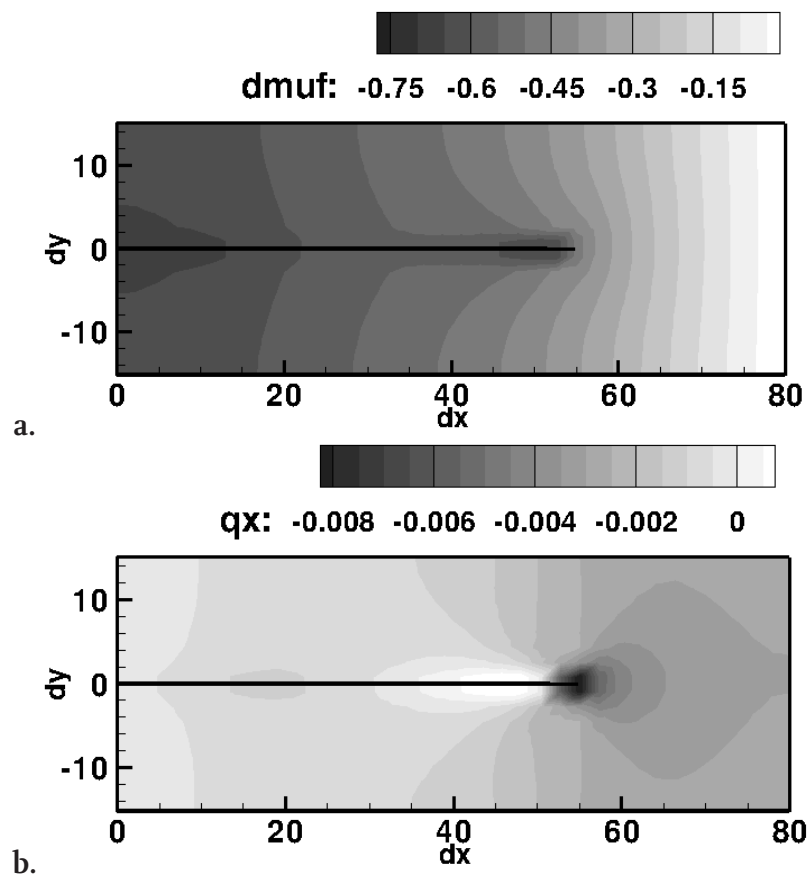


**Figure 5.10:** Delamination in case of prestress in both directions after 950 time increments (i.e.  $9.5\text{e-}2$  mm displacement of top boundary). Distribution of **a.** chemical potential in  $[\text{N}/\text{mm}^2]$  and **b.** flow in  $x$ -direction in  $[\text{mm}/\text{s}]$ .

slightly faster in the case of prestress. With further opening of the crack, the chemical potential decreases and the tangential flow increases. Numerical oscillations seem to be present, but the oscillations are actual changes in chemical potential due to crack growth

and redistribution of load. These changes are less in the case of prestress than when there is no prestress present. In addition in the case without prestress the growth seems more smoothly. Furthermore, the chemical potential is nonzero from the start in case of prestress. When fluid is not taken into account, crack growth occurs faster, while the time to damage initiation is almost the same as in the case with fluid present.

A closer look to the evolution of different fields at the crack at time point  $dt = 100$  s

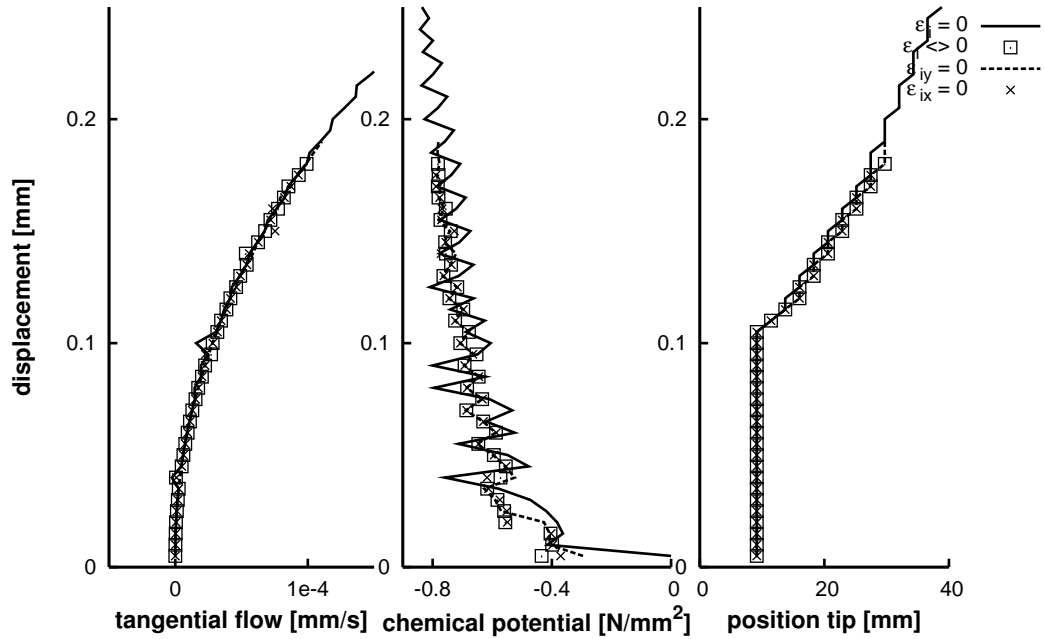


**Figure 5.11:** Comparison of the effect of prestress for delamination  $dx = 13.71$  mm (ahead of the initial crack) on tangential flow in the crack, chemical potential in the crack and crack growth against pull displacement at the top.

in space gives extra information, Fig. 5.12. In the case without prestress a large dip in chemical potential is seen at the crack-tip of the cohesive zone (where  $t_n = 0$ ,  $[u]_n = 0$ ).

In order to check the results, the spatial discretization is refined (from 575 to 2701 elements, "dx refine") and time discretization is refined without refining in space (from 0.5 s to 0.125 s, "dt refine"). Results are shown approximately at the same point (Fig. 5.13). It is evident that both in time and in space, the results are the same, except for the slight mismatch in space due to a mismatch in integration points between the coarse and fine mesh.

Finally, the influence of local mass balance is considered. Decreasing the crack permeability decreases the tangential flow. It does not alter the crack path dramatically. When assuming contact with an external reservoir (i.e.  $\mu_T^f = 0$ ), the flow is reversed with respect to the previous cases. The fluid distribution (Fig. 5.14) shows that the chemical potential is now highest in front of the macro crack, in stead of at the start of the macro crack such as in the previous cases.

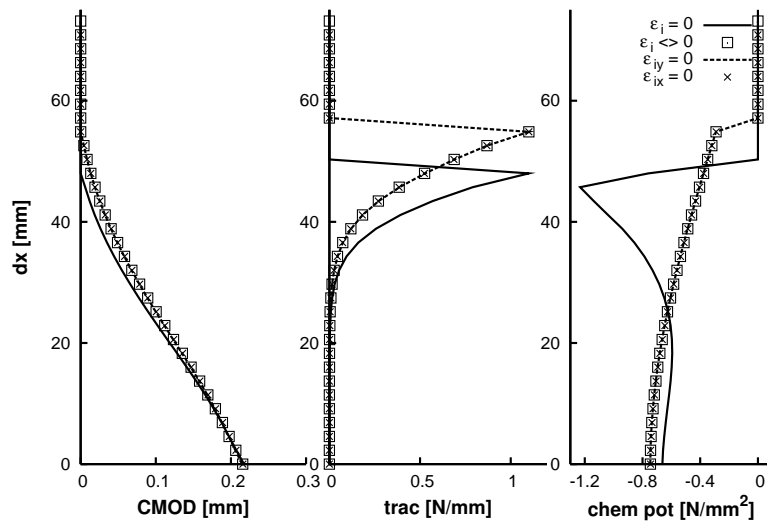


Figure 5.12: Distribution over plane of crack at  $dt = 100$  s of crack mouth opening displacement (CMOD), traction forces (trac) and chemical potential (chem pot) for delamination.

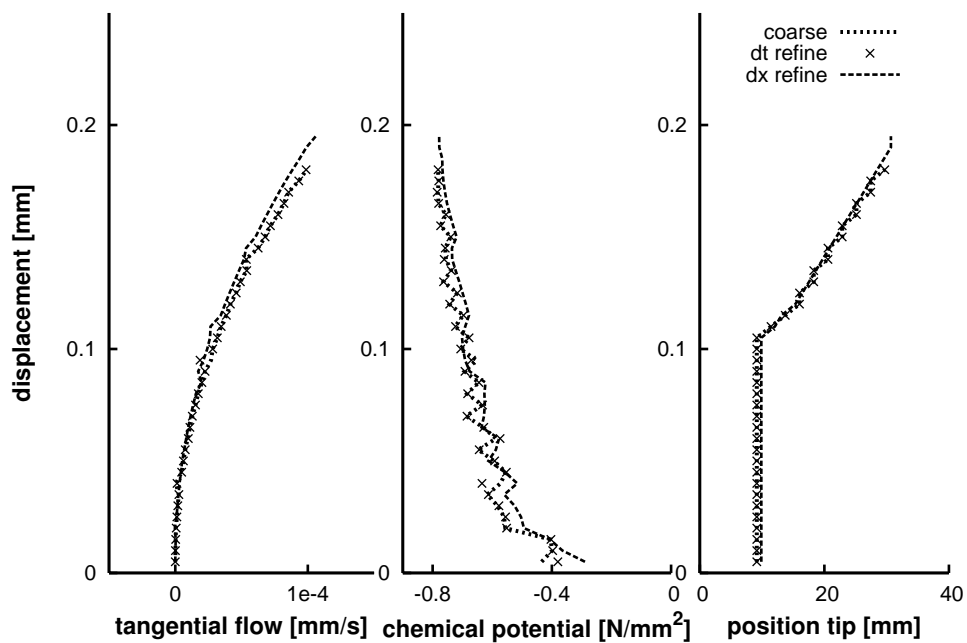
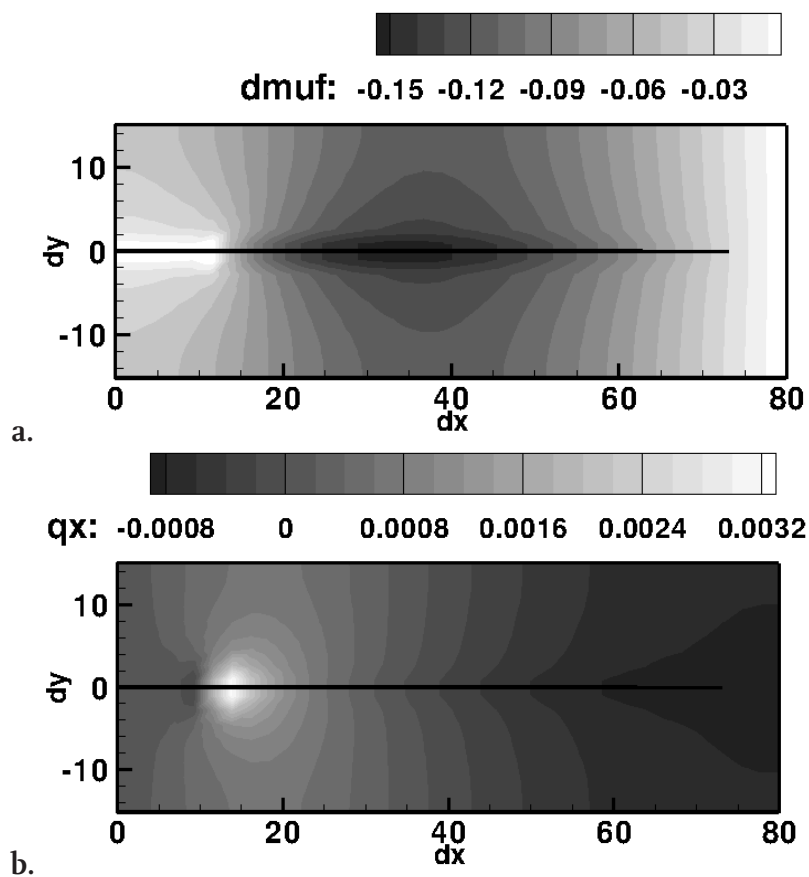


Figure 5.13: Comparison of the effect mesh- and time refinement for delamination at a point just ahead of the initial crack ( $dx = 13.71$  mm).



**Figure 5.14:** Distribution of chemical potential in  $[\text{N}/\text{mm}^2]$  for delamination in case of prestress in both directions and  $\mu_T^f = 0$  after 1100 increments (i.e. displacement of top boundary of  $du = 1.1\text{e-}2$  mm) for **a.** chemical potential and **b.** flow in  $x$ -direction.

### 5.5.2 Pull test

This case considers a less stiff material than for delamination. The prestress caused an initial strain of  $\epsilon_{i,x} = \epsilon_{i,y} = 1.9e-4$  in case of prestress in both directions and an initial strain of  $2.8e-4$  when prestressed in only one direction.

Figure 5.15 shows the chemical potential distribution and flow in case of prestress in both directions with crack growth. Even though the direction of crack growth is not predefined, the damage growth is almost straight. Localization takes place at both crack-tips with low chemical potential, Fig. 5.15a. Fluid is attracted from the left and right towards the crack. The stress field is the largest in the middle of the crack (Fig. 5.15b).

The displacement, tangential flow and chemical potential are considered almost in the

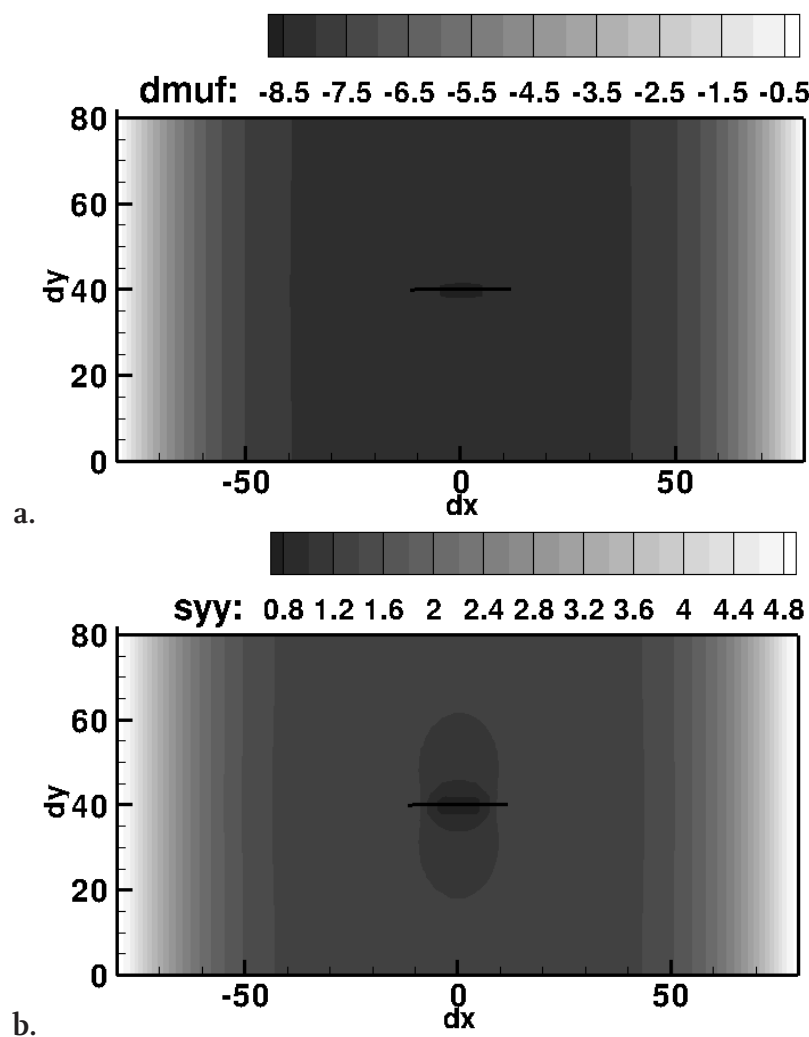


**Figure 5.15:** Distribution for pull test of a. chemical potential and b. stress component  $\sigma_{e,yy}$  for the pull test after 1010 increments (i.e.  $5.05e-2$  mm of pull displacement) in case of prestress in both directions including cohesive zone.

middle of the crack (Fig. 5.16). For all cases of osmotic prestress, the chemical potential



becomes more negative, though in the case without prestress the chemical potential decreases less.

In the case of prestress in  $x$ -direction only, a negative opening is seen at start and increases, which causes a wave in tangential flow. Furthermore, the time to crack initiation increases. When damage initiates, a steep increase in chemical potential is seen in the middle of the crack. Unfortunately, Newton-Rhapson does not converge anymore after several growth stages.

Trends do not alter under mesh and time discretization refinement. Lastly, changing

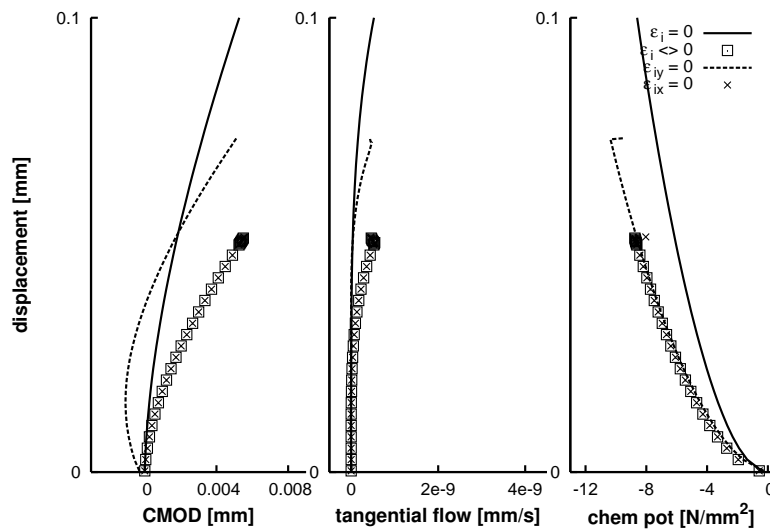


**Figure 5.16:** Comparison for the pull test of the effect of prestress on crack mouth opening displacement (CMOD), chemical potential and tangential flow in the crack at  $dx = 3.5$  mm.

the boundary condition at the crack to the boundary condition representing contact with a reservoir, oscillations were seen.

### 5.5.3 Osmolarity test

In this section a case without external loading is considered. The sample is subjected to an increase of external salt concentration. The result is a global decrease in chemical potential (Fig. 5.17a) and a local increase of stress ahead of the crack-tip (Fig. 5.17b).

The flow is considered in a close-up of the crack-tip (Fig. 5.18). Crack growth causes a local flow at the crack-tip directed towards the crack-tip (in  $x$ - and  $y$ -direction), while the flow away from the crack-tip is directed opposite in the crack.

This trend is seen for all cases with prestress, except for osmotic prestress in only  $x$ -direction. In that case a solution could not be found. Of the other two cases, damage progressed longest in case of prestress only in the  $y$ -direction. Furthermore, in case of prestress in both directions, opening of the crack is largest while chemical potential in

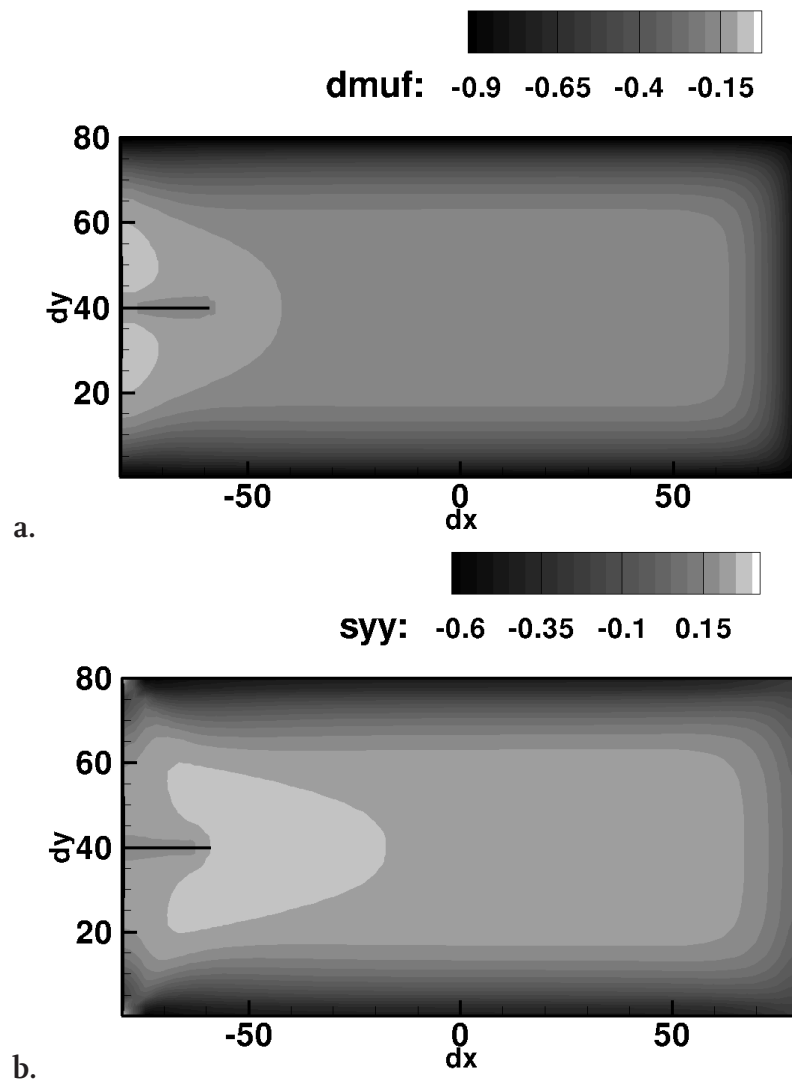


**Figure 5.17:** Distribution for the osmolarity test after 300 increments (i.e. a change in chemical potential of  $-0.96$  MPa) just before damage initiation for prestress in both directions for **a.** of chemical potential and **b.** of stress component  $\sigma_{e,yy}$ .

the crack is smallest. This pattern is seen throughout time. The fact that the curve for prestress in only  $y$ -direction is longer than in case of prestress in both directions, but with zero values, means that damage has occurred but not evolved.

## 5.6 Discussion

In this chapter a small strains numerical model has been derived to study the interplay between prestressing of the solid material, fluid flow and mode-I crack propagation for

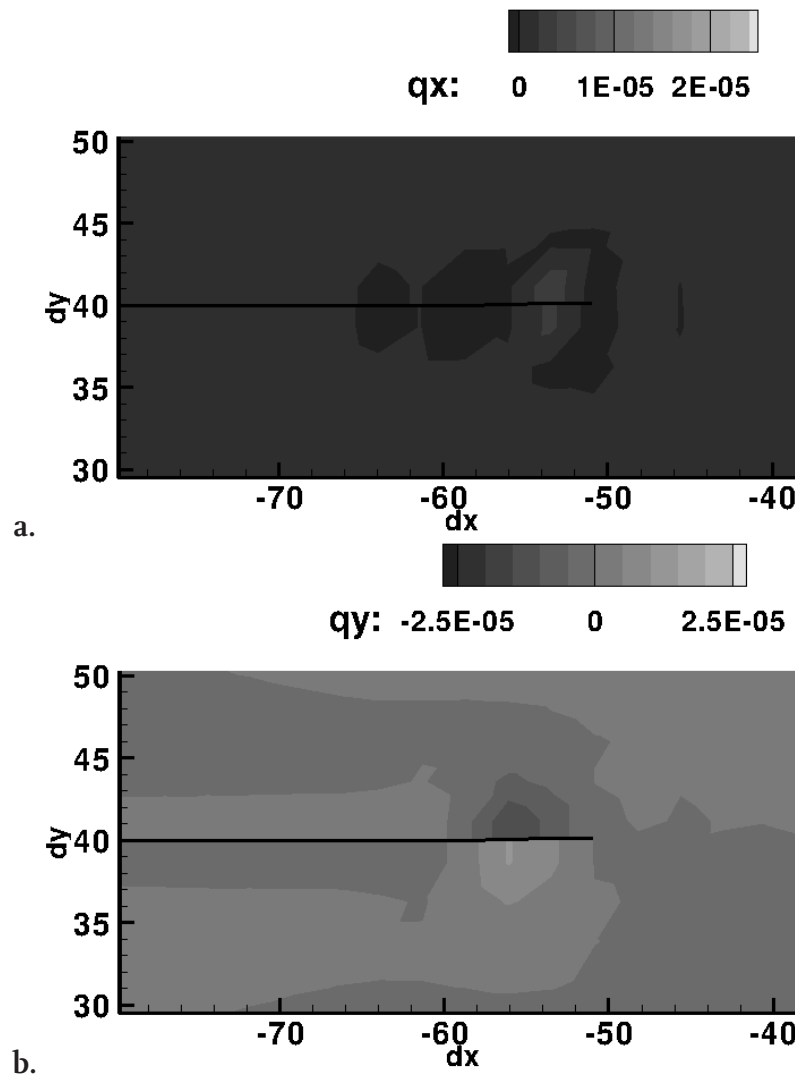


**Figure 5.18:** Distribution at the crack-tip for osmolarity test of flow for prestress in both directions after 306 increments (i.e. a change in chemical potential of  $-0.98$  MPa) just after damage initiation **a.** in  $x$ -directions and **b.**  $y$ -direction.

ionized porous media. The partition of unity approach is used to integrate cracks into the FEM. A strong discontinuity is inserted in the displacement field by enhancing the field by the Heaviside function. A weak discontinuity is inserted in the field of chemical potential via a distance function to capture the high gradient in this field.

The results are meant to indicate trends rather than yielding quantitative predictions. The model captures local trends well. A profound influence is seen of the fluid phase on the crack propagation in the solid. The presence of fluid slows down crack initiation and propagation. The flow from the surrounding medium causes an increase in volumetric strain at the crack-tip, and hence an increase of the (tensile) effective stress at the crack-tip. This increase triggers damage and possible further crack propagation. Upon crack propagation a local change in flow direction is seen. The deformation around the

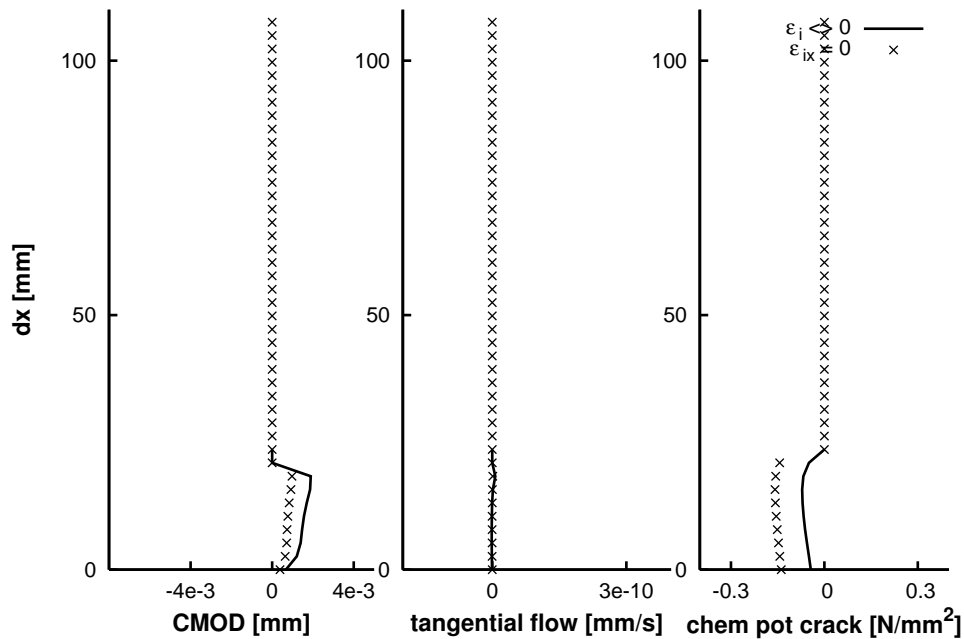


**Figure 5.19:** Evolution for the osmolarity test in plane of crack of chemical potential, tangential flow and crack mouth opening (CMOD) after 130 increments,  $\Delta\mu^f = -0.4 \text{ MPa}$ .

crack causes fluid to flow mostly from the crack itself, because the permeability is far higher in the crack than in the medium. This flow from the crack to the crack-tip causes closing of the crack and, hence, slows down crack propagation. The expression of this phenomenon depends on loading protocol and on (direction) of prestress.

Considering the example without external mechanical load, opening and growth of the crack takes place due to a global decrease in osmotic pressure. This phenomenon is similar to the drying of clay, but in fully saturated conditions. This mechanism could be an explanation for the poor relation between intervertebral disc herniation and load. Furthermore this could be a mechanism for borehole instability.

In this chapter, bilinear shape functions, with chemical potential and displacements at the corner nodes are used to calculate the solution as a simplification. Réthoré et al. [83] show that these approximations are sufficient for structural response in non-propagating cracks when the mesh is fine enough and do not produce issues related to the Babuska-Brezzi conditions [114]. This condition requires a higher order interpolation of the displacement field than of the pressure field.

The introduction of the distance function increases the order of interpolation locally. This is needed for the higher order terms in the cavity model [83]. In this chapter partial integration is used locally, therefore the order of integration needed is less than used. This does not seem to produce any stability problems related to the Babuska-Brezzi condition, probably due to the local use.

Further comparison between this approach and literature is difficult since either

partially saturated conditions are considered [4,85]. Furthermore, results, such as mesh-dependency, is most prominent in lower stiffness cases.

The results are addressed in more detail.

Generally, upon loading the effective stresses at the crack-tip increases and the chemical potential decreases. This is reached by a fluid flow away from the crack-tip. Upon crack propagation the effective stress at the tip suddenly decreases and the chemical potential increases by a fluid flow towards the crack-tip. The time needed to resolve the flow over the extension is equivalent to the stiffness times permeability ( $\Delta t \sim \Delta x^2 / cK$ ).

In case of the delamination test, the material is the stiffness and permeability are so high that fluid (nor chemical potential nor tangential flow) seems to hardly influence crack growth. The presence of prestress seems therefore to enhance crack propagation (Fig. 5.11). The contact with a reservoir changes the flow pattern at the crack, but influence on crack propagation is low.

When the material is less stiff, the influence of the fluid becomes more profound. The pull test decreases the chemical potential in the crack to such an extent, that the osmotic pressure in the crack is lower than in the material. The low osmotic pressure in the crack causes flow from the material into the crack and with that further opening of the crack. The time to initiation is longer in case of no prestress than with prestress due to the slower opening of the crack (Fig. 5.16). In the case without initial prestress in  $y$ -direction, the crack closes temporary due to the osmotic pressure in the material which is larger than the pressure in the crack.

Upon crack growth a steep change in chemical potential takes place. Due to the lower stiffness and permeability of the material than the previous case, the time needed to resolve the flow is bigger. Furthermore, the stress at the crack-tip is not relieved as it should be, which causes fast crack growth. Finally, the mismatch between the physical flow and the simulated flow via the weak discontinuity causes loss of numerical stability. A solution cannot be found anymore.

In the last case a material of relatively low stiffness is considered. The material is not loaded mechanically at the external boundary of the material, but crack initiation is dominated by internal loading. By changing the external salt concentration at the outside of the material, the osmotic pressure is lower outside than inside the material. This difference in osmotic pressure initiates flow. The material shrinks where it is possible, namely at the crack. The result is opening of the crack. The opening of the crack is largest in case minimal prestress in  $y$ -direction (Fig. 5.19), since the pressure difference between the material and the crack is larger. The intervertebral disc is highly prestressed, which gives protection against crack propagation in case of small osmotic changes.

In case of only prestress in  $y$ -direction (and with that the largest), damage evolution is delayed and slower. Therefore the numerical calculations are relatively stable. In all cases stability of the calculations is lost upon the forming of the macro crack, most probably because the fluid flow is unresolved. Nevertheless, just after damage propagation a local change in flow is seen (Fig. 5.18). Flow is attracted from inside the crack near the crack-tip, rather than from the surrounding medium.

## CHAPTER SIX

# Discussion and conclusions

## Discussion and conclusions

A mesh-independent 2D finite element model of crack propagation in osmotic swelling porous media has been developed. The model has the capability of describing both mode-II and mode-I crack propagation. The numerical results have been compared to a specially designed analytical solution of a dislocation of a non-propagating crack in swelling porous media. The model has been applied to mode-II failure under confined compression, to a delamination test and to a mode-I test for crack propagation under changing salt concentration.

In particular, crack propagation without external mechanical load has been simulated by applying an external change in salt concentration. This last result is qualitatively consistent with an experiment on a hydrogel (Fig. 1.4). The mechanism exemplified by the simulation is hypothesized to explain borehole instability in deviated boreholes in swelling shales [33,87], as well as the poor relation between disc degeneration and external mechanical load observed in human disc studies [11,100].

In this thesis discontinuities are included in the mathematics of the finite element method (FEM) by the partition of unity approach [9,80] making remeshing superfluous. The effect of the discontinuity on the displacement field and fluid flow is added to the bulk behavior by the introduction of discontinuous field variables, projection of the crack onto an element (dividing it in two parts), increasing the amount of degrees of freedom of the corresponding nodes with these discontinuous variables and integration of the two parts of the element separately.

Damage preceding propagation, such as micro-cracking, is introduced by cohesive zone modeling. The cohesive zone model relates traction forces to the opening of a crack on a fictitious extension ahead of the crack, effectively smearing the stress singularity. The treatment of displacement discontinuities (the solid phase) is directly adopted from solid mechanics, but the treatment of the fluid phase is not straight forward. Therefore different loadings are addressed separately. Both approaches are suitable for porous media based on Theory of Porous Media [32].

Firstly, shear loading is addressed. In shear loading the crack is closed and no additional assumptions about the fluid flow in the crack are required. In this thesis a singularity solution for shear loading is developed to verify the numerical accuracy of the model, namely a two-edge dislocation. Loading a crack impulsively results in consolidation, i.e. transfer of load between the fluid and solid phase. Comparison of the analytical solution with a commercial code, where the crack was geometrically defined, shows that shear stress is underestimated near the crack-tips causing an offset throughout time.

The numerical representation of the crack is improved by including the displacement discontinuity in the FEM with partition of unity. The presence of a discontinuity in the solid phase affects the fluid phase. When a crack is loaded under shear, a pressure difference holds between the two sides of the discontinuity with a small transition zone, which fades in time. A small mesh size would be required to capture this phenomenon. Mesh refinement is circumvented by introducing a jump (strong discontinuity) in the fluid field (chemical potential). The resulting flow is unresolved in the element. The

flow on the unresolved scale is related to the resolved scale by the introduction of the unresolved hydraulic permeability. The method seems robust for different choices of material stiffness and permeability. In case of the two-edge dislocation, the shear stress distribution shows oscillations which decreases with mesh-refinement. Comparison of the results of a two-edge dislocation with the new model to the analytical solution shows that the model was capable of capturing the singularity behavior quite well. The use of partition of unity for displacement discontinuity, captures the shear stress singularity for the finest mesh (still a relatively coarse mesh) well. Similar mesh-independent behavior is found to other papers [7,82], though in this case fluid exchange between the crack surfaces is allowed.

A confined compression test under shear loading shows that the flow in the damaged zone does influence total flow and fracture behavior as found in other papers [7,82]. Furthermore, the osmotic prestress does influence the path and rate of crack growth, also found by Radi and Loret for prestress in solids [77]. Lastly, crack propagation alternates with pressure diffusion across the crack resulting in a stepwise propagation of the fracture. To our knowledge this stepwise propagation is not reported in literature so far.

Secondly, tensile loading is considered. In tensile loading a steep potential gradient at both crack surfaces is expected (symmetric). The steep gradient is approximated by the introduction of a weak discontinuity using a distance function [83], while the displacement jump is approximated by a strong discontinuity. The fluid flow at the crack is dominated by deformation, fluid exchange between the crack and the surrounding material, and flow in the crack. Couette flow is assumed to model the flow inside the crack. Benchmarks are hardly available; therefore two tests of external mechanical loading are considered (a delamination test and a pull test). In addition, one test without external mechanical load is considered, namely loading of the crack by changing the osmotic pressure (a osmolarity test).

The tests show that tensile loading of the crack results in a low chemical potential of the fluid in the crack. Depending on the stiffness, prestress and permeability of the material the low chemical potential is compensated by the fluid in the crack or by fluid from the surrounding medium. When fluid is extracted from the crack, the crack closes, slowing down crack propagation. This loading and unloading is also seen in fluid-driven fracture propagation [17]. The loading and unloading of the crack require a history dependent damage evolution. In a addition a contact algorithm in the crack is required. Due to the simplicity of the contact algorithm, numerical stability is decreased.

Furthermore, with the decrease of stiffness or permeability, the time for the fluid flow to resolve after growth of one element increases ( $\Delta t \sim \Delta x^2 / cK$ ). The element size is too large to resolve the fluid flow or the rate of propagation too large. The mismatch between numerical flow and physical flow causes numerical instability and slight mesh-dependency of the fluid phase. This is not seen in the case of delamination where material properties are in the same range as Réthoré et al. [83] and Roels et al. [85]. It is unclear whether they would suffer the same mesh-dependence for different parameters. An extension or variant of the approach is needed to overcome mesh-dependency for low stiffness cases.



## Limitations and recommendations

### Numerical simulations

The link between deformation and fluid flow is strong. Therefore improvement of the underlying element properties, i.e. displacement and chemical potential in the nodes with linear approximations, is essential for correct approximation of the fluid flow. A mixed-hybrid approach has shown to be able to deal very well with large gradients in undamaged materials [66]. This approach is likely to enhance numerical stability. In addition, the Newton-Raphson procedure can be improved by separating the convergence criterion for fluid field and solid field.

The bulk porous matrix is assumed linear elastic and homogeneous. Furthermore, ion flow is neglected. Permeability and volume fractions are chosen independently of deformation, while in reality they are not. These simplifications are made, because this work has been a first step. An extension to nonlinear, anisotropic materials and finite deformations should be made [31,109].

Inertia forces are neglected. In soft tissue this assumption is probably valid, but for geotechnical applications it is not. The introduction of inertia forces might produce acoustical waves and increase singularity of the fluid phase [62]. Furthermore in practise, materials are 3D and can have different properties in different directions. A step to 3-D should be made for application.

The previous recommendations involve the bulk material. There is also room for improvement of the discontinuity kinematics. The partition of unity method seems to be applicable and useful in ionized porous media. Especially in shear loading, simulations seem robust. To increase numerical stability in case of tensile loading, a symmetric strong discontinuity or an increase in the order of the enhancement function might be an option. Adding information to FEM might result in less numerical stability [72], therefore a strong discontinuity is preferred.

The cohesive zone models applied here were simple and not validated. The influence of the choice of cohesive zone model could be examined. Furthermore, phenomena like time-dependent behavior and friction between the crack surfaces could be added to the cohesive zone.

The nucleation of damage was based on maximum (principal) effective stress using stress averaging (nonlocal approach). The yield criterion could be improved to a Drucker-Prager yield condition [77] or using a multi-scale approach at the crack-tip.

Material transitions also can be approximated by partition of unity, i.e. separating effects of material transition and not discontinuity. This allows for material transitions within an element and debonding between different materials within an element and debonding within composites [5,38].

Verification of the weak discontinuity model has not been performed. It would be interesting to consider hydraulic fracturing in non-ionized porous media and compare the

results to literature data.

Last but not least, most natural cracks are not purely mode-I or mode-II in nature. Therefore a step to arbitrary cracking has to be made. This is possible if the fluid phase is not enhanced by only one enhancement function, but by two: one related to the pressure difference between crack surfaces due to the shear component, and the other to the flow in the crack.

## Experimental simulations

Validation of the model has not been addressed for both models. There are not many experiments available in literature and if they are, osmotic conditions are not taken into account or administrated well. There is a great need for experiments for failure patterns and associated flow. Length scales and size effects are hardly known.

Hydrogel is very suitable to do validation on small scale. The properties of the hydrogel can be altered easily, such that a wide range a parameters can be tested. Experiments have been performed with isotropic hydrogel to show that existing cracks open under decreasing osmotic pressure. It would be interesting to visualize the corresponding flow. Furthermore it would be interesting to visualize deformations in case of reinforced hydrogel or tissue. An example for a setup is given in Fig. 6.1.

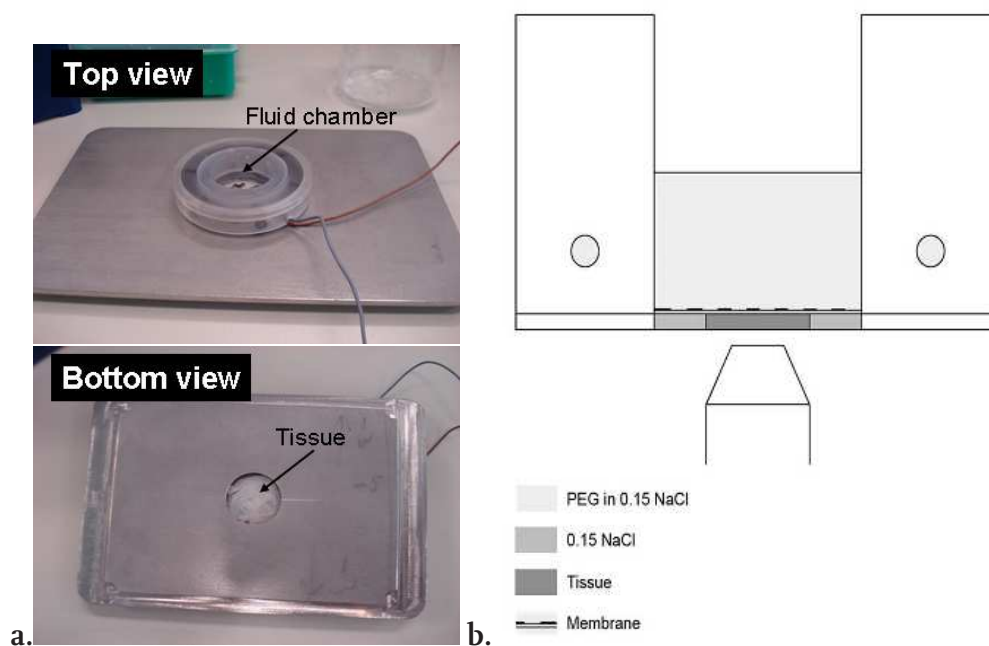


**Figure 6.1:** Setup for visualization. **a.** top and bottom view with tissue clammed in the column. **b.** Sample is hydrated in external salt solution. The sample is prestressed by adding polyethylene glycol (PEG, causes osmotic loading of the sample) to the column separated by a membrane from the sample.



## Bibliography

- [1] M Abramowitz and I A Stegun. *Handbook of mathematical functions*. New York: Dover, 1970.
- [2] M. A. Adams, P. Dolan, and W. C. Hutton. Diurnal variations in the stresses on the lumbar spine. *Spine*, 12(2):130–137, 1987.
- [3] M. A. Adams and P. J. Roughley. What is intervertebral disc degeneration, and what causes it? *Spine*, 31(18):2151–2161, 2006.
- [4] R. Al-Khoury and L. J. Sluys. A computational model for fracturing porous media. *International Journal for Numerical Methods in Engineering*, 70(4):423–444, 2007.
- [5] M.V. Cid Alfaro, A.S.J. Suiker, R. de Borst, and J.J.C. Remmers. Analysis of fracture and delamination in laminates using 3d numerical modelling. *Engng. Fracture Mech.*, 76:761–780, 2009.
- [6] J. Antoniou, T. Steffen, F. Nelson, N. Winterbottom, A. P. Hollander, R. A. Poole, M. Aebi, and M. Alini. The human lumbar intervertebral disc: evidence for changes in the biosynthesis and denaturation of the extracellular matrix with growth, maturation, ageing, and degeneration. *J. Clin. Invest*, 98(4):996–1003, 1996.
- [7] F. Armero and C. Callari. An analysis of strong discontinuities in a saturated poro-plastic solid. *International Journal for Numerical Methods in Engineering*, 46(10):1673–1698, 1999.
- [8] C. Atkinson and R. V. Craster. Plane-strain fracture in poroelastic media. *Proceedings of the Royal Society of London Series A-Mathematical Physical and Engineering Sciences*, 434(1892):605–633, 1991.
- [9] I. Babuska and J. M. Melenk. The partition of unity method. *International Journal for Numerical Methods in Engineering*, 40(4):727–758, 1997.
- [10] G. I. Barenblatt. The mathematical theory of equilibrium cracks in brittle fracture. *Advances in Applied Mechanics*, (7):55–129, 1962.
- [11] M. C. Battie, T. Videman, and E. Parent. Lumbar disc degeneration: epidemiology and genetic influences. *Spine*, 29(23):2679–2690, 2004.
- [12] T. Belytschko and T. Black. Elastic crack growth in finite elements with minimal remeshing. *International Journal for Numerical Methods in Engineering*, 45(5):601–620, 1999.

- [13] M A Biot. General theory of three-dimensional consolidation. *J Appl Phys*, 12(2):155–164, 1941.
- [14] M A Biot. General solutions of the equations of elasticity and consolidation for a porous material. *J Appl Mech*, pages 91–96, 1956.
- [15] J. R. Booker. Time-dependent strain following faulting of a porous-medium. *Journal of Geophysical Research*, 79(14):2037–2044, 1974.
- [16] T. J. Boone and A. R. Ingraffea. A numerical procedure for simulation of hydraulically-driven fracture propagation in poroelastic media. *International Journal for Numerical and Analytical Methods in Geomechanics*, 14(1):27–47, 1990.
- [17] T. J. Boone, A. R. Ingraffea, and J. C. Roegiers. Simulation of hydraulic fracture propagation in poroelastic rock with application to stress measurement techniques. *International Journal of Rock Mechanics and Mining Sciences & Geomechanics Abstracts*, 28(1):1–14, 1991.
- [18] J. A. Buckwalter. Spine update - aging and degeneration of the human intervertebral disc. *Spine*, 20(11):1307–1314, 1995.
- [19] J. P. Callaghan and S. M. McGill. Intervertebral disc herniation: studies on a porcine model exposed to highly repetitive flexion/extension motion with compressive force. *Clin. Biomech. (Bristol. , Avon. )*, 16(1):28–37, 2001.
- [20] G. T. Camacho and M. Ortiz. Computational modelling of impact damage in brittle materials. *International Journal of Solids and Structures*, 33(20-22):2899–2938, 1996.
- [21] O. Coussy, L. Dormieux, and E. Detournay. From mixture theory to biot’s approach for porous media. *International Journal of Solids and Structures*, 35(34-35):4619–4635, 1998.
- [22] R. de Borst. Challenges in computational materials science: Multiple scales, multiphysics and evolving discontinuities. *Computational Materials Science*, 43(1):1–15, 2008.
- [23] R. de Borst, J. J. C. Remmers, A. Needleman, and M. A. Abellan. Discrete vs smeared crack models for concrete fracture: bridging the gap. *International Journal for Numerical and Analytical Methods in Geomechanics*, 28(7-8):583–607, 2004.
- [24] R. de Borst, J. Rethore, and M. A. Abellan. A numerical approach for arbitrary cracks in a fluid-saturated medium. *Archive of Applied Mechanics*, 75(10-12):595–606, 2006.
- [25] E. Detournay and A. H. D. Cheng. Plane-strain analysis of a stationary hydraulic fracture in a poroelastic medium. *International Journal of Solids and Structures*, 27(13):1645–1662, 1991.

- [26] E Detournay and A H D Cheng. *Comprehensive rock engineering: Principles, practice and projects*, volume II. Pergamon, 1993.
- [27] E. Detournay and D. I. Garagash. The near-tip region of a fluid-driven fracture propagating in a permeable elastic solid. *Journal of Fluid Mechanics*, 494:1–32, 2003.
- [28] L. Dormieux, D. Kondo, and F. J. Ulm. A micromechanical analysis of damage propagation in fluid-saturated cracked media. *Comptes Rendus Mecanique*, 334(7):440–446, 2006.
- [29] L. Dormieux, E. Lemarchand, and O. Coussy. Macroscopic and micromechanical approaches to the modelling of the osmotic swelling in clays. *Transport in Porous Media*, 50(1-2):75–91, 2003.
- [30] D. S. Dugdale. Yielding of steel sheets containing slits. *Journal of the Mechanics and Physics of Solids*, 8(2):100–104, 1960.
- [31] W. Ehlers, N. Karajan, and B. Markert. A porous media model describing the inhomogeneous behaviour of the human intervertebral disc. *Materialwissenschaft und Werkstofftechnik*, 37(6):546–551, 2006.
- [32] W. Ehlers and B. Markert. A linear viscoelastic biphasic model for soft tissues based on the theory of porous media. *Journal of Biomechanical Engineering-Transactions of the Asme*, 123(5):418–424, 2001.
- [33] S. Ekbote, Y. Abousleiman, L. Cui, and M. Zaman. Analyses of inclined boreholes in poroelastic media. *International Journal of Geomechanics*, 4(3):178–190, 2004.
- [34] S. H. Emerman, D. L. Turcotte, and D. A. Spence. Transport of magma and hydrothermal solutions by laminar and turbulent fluid fracture. *Physics of the Earth and Planetary Interiors*, 41(4):249–259, 1986.
- [35] A. J. H. Frijns, J. M. Huyghe, and J. D. Janssen. A validation of the quadriphasic mixture theory for intervertebral disc tissue. *International Journal of Engineering Science*, 35(15):1419–1429, 1997.
- [36] T. C. Gasser and G. A. Holzapfel. Finite element modeling of balloon angioplasty by considering overstretch of remnant non-diseased tissues in lesions. *Computational Mechanics*, 40(1):47–60, 2007.
- [37] T. C. Gasser and G. A. Holzapfel. Modeling plaque fissuring and dissection during balloon angioplasty intervention. *Annals of Biomedical Engineering*, 35(5):711–723, 2007.
- [38] T. Hettich, A. Hund, and E. Ramm. Modeling of failure in composites by x-fem and level sets within a multiscale framework. *Computer Methods in Applied Mechanics and Engineering*, 197(5):414–424, 2008.

- [39] T. Hettich and E. Ramm. Interface material failure modeled by the extended finite-element method and level sets. *Computer Methods in Applied Mechanics and Engineering*, 195(37-40):4753–4767, 2006.
- [40] A. Hillerborg, M. Modeér, and P. E. Petersson. Analysis of crack formation and crack growth in concrete by means of fracture mechanics and finite elements. *Cement and Concrete Research*, (6):773–782, 1976.
- [41] N. C. Huang and S. G. Russell. Hydraulic fracturing of a saturated porous-medium .I. general-theory. *Theoretical and Applied Fracture Mechanics*, 4(3):201–213, 1985.
- [42] W. C. Hutton, T. M. Ganey, W. A. Elmer, E. Kozłowska, J. L. Ugbo, E. S. Doh, and Jr. T. E. Whitesides. Does long-term compressive loading on the intervertebral disc cause degeneration? *Spine*, 25(23):2993–3004, 2000.
- [43] J. M. Huyghe and S. C. Cowin. Preface on physicochemical and electromechanical interactions in porous media. *Transport in Porous Media*, 50(1-2):1–3, 2003.
- [44] J. M. Huyghe and J. D. Janssen. Quadriphasic mechanics of swelling incompressible porous media. *International Journal of Engineering Science*, 35(8):793–802, 1997.
- [45] J. M. Huyghe and J. D. Janssen. Thermo-chemo-electro-mechanical formulation of saturated charged porous solids. *Transport in Porous Media*, 34(1-3):129–141, 1999.
- [46] J. C. Iatridis, J. P. Laible, and M. H. Krag. Influence of fixed charge density magnitude and distribution on the intervertebral disc: applications of a poroelastic and chemical electric (peace) model. *J. Biomech. Eng*, 125(1):12–24, 2003.
- [47] J. C. Iatridis, L. A. Setton, R. J. Foster, B. A. Rawlins, M. Weidenbaum, and V. C. Mow. Degeneration affects the anisotropic and nonlinear behaviors of human annulus fibrosus in compression. *J. Biomech.*, 31(6):535–544, 1998.
- [48] A.C. Jones and R.K. Wilcox. Finite element analysis of the spine: towards a framework of verification, validation and sensitivity analysis. *Medical Engineering & Physics*, 30:1287–1304, 2008.
- [49] M. Kfoury, R. Ababou, B. Noetinger, and M. Quintard. Upscaling fractured heterogeneous media: Permeability and mass exchange coefficient. *Journal of Applied Mechanics-Transactions of the Asme*, 73(1):41–46, 2006.
- [50] Y. Kim. Prediction of peripheral tears in the annulus of the intervertebral disc. *Spine*, 25(14):1771–1774, 2000.
- [51] F Kraaijeveld, J M Huyghe, and F P T Baaijens. Singularity solution of lanir’s osmoelasticity: verification of discontinuity simulations in soft tissues. *J Biomech Engng*, 2009.

- [52] F Kraaijeveld, J M Huyghe, J J C Remmers, R de Borst, and F P T Baaijens. A mesh-independent model for mode-*i* fracture in osmoelastic saturated porous media. *International Journal for Numerical Methods in Engineering*, -.
- [53] F Kraaijeveld, J M Huyghe, J J C Remmers, R de Borst, and F P T Baaijens. Shear fracture in osmoelastic saturated porous media: a mesh-independent model. *Engng Frac Mech*, 2009.
- [54] W. M. Lai, J. S. Hou, and V. C. Mow. A triphasic theory for the swelling and deformation behaviors of articular-cartilage. *Journal of Biomechanical Engineering-Transactions of the Asme*, 113(3):245–258, 1991.
- [55] W. M. Lai, V. C. Mow, D. D. Sun, and G. A. Ateshian. On the electric potentials inside a charged soft hydrated biological tissue: Streaming potential versus diffusion potential. *Journal of Biomechanical Engineering-Transactions of the Asme*, 122(4):336–346, 2000.
- [56] Y. Lanir. Biorheology and fluid flux in swelling tissues .1. bicomponent theory for small deformations, including concentration effects. *Biorheology*, 24(2):173–187, 1987.
- [57] Y. Lanir. Biorheology and fluid flux in swelling tissues .2. analysis of unconfined compressive response of transversely isotropic cartilage disk. *Biorheology*, 24(2):189–205, 1987.
- [58] J. Larsson and R. Larsson. Localization analysis of a fluid-saturated elastoplastic porous medium using regularized discontinuities. *Mechanics of Cohesive-Frictional Materials*, 5(7):565–582, 2000.
- [59] R. Larsson, K. Runesson, and S. Sture. Embedded localization band in undrained soil based on regularized strond discontinuity. theory and *fe*-analysis. *Internationla Journal Solids & Structures*, 33(20-22):3081–3101, 1996.
- [60] J. P. Little, C. J. Adam, J. H. Evans, G. J. Pettet, and M. J. Percy. Nonlinear finite element analysis of anular lesions in the l4/5 intervertebral disc. *J. Biomech.*, 40(12):2744–2751, 2007.
- [61] J. S. Little and P. S. Khalsa. Material properties of the human lumbar facet joint capsule. *Journal of Biomechanical Engineering-Transactions of the Asme*, 127(1):15–24, 2005.
- [62] B. Loret and E. Radi. The effects of inertia on crack growth in poroelastic fluid-saturated media. *Journal of the Mechanics and Physics of Solids*, 49(5):995–1020, 2001.
- [63] Y. M. Lu, W. C. Hutton, and V. M. Gharpuray. Do bending, twisting, and diurnal fluid changes in the disc affect the propensity to prolapse? a viscoelastic finite element model. *Spine*, 21(22):2570–2579, 1996.



- [64] E. J. Macari and L. R. Hoyos. Mechanical behavior of an unsaturated soil under multi-axial stress states. *Geotechnical Testing Journal*, 24(1):14–22, 2001.
- [65] K. Malakpoor, E. F. Kaasschieter, and J. M. Huyghe. Mathematical modelling and numerical solution of swelling of cartilaginous tissues. part i: Modelling of incompressible charged porous media. *Esaim-Mathematical Modelling and Numerical Analysis-Modelisation Mathematique et Analyse Numerique*, 41(4):661–678, 2007.
- [66] K. Malakpoor, E. F. Kaasschieter, and J. M. Huyghe. Mathematical modelling and numerical solution of swelling of cartilaginous tissues. part ii: Mixed-hybrid finite element solution. *Esaim-Mathematical Modelling and Numerical Analysis-Modelisation Mathematique et Analyse Numerique*, 41(4):679–712, 2007.
- [67] A. Maroudas, E. Wachtel, G. Grushko, E. P. Katz, and P. Weinberg. The effect of osmotic and mechanical pressures on water partitioning in articular cartilage. *Biochim et Biophys Acta*, 1073:285–294, 1991.
- [68] J. McNamee and R. E. Gibson. Displacements functions and linear transforms applied to diffusion through porous elastic media. *Quart J Mech and Appl Math*, 13(1):98–111, 1960.
- [69] J. Van Meerveld, M. M. Molenaar, J. M. Huyghe, and F. P. T. Baaijens. Analytical solution of compression, free swelling and electrical loading of saturated charged porous media. *Transport in Porous Media*, 50(1-2):111–126, 2003.
- [70] N. Moes and T. Belytschko. Extended finite element method for cohesive crack growth. *Engineering Fracture Mechanics*, 69(7):813–833, 2002.
- [71] V. Mow and X. E. Guo. Mechano-electrochemical properties of articular cartilage: Their inhomogeneities and anisotropies. *Annual Review of Biomedical Engineering*, 4:175–209, 2002.
- [72] E. A. Munts, S. J. Hulshoff, and R. de Borst. The partition-of-unity method for linear diffusion and convection problems: accuracy, stabilization and multiscale interpretation. *International Journal for Numerical Methods in Fluids*, 43(2):199–213, 2003.
- [73] R. N. Natarajan, J. R. Williams, and G. B. Andersson. Recent advances in analytical modeling of lumbar disc degeneration. *Spine*, 29(23):2733–2741, 2004.
- [74] R. N. Natarajan, J. R. Williams, S. A. Lavender, and G. B. J. Andersson. Poro-elastic finite element model to predict the failure progression in a lumbar disc due to cyclic loading. *Computers & Structures*, 85(11-14):1142–1151, 2007.
- [75] A. Needleman. A continuum model for void nucleation by inclusion debonding. *Journal of Applied Mechanics*, 54:525–531, 1987.
- [76] A. Nur and J. R. Booker. Aftershocks caused by pore fluid-flow. *Science*, 175(4024):885–887, 1972.

- [77] E. Radi, D. Bigoni, and B. Loret. Effects of pre-stress on crack-tip fields in elastic, incompressible solids. *International Journal of Solids and Structures*, 39:3971–3996, 2002.
- [78] J. J. C. Remmers. *Discontinuities in materials and structures. A unifying computational approach*. PhD thesis, University of Technology Delft, The Netherlands, 2006.
- [79] J. J. C. Remmers and R. de Borst. Delamination buckling of fibre-metal laminates. *Composites Science and Technology*, 61(15):2207–2213, 2001.
- [80] J. J. C. Remmers, R. de Borst, and A. Needleman. A cohesive segments method for the simulation of crack growth. *Computational Mechanics*, 31(1-2):69–77, 2003.
- [81] J. J. C. Remmers, R. de Borst, and A. Needleman. The simulation of dynamic crack propagation using the cohesive segments method. *Journal of the Mechanics and Physics of Solids*, 56(1):70–92, 2008.
- [82] J. Rethore, R. de Borst, and M. A. Abellan. A discrete model for the dynamic propagation of shear bands in a fluid-saturated medium. *International Journal for Numerical and Analytical Methods in Geomechanics*, 31(2):347–370, 2007.
- [83] J. Rethore, R. de Borst, and M. A. Abellan. A two-scale approach for fluid flow in fractured porous media. *International Journal for Numerical Methods in Engineering*, 71(7):780–800, 2007.
- [84] J R Rice and M P Cleary. Some basic stress diffusion solutions for fluid-saturated elastic porous media with compressible constituents. *Rev. Geophys. and Space Phys.*, 14(2):227–241, 1976.
- [85] S. Roels, P. Moonen, K. De Proft, and J. Carmeliet. A coupled discrete-continuum approach to simulate moisture effects on damage processes in porous materials. *Computer Methods in Applied Mechanics and Engineering*, 195(52):7139–7153, 2006.
- [86] J. G. Rots. Smearred and discrete representation of localized fracture. *International Journal of Fracture*, 51:45–59, 1991.
- [87] F.J. Santarelli, D. Dahren, H. Baroudi, and K. B. Sliman. Mechanisms of borehole instability in heavily fractured rock media. *Int. J. Rock Mech. Min. Sci. & Geomech. Abstr.*, 29(5):457–467, 1992.
- [88] J. C. J. Schelleken and R. de Borst. Free edge delamination in carbon-epoxy laminates: a novel numerical/experimental approach. *Composite Structures*, 28:357–373, 1994.
- [89] B. A. Schrefler, S. Secchi, and L. Simoni. On adaptive refinement techniques in multi-field problems including cohesive fracture. *Computer Methods in Applied Mechanics and Engineering*, 195(4-6):444–461, 2006.

- [90] B. A. Schrefler, S. Secchio, and L. Simoni. Numerical procedure for discrete fracture propagation in porous materials. pages 220–229, 2004.
- [91] Y. Schroeder, S. Sivan, W. Wilson, Y. Merkher, J. M. Huyghe, A. Maroudas, and F. P. Baaijens. Are disc pressure, stress, and osmolarity affected by intra- and extrafibrillar fluid exchange? *J. Orthop. Res.*, 25(10):1317–1324, 2007.
- [92] Y. Schroeder, W. Wilson, J. M. Huyghe, and F. P. Baaijens. Osmoviscoelastic finite element model of the intervertebral disc. *Eur. Spine J.*, 15 Suppl 3:S361–S371, 2006.
- [93] S. Secchi, L. Simoni, and B. A. Schrefler. Mesh adaptation and transfer schemes for discrete fracture propagation in porous materials. *International Journal for Numerical and Analytical Methods in Geomechanics*, 31(2):331–345, 2007.
- [94] L. Simoni and S. Secchi. Cohesive fracture mechanics for a multi-phase porous medium. *Engineering Computations*, 20(5-6):675–698, 2003.
- [95] D. I. Simunic, N. D. Broom, and P. A. Robertson. Biomechanical factors influencing nuclear disruption of the intervertebral disc. *Spine*, 26(11):1223–1230, 2001.
- [96] D. I. Simunic, P. A. Robertson, and N. D. Broom. Mechanically induced disruption of the healthy bovine intervertebral disc. *Spine*, 29(9):972–978, 2004.
- [97] P. Steinmann. A finite element formulation for strong discontinuities in fluid-saturated porous media. *Mechanics of Cohesive-Frictional Materials*, 4(2):133–152, 1999.
- [98] K Terzaghi. *Theoretical soil mechanics*. John Wiley and Sons, New York, 1943.
- [99] J. P. Urban and A. Maroudas. Swelling of the intervertebral disc in vitro.
- [100] J. P. Urban and S. Roberts. Degeneration of the intervertebral disc. *Arthritis Res. Ther.*, 5(3):120–130, 2003.
- [101] M. J. van den Bosch, P. J. G. Schreurs, and M. G. D. Geers. An improved description of the exponential xu and needleman cohesive zone law for mixed-mode decohesion. *Engineering Fracture Mechanics*, 73(9):1220–1234, 2006.
- [102] R. van Loon, J. M. Huyghe, M. W. Wijlaars, and F. P. T. Baaijens. 3d fe implementation of an incompressible quadriphasic mixture model. *International Journal for Numerical Methods in Engineering*, 57(9):1243–1258, 2003.
- [103] P. A. Vermeer and A. Verruijt. An accuracy condition for consolidation by finite-elements. *International Journal for Numerical and Analytical Methods in Geomechanics*, 5(1):1–14, 1981.
- [104] A. Verruijt. Displacement functions in theory consolidation or in thermoelasticity. *Zeitschrift für Angewandte Mathematik und Physik*, 22(5):891–898, 1971.

- [105] T. Videman and M. C. Battie. The influence of occupation on lumbar degeneration. *Spine*, 24(11):1164–1168, 1999.
- [106] G. N. Wells. *Discontinuous modelling of strain localisation and failure*. PhD thesis, University of Technology Delft, The Netherlands, 2001.
- [107] G. N. Wells and L. J. Sluys. Discontinuous analysis of softening solids under impact loading. *International Journal for Numerical and Analytical Methods in Geomechanics*, 25(7):691–709, 2001.
- [108] W. Wilson, C. C. van Donkelaar, and J. M. Huyghe. A comparison between mechano-electrochemical and biphasic swelling theories for soft hydrated tissues. *Journal of Biomechanical Engineering-Transactions of the Asme*, 127(1):158–165, 2005.
- [109] W. Wilson, C. C. van Donkelaar, B. van Rietbergen, and R. Huiskes. A fibril-reinforced poroviscoelastic swelling model for articular cartilage. *Journal of Biomechanics*, 38(6):1195–1204, 2005.
- [110] W. Wilson, C. C. van Donkelaar, B. van Rietbergen, K. Ito, and R. Huiskes. Stresses in the local collagen network of articular cartilage: a poroviscoelastic fibril-reinforced finite element study. *Journal of Biomechanics*, 37(3):357–366, 2004.
- [111] S. Wognum, J. M. Huyghe, and F. P. T. Baaijens. Influence of osmotic pressure changes on the opening of existing cracks in 2 intervertebral disc models. *Spine*, 31(16):1783–1788, 2006.
- [112] X. P. Xu and A. Needleman. Void nucleation by inclusion debonding in a crystal matrix. *Modelling and Simulation in Materials Science and Engineering*, 1(2):111–132, 1993.
- [113] C. Y. Yu, K. H. Tsai, W. P. Hu, R. M. Lin, H. W. Song, and G. L. Chang. Geometric and morphological changes of the intervertebral disc under fatigue testing. *Clin. Biomech. (Bristol. , Avon. )*, 18(6):S3–S9, 2003.
- [114] O. C. Zienkiewicz, S. Qu, R. L. Taylor, and S. Nakazawa. The patch test for mixed formulations. *International Journal for Numerical Methods in Engineering*, 23(10):1873–1883, 1986.



## APPENDIX A

# Derivations for analytical solution

### A.1 Derivation of stress functions

The system is given by (A.1) and corresponds with (3.6).

$$\begin{aligned} \mu \nabla^2 u + (\lambda + \mu + RT\Gamma C_1) \frac{\partial}{\partial x} e - \frac{\partial}{\partial x} \mu^f &= 0, \\ \mu \nabla^2 w + (\lambda + \mu + RT\Gamma C_1) \frac{\partial}{\partial z} e - \frac{\partial}{\partial z} \mu^f &= 0, \\ \frac{\partial e}{\partial t} - K \nabla^2 \mu^f &= 0. \end{aligned} \quad (\text{A.1})$$

#### A.1.1 Stress function $S$

Firstly, the stress function  $S$  is derived which is related to chemical potential. For this purpose, the first equation of (A.1) is differentiated to  $x$ , the second to  $z$ . The differentiated equations are then summed.

$$\nabla^2 ((2\mu + \lambda + RT\Gamma C_1)e - \mu^f - RT\Gamma C_0) = 0. \quad (\text{A.2})$$

Following McNamee and Gibson [68], the harmonic function  $S(x, z, t)$  is introduced. A function  $S$  is said to be harmonic when  $\nabla^2 S = 0$ . This function is chosen such it has opposite sign of strain and with that it has the same sign as pressure. Then for the chemical potential holds

$$\mu^f = (2\mu + \lambda + RT\Gamma C_1)e - a\mu \frac{\partial S}{\partial z} - RT\Gamma C_0. \quad (\text{A.3})$$

Equation (A.2) is automatically satisfied if  $S$  is harmonic. The value of the constant  $a$  in (A.3) is reduced in the next steps. Equations (A.1) are reduced to

$$\begin{aligned} \mu \nabla^2 u - \mu \frac{\partial}{\partial x} e + a\mu \frac{\partial^2 S}{\partial x \partial z} &= 0, \\ \mu \nabla^2 w - \mu \frac{\partial}{\partial z} e + a\mu \frac{\partial^2 S}{\partial z^2} &= 0, \\ \frac{\partial e}{\partial t} - K \nabla^2 \mu^f &= 0. \end{aligned} \quad (\text{A.4})$$

The factor  $\mu$  is removed. The separation of the displacements is introduced.

$$\begin{aligned} u &= u_1 + u_2 + u_3, \\ w &= w_1 + w_2 + w_3. \end{aligned} \quad (\text{A.5})$$

Here  $u_1, w_1$  are associated with strain  $e$ ,  $u_2, w_2$  are associated with harmonic function  $S$  and  $u_3, w_3$  are harmonic functions. If these functions satisfy

$$\begin{aligned}\nabla^2 u_1 + \frac{\partial e}{\partial x} &= 0, \\ \nabla^2 u_2 + a \frac{\partial^2 S}{\partial x \partial z} &= 0, \\ \nabla^2 u_3 &= 0\end{aligned}\tag{A.6}$$

and

$$\begin{aligned}\nabla^2 w_1 + \frac{\partial e}{\partial z} &= 0, \\ \nabla^2 w_2 + a \frac{\partial^2 S}{\partial z^2} &= 0, \\ \nabla^2 w_3 &= 0\end{aligned}\tag{A.7}$$

then the first two equations of (A.4) are satisfied. If we differentiate (A.6a) to  $x$  and (A.7a) to  $z$  the next holds

$$\nabla^2 e = \nabla^2 \left( \frac{\partial u_1}{\partial x} + \frac{\partial w_1}{\partial z} \right),\tag{A.8}$$

The factor  $a$  is chosen  $a = 2$ . This prevents fractions in the solution.

### A.1.2 Stress function $E$

The solutions of equations (A.6), (A.7) and (A.8) are given by (A.10). From these solutions the stress function  $E$  is derived. The first equation of (A.10) is chosen intuitively, with  $X$  an arbitrary differentiable function. The remaining equations are found through solving the PDE's. For instance the solutions  $u_2$  and  $w_2$ , related to harmonic function  $S$ , both follow the general solution (constant solution not taken into account)

$$\begin{aligned}u_2 &= a_1 S + a_2 z S + a_3 \frac{\partial S}{\partial x} + a_4 \frac{\partial S}{\partial z} + a_5 z \frac{\partial S}{\partial x} + a_6 z \frac{\partial S}{\partial z} + h.o.t. \\ w_2 &= b_1 S + b_2 z S + b_3 \frac{\partial S}{\partial x} + b_4 \frac{\partial S}{\partial z} + b_5 z \frac{\partial S}{\partial x} + b_6 z \frac{\partial S}{\partial z} + h.o.t.\end{aligned}\tag{A.9}$$

These terms are the result of the fact that  $\nabla^2 S = 0$  holds. They are present in the general solutions for  $u_1, u_3, w_1$  and  $w_3$  as well. Furthermore  $a_4 = -c_2/2$  has to hold for  $u_2$  and  $b_6 = -a/2$  for  $w_2$  to satisfy the second equations of (A.6) and (A.7). That is why  $a = 2$  was chosen. Equations (A.8) require  $a_1 = -b_1, a_4 = -b_3, a_3 = 0, b_4 = a/2$ . The solutions are

$$\begin{aligned}e &= \nabla^2 X, \quad \nabla^2 Y = 0, \\ u_1 &= \frac{\partial X}{\partial x}, \quad u_2 = -z \frac{\partial S}{\partial x}, \quad u_3 = + \frac{\partial Y}{\partial x}, \\ w_1 &= \frac{\partial X}{\partial z}, \quad w_2 = S - z \frac{\partial S}{\partial z}, \quad w_3 = + \frac{\partial Y}{\partial z}.\end{aligned}\tag{A.10}$$

$E$  is taken  $E = X + Y$  which means that  $e = \nabla^2 E$ .

## A.2 State variables in terms of Stress Functions

$$\begin{aligned} u &= \frac{\partial E}{\partial x} - z \frac{\partial S}{\partial x}, \\ w &= \frac{\partial E}{\partial z} - z \frac{\partial S}{\partial z} + S, \\ \mu^f &= c \nabla^2 E - 2\mu \frac{\partial S}{\partial z}, \end{aligned} \quad (\text{A.11})$$

The stresses are given by

$$\begin{aligned} \sigma_{xx} &= -2\mu \left\{ \frac{\partial^2 E}{\partial z^2} + z \frac{\partial^2 S}{\partial x^2} - \frac{\partial S}{\partial z} \right\}, \\ \sigma_{xz} &= 2\mu \left\{ \frac{\partial^2 E}{\partial x \partial z} - z \frac{\partial^2 S}{\partial x \partial z} \right\} \\ \sigma_{zz} &= -2\mu \left\{ \frac{\partial^2 E}{\partial x^2} + z \frac{\partial^2 S}{\partial z^2} - \frac{\partial S}{\partial z} \right\} \end{aligned} \quad (\text{A.12})$$

These are used to derive the boundary conditions.

## A.3 Jump Condition Mode II

Shear faulting is considered. For shear faulting the displacement jump between  $z = 0^-$  and  $z = 0^+$  is given by

$$[u] = f(x) \mathcal{H}(t). \quad (\text{A.13})$$

with  $f(x)$  the slip function, and  $\mathcal{H}(t)$  the Heaviside function. There is no jump in normal displacement and therefore  $[\hat{w}] = 0$  holds at  $z = 0$ . The slip function has Fourier transform  $\tilde{f}(k)$ .

Then taking Fourier and Laplace transformation gives at  $z = 0$ :

$$[\hat{u}] = \tilde{f}(k) / p = ik \hat{E} \rightarrow [\hat{E}] = \frac{\tilde{f}(k)}{ikp}. \quad (\text{A.14})$$

$$[\hat{w}] = 0 \rightarrow \left[ \frac{\partial \hat{E}}{\partial z} \right] = -[\hat{S}]. \quad (\text{A.15})$$

Other jump conditions at  $z = 0$  is continuity of pore pressure and its normal derivative:

$$\begin{aligned} [\hat{\mu}^f] &= 0. \rightarrow c \left[ \frac{\partial^2 \hat{E}}{\partial z^2} \right] - ck^2 [\hat{E}] - 2\mu \left[ \frac{\partial \hat{S}}{\partial z} \right] = 0. \\ \left[ \frac{\partial \hat{\mu}^f}{\partial z} \right] &= 0. \rightarrow c \left[ \frac{\partial^3 \hat{E}}{\partial z^3} \right] - ck^2 \left[ \frac{\partial \hat{E}}{\partial z} \right] - 2\mu \left[ \frac{\partial^2 \hat{S}}{\partial z^2} \right] = 0. \end{aligned} \quad (\text{A.16})$$

Furthermore continuity of stresses  $\hat{\sigma}_{xz}$  and  $\hat{\sigma}_{zz}$  is assumed.

$$[\hat{\sigma}_{xz}] = [\hat{\sigma}_{zz}] = 0. \quad (\text{A.17})$$



The following holds:

$$2\mu ik \left\{ \left[ \frac{\partial \hat{E}}{\partial z} \right] \right\} = 0. \quad - 2\mu \left\{ -k^2 [\hat{E}] - \left[ \frac{\partial \hat{S}}{\partial z} \right] \right\} = 0. \quad (\text{A.18})$$

Equations (A.14) - (A.18) form six equations with seven unknowns. They reduce to jump conditions for the stress functions and their derivatives and for the transformed equations (A.34).

The first jump condition is derived from (A.14).

$$[\hat{E}] = \frac{-i}{ks} \tilde{f}(k), \quad (\text{A.19})$$

while (A.18) gives

$$\left[ \frac{\partial \hat{E}}{\partial z} \right] = 0. \quad (\text{A.20})$$

Substituting (A.19) in (A.18) results in jump condition

$$\left[ \frac{\partial \hat{S}}{\partial z} \right] = \frac{ik}{s} \tilde{f}(k) \quad (\text{A.21})$$

Substituting (A.20) in (A.15) results in the next jump condition

$$[\hat{S}] = 0. \quad (\text{A.22})$$

Inserting the jump conditions (A.19) and (A.21) in equation (A.16) gives the jump condition for second order derivative of function  $E$

$$\left[ \frac{\partial^2 \hat{E}}{\partial z^2} \right] = -\frac{ik}{s} \tilde{f}(k) (1 - 2\mu/c). \quad (\text{A.23})$$

The last jump condition is derived by inserting the jump condition (A.20) in equation (A.16).

$$\left[ \frac{\partial^2 \hat{S}}{\partial z^2} \right] = \frac{c}{2\mu} \left[ \frac{\partial^3 \hat{E}}{\partial z^3} \right]. \quad (\text{A.24})$$

## A.4 Fourier and Laplace Transformations

Integral forms are used to handle discontinuities in space and time. Another advantage is that integration and differentiation become multiplication and division. We define the

next Fourier and Laplace transformations of the decoupling functions  $E$  and  $S$ .

$$\begin{aligned}
 \tilde{E}(k, z, t) &= \int_{-\infty}^{\infty} E(x, z, t) e^{-ikx} dx \\
 \hat{E}(k, z, s) &= \int_0^{\infty} \tilde{E}(k, z, t) e^{-st} dt \\
 \tilde{S}(k, z, t) &= \int_{-\infty}^{\infty} S(x, z, t) e^{-ikx} dx \\
 \hat{S}(k, z, s) &= \int_0^{\infty} \tilde{S}(k, z, t) e^{-st} dt
 \end{aligned} \tag{A.25}$$

### A.4.1 Fourier Transformations

A few reminders about the derivatives to  $x$

$$\begin{aligned}
 \int_{-\infty}^{\infty} \left\{ \frac{\partial E}{\partial x} \right\} e^{-ikx} dx &= \int_{-\infty}^{\infty} e^{-ikx} dE \\
 &= \lim_{a \rightarrow \infty} \left\{ E e^{-ikx} \right\}_{-a}^a - \int_{-\infty}^{\infty} -ik E e^{-ikx} dx \\
 &= 0 + ik\tilde{E}, \\
 \int_{-\infty}^{\infty} \left\{ \frac{\partial^2 E}{\partial x^2} \right\} e^{-ikx} dx &= \int_{-\infty}^{\infty} e^{-ikx} d\left(\frac{\partial E}{\partial x}\right) \\
 &= \lim_{a \rightarrow \infty} \left\{ \frac{\partial E}{\partial x} e^{ikx} e^{ikx} \right\}_{x=-a}^{x=a} - \int_{-\infty}^{\infty} -ik \frac{\partial E}{\partial x} e^{-ikx} dx \\
 &= \dots = -k^2 \tilde{E}, \\
 \int_{-\infty}^{\infty} \left\{ \nabla^2 E \right\} e^{-ikx} dx &= \left( \frac{\partial^2}{\partial z^2} - k^2 \right) \tilde{E}.
 \end{aligned} \tag{A.26}$$

Concluding, the next holds

$$\tilde{e} = \left( \frac{\partial^2}{\partial z^2} - k^2 \right) \tilde{E}. \tag{A.27}$$

Then for the displacement functions and pore pressure we find

$$\begin{aligned}
\tilde{u} &= \int_{-\infty}^{\infty} u(x, z, t) e^{-ikx} dx \\
&= \int_{-\infty}^{\infty} \left( \frac{\partial E}{\partial x} - z \frac{\partial \tilde{S}}{\partial x} \right) e^{ikx} dx \\
&= ik(\tilde{E} - z\tilde{S}). \\
\tilde{w} &= \int_{-\infty}^{\infty} w(x, z, t) e^{-ikx} dx \\
&= \int_{-\infty}^{\infty} \left( \frac{\partial E}{\partial z} - z \frac{\partial \tilde{S}}{\partial z} + S \right) e^{ikx} dx \\
&= \frac{\partial \tilde{E}}{\partial z} - z \frac{\partial \tilde{S}}{\partial z} + \tilde{S}. \\
\tilde{\mu}^f &= c \left( \frac{\partial^2}{\partial z^2} - k^2 \right) \tilde{E} - 2\mu \frac{\partial \tilde{S}}{\partial z} - RTTC_0 2\pi \delta(k).
\end{aligned} \tag{A.28}$$

The Fourier transformed stress components become

$$\begin{aligned}
\tilde{\sigma}_{xx} &= -2\mu \left\{ \frac{\partial^2 \tilde{E}}{\partial z^2} - zk^2 \tilde{S} - \frac{\partial \tilde{S}}{\partial z} \right\}. \\
\tilde{\sigma}_{xz} &= 2\mu ik \left\{ \frac{\partial \tilde{E}}{\partial z} - z \frac{\partial \tilde{S}}{\partial z} \right\}. \\
\tilde{\sigma}_{zz} &= -2\mu \left\{ -k^2 \tilde{E} + z \frac{\partial^2 \tilde{S}}{\partial z^2} - \frac{\partial \tilde{S}}{\partial z} \right\}
\end{aligned} \tag{A.29}$$

The Fourier transformed governing equations become

$$\begin{aligned}
\left( \frac{\partial^2}{\partial z^2} - k^2 \right) \tilde{S} &= 0, \\
\left( \frac{\partial^2}{\partial z^2} - k^2 \right) \frac{\partial \tilde{E}}{\partial t} - cK \left( \frac{\partial^2}{\partial z^2} - k^2 \right)^2 \tilde{E} &= 0.
\end{aligned} \tag{A.30}$$

## A.4.2 Laplace Transformations

To take out the time dependency also Laplace transformation is performed.

$$\int_0^{\infty} \frac{\partial \tilde{E}}{\partial t} e^{-st} dt = \int_0^{\infty} e^{-st} d\tilde{E} = +s\hat{E}. \tag{A.31}$$

The Laplace transformed equations for displacements (A.28), stress components (A.29) and governing equations (A.30) are (A.32) to (A.34).

$$\begin{aligned}
\hat{u} &= ik(\hat{E} - z\hat{S}), \\
\hat{w} &= \frac{\partial}{\partial z} \hat{E} - \left( z \frac{\partial}{\partial z} - 1 \right) \hat{S}, \\
\hat{\mu}^f &= c \left( \frac{\partial^2}{\partial z^2} - k^2 \right) \hat{E} - 2\mu \frac{\partial}{\partial z} \hat{S} - RTTC_0 \frac{2\pi \delta(k)}{s}.
\end{aligned} \tag{A.32}$$

$$\begin{aligned}
\hat{\sigma}_{xx} &= -2\mu \left\{ \frac{\partial^2}{\partial z^2} \hat{E} - (zk^2 + \frac{\partial}{\partial z}) \hat{S} \right\}. \\
\hat{\sigma}_{xz} &= 2\mu ik \left\{ \frac{\partial}{\partial z} \hat{E} - z \frac{\partial}{\partial z} \hat{S} \right\}. \\
\hat{\sigma}_{zz} &= -2\mu \left\{ -k^2 \hat{E} + \left( z \frac{\partial^2}{\partial z^2} - \frac{\partial}{\partial z} \right) \hat{S} \right\}
\end{aligned} \tag{A.33}$$

$$\begin{aligned} \left(\frac{\partial^2}{\partial z^2} - k^2\right)\hat{S} &= 0, \\ \left(\frac{\partial^2}{\partial z^2} - k^2\right)(cK\left(\frac{\partial^2}{\partial z^2} - k^2\right) - s)\hat{E} &= 0. \end{aligned} \quad (\text{A.34})$$

## A.5 Laplace Solution

Because the impact of the crack fades away far from the crack, the solution has to approach zero for  $z \rightarrow \pm\infty$ . The domain is divided into an upper half plane and a lower half plane, because there is a sign dependence.

### A.5.1 Solution of $\hat{S}$

Firstly, the solution of the harmonic equation (A.34a) is derived. The problem is given by

$$\begin{aligned} \left(\frac{\partial^2}{\partial z^2} - k^2\right)\hat{S} &= 0 \\ [\hat{S}] &= 0 \quad \left[\frac{\partial \hat{S}}{\partial z}\right] = \frac{ik}{s}\tilde{f}(k). \end{aligned} \quad (\text{A.35})$$

It is a Laplace equation and the general solution is given by

$$\hat{S}(k, z, s) = a_1 e^{-kz} + a_2 e^{+kz}. \quad (\text{A.36})$$

For  $z > 0$  the solution is given by  $\hat{S}_+ = a_+ e^{-|k|z}$  and for  $z < 0$  the solution is given by  $\hat{S}_- = a_- e^{+|k|z}$ . As jump conditions the jump over the displacement is given for the stress function  $S$  and its derivative.

$$\begin{aligned} \lim_{z \downarrow 0} \hat{S}_+ - \lim_{z \uparrow 0} \hat{S}_- &= a_+ - a_- = 0, \\ \lim_{z \downarrow 0} \frac{\partial \hat{S}_+}{\partial z} - \lim_{z \uparrow 0} \frac{\partial \hat{S}_-}{\partial z} &= -|k|(a_+ + a_-) = \frac{ik}{s}\tilde{f}(k). \end{aligned} \quad (\text{A.37})$$

With  $\text{sign}(k) = k/|k|$  the next holds

$$a_+ = a_- = \frac{-i\text{sign}(k)}{2s}\tilde{f}(k). \quad (\text{A.38})$$

In conclusion the solution of (A.35) is given by

$$\hat{S}(k, z, s) = \frac{-i\text{sign}(k)}{2s}\tilde{f}(k)e^{-|k||z|}. \quad (\text{A.39})$$

Note that  $\left[\frac{\partial^2 \hat{S}}{\partial z^2}\right] = k^2 a_+ - k^2 a_- = 0$ .

### A.5.2 Solution of $\hat{E}$

The mass equation is solved similarly to the harmonic stress function. The problem is

$$\begin{aligned} (\frac{\partial^2}{\partial z^2} - k^2)(cK(\frac{\partial^2}{\partial z^2} - k^2) - s)\hat{E} &= 0, \\ [\hat{E}] &= \frac{-i}{ks}\tilde{f}(k) \quad [\frac{\partial \hat{E}}{\partial z}] = 0, \\ [\frac{\partial^2 \hat{E}}{\partial z^2}] &= -\frac{ik}{cs}\tilde{f}(k)(c - 2\mu) \quad [\frac{\partial^3 \hat{E}}{\partial z^3}] = 0. \end{aligned} \quad (\text{A.40})$$

The general solution is given by (A.41) with  $\gamma = \sqrt{k^2 + \frac{s}{cK}}$  and  $\Re(\gamma) > 0$ . The solution is again divided into one for the upper half plane and one for the lower half plane.

$$\hat{E}(k, z, s) = a_+ e^{-kz} + a_- e^{+kz} + b_+ e^{-\gamma z} + b_- e^{\gamma z}. \quad (\text{A.41})$$

Again the jump conditions are used to determine these coefficients.  $a_+ = -a_-$  and  $b_+ = -b_-$  hold. Then the solution of (A.41) is given by (A.42)

$$\hat{E}(k, z, s) = a_+ \text{sign}(z) e^{-|k||z|} + b_+ \text{sign}(z) e^{-\gamma|z|}. \quad (\text{A.42})$$

with

$$\begin{aligned} a_+ &= -\left(\frac{ik\tilde{f}(k)\mu K}{s^2} + \frac{i\tilde{f}(k)}{2ks}\right), \\ b_+ &= \frac{ik\mu\tilde{f}(k)K}{s^2} \}. \end{aligned} \quad (\text{A.43})$$

Then in total the solution is given by

$$\begin{aligned} \hat{E}(k, z, s) &= -\text{sign}(z) \left\{ \frac{ik\mu\tilde{f}(k)K}{s^2} + \frac{i\tilde{f}(k)}{2ks} \right\} e^{-|k||z|} \\ &+ \text{sign}(z) \left\{ \frac{ik\mu\tilde{f}(k)K}{s^2} \right\} e^{-\frac{|z|}{\sqrt{cK}} \sqrt{k^2 cK + s}}. \end{aligned} \quad (\text{A.44})$$

We introduce the Fourier transformed function  $\tilde{g}(k)$  such that

$$\tilde{g}(k) = ik\mu\tilde{f}(k)K \quad (\text{A.45})$$

Solution rewritten becomes then

$$\begin{aligned} \hat{E}(k, z, s) &= \text{sign}(z) \left\{ \left[ -\frac{\tilde{g}(k)}{s^2} - \frac{i\tilde{f}(k)}{2ks} \right] e^{-|k||z|} \right. \\ &\left. + \frac{\tilde{g}(k)}{s^2} e^{-\frac{|z|}{\sqrt{cK}} \sqrt{k^2 cK + s}} \right\}. \end{aligned} \quad (\text{A.46})$$

## A.6 Inverse Laplace

The inverse Laplace transformations are found by Abramowitz and Stegun [1].

### A.6.1 Inverse stress function $\hat{S}$

When the solution of transformed equations are considered several terms dependent on time are present. For the stress function  $\hat{S}$  the inverse Laplace is rather simple to derive.  $\hat{S}$  contains a factor  $1/s$ . The inverse Laplace is given by

$$\mathcal{L}^{-1}\left(\frac{1}{s}\right) = \mathcal{H}(t). \quad (\text{A.47})$$

The inverse Laplace of (A.39) for the stress function  $\hat{S}$  is

$$\tilde{S}(k, z, t) = -\frac{i \operatorname{sign}(k)}{2} \tilde{f}(k) e^{-|k||z|} \mathcal{H}(t). \quad (\text{A.48})$$

### A.6.2 Inverse stress function $\hat{E}$

The inverse Laplace of stress function  $\hat{E}$  is more difficult. It contains factors  $1/s$ ,  $1/s^2$  but also factor  $e^{-\frac{|z|\sqrt{k^2 cK+s}}{\sqrt{cK}}}$ . This latter term is not easy to invert. The next holds.

$$\mathcal{L}^{-1}\left(\frac{1}{s^2}\right) = t\mathcal{H}(t). \quad (\text{A.49})$$

For deriving the inverse of the complex term the shift theorem is needed and the convolution theorem. The next steps are followed

1. The exponent is inverted

$$\mathcal{L}^{-1}\left(e^{-\frac{|z|}{\sqrt{cK}}\sqrt{s}}\right) = \frac{|z|}{\sqrt{cK}\sqrt{4\pi t^3}} e^{-\frac{z^2}{4ckt}}. \quad (\text{A.50})$$

2. Shift theorem  $\mathcal{L}^{-1}(F(s-a)) = e^{at}f(t)$  is used:

$$\mathcal{L}^{-1}\left(e^{-\frac{|z|}{\sqrt{cK}}\sqrt{k^2 cK+s}}\right) = \frac{|z|}{\sqrt{cK}\sqrt{4\pi t^3}} e^{-\frac{z^2}{4ckt} - k^2 cKt}. \quad (\text{A.51})$$

3. Convolution theorem  $\mathcal{L}^{-1}(FG) = f * g = \int g(t-\tau)f(\tau)d\tau$  is used:

$$\mathcal{L}^{-1}\left(\frac{e^{-\frac{|z|}{\sqrt{cK}}\sqrt{k^2 cK+s}}}{s^2}\right) = \int_0^t \frac{|z|(t-\tau)}{\sqrt{cK}\sqrt{4\pi\tau^3}} e^{-\frac{z^2}{4ck\tau} - k^2 cK\tau} d\tau. \quad (\text{A.52})$$

The integration in equation (A.52) is solved by substitution of  $x^2 = \tau$  ( $2x dx = d\tau$ ) and substitution of  $b = \frac{z^2}{4cK}$ ,  $a = k^2cK$ :

$$\begin{aligned}
 \mathcal{L}^{-1}(\dots) &= \int_0^t \frac{|z|(t-\tau)}{\sqrt{cK}\sqrt{4\pi\tau^3}} e^{-\frac{z^2}{4cK\tau} - k^2cK\tau} d\tau \\
 &= \frac{|z|}{\sqrt{cK\pi}} \int_0^{\sqrt{t}} \left(\frac{t}{x^2} - 1\right) e^{-\frac{z^2}{4cKx^2} - k^2cKx^2} dx \\
 &= -\frac{|z|}{\sqrt{cK\pi}} \int_0^{\sqrt{t}} \left(1 + t\frac{\partial}{\partial b}\right) e^{-\frac{b}{x^2} - ax^2} dx, \\
 &= -\frac{|z|}{\sqrt{cK\pi}} \left(1 + t\frac{\partial}{\partial b}\right) \int_0^{\sqrt{t}} e^{-\frac{b}{x^2} - ax^2} dx.
 \end{aligned} \tag{A.53}$$

This last integral can be solved by using the formula 7.4.33 of Abramowitz and Stegun [1]. The solution is a combination of error functions. Note that  $b$  is positive and therefore the

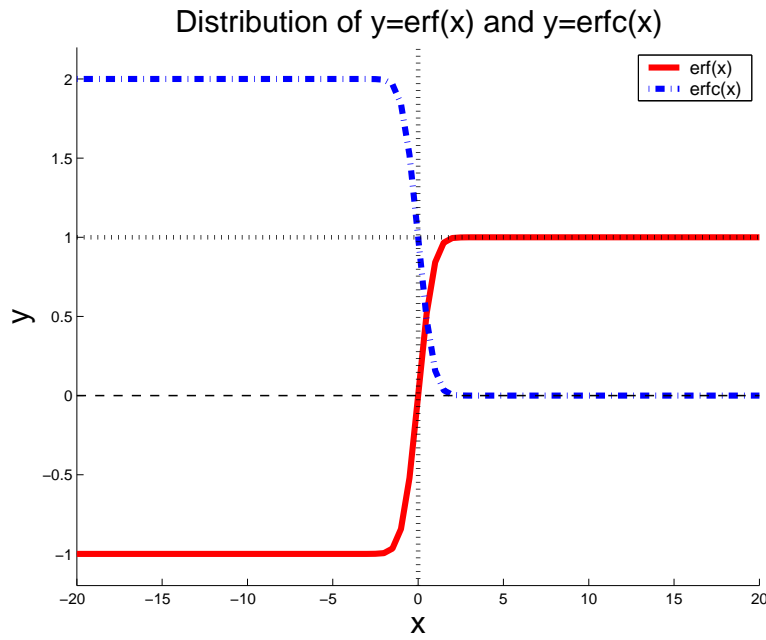


Figure A.1: Distribution of error function and its complementary.

next holds (See Figure A.1).

$$\begin{aligned}
 \lim_{x \downarrow 0} \operatorname{erf}(\sqrt{ax} - \sqrt{b}/x) &= \lim_{x \downarrow 0} \operatorname{erf}(-\sqrt{b}/x) = -1, \\
 \lim_{x \downarrow 0} \operatorname{erf}(\sqrt{ax} + \sqrt{b}/x) &= \lim_{x \downarrow 0} \operatorname{erf}(\sqrt{b}/x) = +1.
 \end{aligned} \tag{A.54}$$

$$\begin{aligned}
\mathcal{L}^{-1}(\dots) &= -\frac{|z|}{\sqrt{cK\pi}} \frac{\sqrt{\pi}}{4\sqrt{a}} (1 + t \frac{\partial}{\partial b}) \times \\
&\quad \left[ e^{2\sqrt{ab}} \operatorname{erf}(\sqrt{ax} + \sqrt{b}/x) + e^{-2\sqrt{ab}} \operatorname{erf}(\sqrt{ax} - \sqrt{b}/x) \right]_0^{\sqrt{t}} \\
&= -\frac{|z|}{\sqrt{cK}} \frac{1}{4\sqrt{a}} (1 + t \frac{\partial}{\partial b}) \times \\
&\quad \left( e^{2\sqrt{ab}} (-1 + \operatorname{erf}(\sqrt{at} + \sqrt{b/t})) + e^{-2\sqrt{ab}} (1 + \operatorname{erf}(\sqrt{at} - \sqrt{b/t})) \right) \\
&= +\frac{|z|}{4\sqrt{cKa}} (1 + t \frac{\partial}{\partial b}) \times \\
&\quad \left( e^{2\sqrt{ab}} \operatorname{erfc}(\sqrt{at} + \sqrt{b/t}) - e^{-2\sqrt{ab}} (2 - \operatorname{erfc}(\sqrt{at} - \sqrt{b/t})) \right)
\end{aligned} \tag{A.55}$$

with  $\operatorname{erf}(x) = \frac{2}{\sqrt{\pi}} \int_0^x e^{-t^2} dt$  the error function and  $\operatorname{erfc}(x) = 1 - \operatorname{erf}(x)$  its complementary. Considering that  $\frac{\partial \operatorname{erfc}(x)}{\partial x} = -2e^{-x^2} / \sqrt{\pi}$ , we find

$$\begin{aligned}
\frac{\partial}{\partial b} e^{2\sqrt{ab}} &= \frac{\sqrt{a}}{\sqrt{b}} e^{2\sqrt{ab}}, \\
\frac{\partial}{\partial b} \operatorname{erfc}(\sqrt{at} + \sqrt{b/t}) &= -\frac{1}{\sqrt{\pi bt}} e^{-(\sqrt{at} + \sqrt{b/t})^2} \\
\frac{\partial}{\partial b} e^{-2\sqrt{ab}} &= -\frac{\sqrt{a}}{\sqrt{b}} e^{-2\sqrt{ab}}, \\
\frac{\partial}{\partial b} \operatorname{erfc}(\sqrt{at} - \sqrt{b/t}) &= \frac{1}{\sqrt{\pi bt}} e^{-(\sqrt{at} - \sqrt{b/t})^2}
\end{aligned} \tag{A.56}$$

Then the derivatives of the error functions become

$$\begin{aligned}
\frac{\partial}{\partial b} (e^{2\sqrt{ab}} \operatorname{erfc}(\sqrt{at} + \sqrt{b/t})) &= \sqrt{a/b} e^{2\sqrt{ab}} \operatorname{erfc}(\sqrt{at} + \sqrt{b/t}) - \frac{e^{2\sqrt{ab}}}{\sqrt{\pi bt}} e^{-(\sqrt{at} + \sqrt{b/t})^2}, \\
\frac{\partial}{\partial b} (e^{-2\sqrt{ab}} \operatorname{erfc}(\sqrt{at} - \sqrt{b/t})) &= -\sqrt{a/b} e^{-2\sqrt{ab}} \operatorname{erfc}(\sqrt{at} - \sqrt{b/t}) + \frac{e^{-2\sqrt{ab}}}{\sqrt{\pi bt}} e^{-(\sqrt{at} - \sqrt{b/t})^2}.
\end{aligned} \tag{A.57}$$

And for the exponents holds

$$e^{-2\sqrt{ab}} e^{-(\sqrt{at} - \sqrt{b/t})^2} = e^{2\sqrt{ab}} e^{-(\sqrt{at} + \sqrt{b/t})^2} = e^{-(at+b/t)}. \tag{A.58}$$

Then differentiating with respect to  $b$  in equation (A.55), we find for the inverse Laplace of the exponent through convolution theory (equation (A.52)) and with  $b = \frac{z^2}{4cK}$  and  $a = k^2cK$ .

$$\begin{aligned}
\mathcal{L}^{-1}(\dots) &= \left( \frac{-|z|}{2|k|cK} + t \right) e^{-|k||z|} + \left( \frac{|z|}{4|k|cK} + t/2 \right) e^{+|k||z|} \operatorname{erfc}(|k|\sqrt{cKt} + |z|/\sqrt{4cKt}) \\
&\quad + \left( \frac{|z|}{4|k|cK} - t/2 \right) e^{-|k||z|} \operatorname{erfc}(|k|\sqrt{cKt} - |z|/\sqrt{4cKt}).
\end{aligned} \tag{A.59}$$

The complementary error function  $\operatorname{erfc}(x) = 1 - \operatorname{erf}(x)$  is introduced. This is convenient for the total expression for the stress function.

The Fourier transformed stress function  $\tilde{E}$  becomes

$$\begin{aligned}
\mathcal{L}^{-1}(\hat{E}) &= \tilde{E}(k, z, t) \\
&= \operatorname{sign}(z) \left\{ [-\tilde{g}(k)t - \frac{i\tilde{f}(k)}{2k}] e^{-|k||z|} \mathcal{H}(t) + \tilde{g}(k) \mathcal{L}^{-1} \left( \frac{e^{-\frac{1}{cK} \sqrt{k^2cK + s|z|}}}{s^2} \right) \right\},
\end{aligned} \tag{A.60}$$



with  $\tilde{g}(k) = ik\mu\tilde{f}(k)K$ . This expression for the stress function is reduced to

$$\begin{aligned}\tilde{E}(k, z, t) = & -\text{sign}(z) \left\{ \left[ \frac{i\tilde{f}(k)}{2k} + \frac{|z|}{2|k|cK} \tilde{g}(k) \right] e^{-|k||z|} \mathcal{H}(t) \right. \\ & - \tilde{g}(k) \left( \frac{t}{2} + \frac{|z|}{4|k|cK} \right) e^{|k||z|} \text{erfc}(|k|\sqrt{cKt} + |z|/\sqrt{4cKt}) \\ & \left. + \tilde{g}(k) \left( \frac{t}{2} - \frac{|z|}{4|k|cK} \right) e^{-|k||z|} \text{erfc}(|k|\sqrt{cKt} - |z|/\sqrt{4cKt}) \right\}.\end{aligned}\quad (\text{A.61})$$

or rewritten

$$\begin{aligned}\tilde{E}(k, z, t) = & -\frac{i\mu\tilde{f}(k)\text{sign}(z)}{2ck} \left\{ \left[ \frac{c}{\mu} + |z||k| \right] e^{-|k||z|} \mathcal{H}(t) \right. \\ & - cK(k^2t + \frac{|z||k|}{2cK}) e^{|k||z|} \text{erfc}(|k|\sqrt{cKt} + |z|/\sqrt{4cKt}) \\ & \left. + cK(k^2t - \frac{|z||k|}{2cK}) e^{-|k||z|} \text{erfc}(|k|\sqrt{cKt} - |z|/\sqrt{4cKt}) \right\}.\end{aligned}\quad (\text{A.62})$$

### A.6.3 Derivatives of Inverse Stress Functions

A short notation is introduced:

$$\begin{aligned}\text{erfc}(|k|\sqrt{cKt} - |z|/\sqrt{4cKt}) &= \text{erfc}(-), \\ \text{erfc}(|k|\sqrt{cKt} + |z|/\sqrt{4cKt}) &= \text{erfc}(+).\end{aligned}$$

Partial differentiation with respect to  $z$  results in:

$$\begin{aligned}\frac{\partial}{\partial z}(e^{-|k||z|}) &= -\text{sign}(z)|k|e^{-|k||z|} \\ \frac{\partial}{\partial z}(e^{|k||z|}) &= \text{sign}(z)|k|e^{|k||z|}\end{aligned}$$

and

$$e^{\pm|k||z|} \frac{\partial}{\partial z}(\text{erfc}(\pm)) = -\frac{\pm\text{sign}(z)}{\sqrt{\pi cKt}} e^{-(k^2cKt+z^2/(4cKt))}.$$

The first order derivatives with respect to  $z$  of the stress functions are given below.

$$\begin{aligned}\frac{\partial \tilde{E}}{\partial z}(k, z, t) &= \left\{ \left[ \frac{i|k|\tilde{f}(k)}{2k} + \frac{|z||k|-1}{2|k|cK} \tilde{g}(k) \right] e^{-|k||z|} \mathcal{H}(t) \right. \\ & + \tilde{g}(k) \left( \frac{t|k|}{2} + \frac{|z||k|+1}{4|k|cK} \right) e^{|k||z|} \text{erfc}(+) \\ & + \tilde{g}(k) \left( \frac{t|k|}{2} - \frac{|z||k|-1}{4|k|cK} \right) e^{-|k||z|} \text{erfc}(-) \\ & \left. - \frac{\tilde{g}(k)t}{\sqrt{\pi cKt}} e^{-(k^2cKt+z^2/(4cKt))} \right\}. \\ &= \frac{i\mu\tilde{f}(k)}{2ck} \left\{ |k| \left[ \frac{c}{\mu} + |z||k| - 1 \right] e^{-|k||z|} \mathcal{H}(t) \right. \\ & + |k|cK(k^2t + \frac{|z||k|+1}{2cK}) e^{|k||z|} \text{erfc}(+) \\ & + |k|cK(k^2t - \frac{|z||k|-1}{2cK}) e^{-|k||z|} \text{erfc}(-) \\ & \left. - 2\frac{k^2\sqrt{cKt}}{\sqrt{\pi}} e^{-(k^2cKt+z^2/(4cKt))} \right\}. \\ \frac{\partial \tilde{S}}{\partial z}(k, z, t) &= \frac{ik\text{sign}(z)}{2} \tilde{f}(k) e^{-|k||z|} \mathcal{H}(t).\end{aligned}\quad (\text{A.63})$$

The second order derivatives with respect to  $z$  are

$$\begin{aligned}
\frac{\partial^2 \tilde{E}}{\partial z^2}(k, z, t) &= -\text{sign}(z) \left\{ \left[ \frac{ik\tilde{f}(k)}{2} + \frac{|z|k^2 - 2\text{sign}(z)|k|}{2|k|cK} \tilde{g}(k) \right] e^{-|k||z|} \mathcal{H}(t) \right. \\
&\quad - \tilde{g}(k) \left( \frac{tk^2}{2} + \frac{|z||k| + 2\text{sign}(z)}{4cK} \right) e^{|k||z|} \text{erfc}(+) \\
&\quad \left. + \tilde{g}(k) \left( \frac{tk^2}{2} - \frac{|z||k| - 2\text{sign}(z)}{4cK} \right) e^{-|k||z|} \text{erfc}(-) \right\} \\
&= -\frac{i\mu\tilde{f}(k)\text{sign}(z)}{2ck} \left\{ k^2 \left[ \frac{c}{\mu} + |z||k| - 2 \right] e^{-|k||z|} \mathcal{H}(t) \right. \\
&\quad - k^2 cK \left( k^2 t + \frac{|z||k| + 2}{2cK} \right) e^{|k||z|} \text{erfc}(+) \\
&\quad \left. + k^2 cK \left( k^2 t - \frac{|z||k| - 2}{2cK} \right) e^{-|k||z|} \text{erfc}(-) \right\}. \\
\frac{\partial^2 \tilde{S}}{\partial z^2}(k, z, t) &= -\frac{ik|k|}{2} \tilde{f}(k) e^{-|k||z|} \mathcal{H}(t).
\end{aligned} \tag{A.64}$$

They indeed fulfil the jump conditions.

### A.6.4 Other Inverse Laplace

The shear stress in Fourier transforms become:

$$\begin{aligned}
\tilde{\sigma}_{xz} &= 2\mu ik \left\{ \frac{\partial \tilde{E}}{\partial z} - z \frac{\partial \tilde{S}}{\partial z} \right\}. \\
&= 2\mu \left\{ \left[ \frac{-(|k| - |z|k^2)\tilde{f}(k)}{2} + \frac{|z||k| - 1}{2|k|cK} \tilde{g}(k) \right] e^{-|k||z|} \mathcal{H}(t) \right. \\
&\quad + ik\tilde{g}(k) \left( \frac{t|k|}{2} + \frac{|z||k| + 1}{4|k|cK} \right) e^{|k||z|} \text{erfc}(+) \\
&\quad + ik\tilde{g}(k) \left( \frac{t|k|}{2} - \frac{|z||k| - 1}{4|k|cK} \right) e^{-|k||z|} \text{erfc}(-) \\
&\quad \left. - ik \frac{\tilde{g}(k)t}{\sqrt{\pi cKt}} e^{-(k^2 cKt + z^2 / (4cKt))} \right\} \\
&= \frac{-\mu^2 \tilde{f}(k)|k|}{c} \left\{ \left[ - \left( 1 - \frac{c}{\mu} \right) (1 - |z||k|) \right] e^{-|k||z|} \mathcal{H}(t) \right. \\
&\quad + cK \left( k^2 t + \frac{|z||k| + 1}{2cK} \right) e^{|k||z|} \text{erfc}(+) \\
&\quad + cK \left( k^2 t - \frac{|z||k| - 1}{2cK} \right) e^{-|k||z|} \text{erfc}(-) \\
&\quad \left. - 2|k| \frac{\sqrt{cKt}}{\sqrt{\pi}} e^{-(k^2 cKt + z^2 / (4cKt))} \right\}
\end{aligned} \tag{A.65}$$

Also the chemical potential can be calculated. It is given by

$$\begin{aligned}
\tilde{\mu}^f &= c \left( \frac{\partial^2}{\partial z^2} - k^2 \right) \tilde{E} - 2\mu \frac{\partial \tilde{S}}{\partial z} - RT\Gamma C_0 2\pi\delta(k). \\
&= \frac{\text{sign}(z)}{K} \tilde{g}(k) e^{-|k||z|} \mathcal{H}(t) + \frac{\tilde{g}(k)\text{sign}(z)}{2K} (e^{|k||z|} \text{erfc}(+) + e^{-|k||z|} \text{erfc}(-)) \\
&\quad - ik\mu\tilde{f}(k) e^{-|k||z|} - RT\Gamma C_0 2\pi\delta(k), \\
&= \frac{i\mu k \tilde{f}(k) \text{sign}(z)}{2} \left\{ e^{|k||z|} \text{erfc}(+) - e^{-|k||z|} \text{erfc}(-) \right\} - RT\Gamma C_0 2\pi\delta(k)
\end{aligned} \tag{A.66}$$

## A.7 Inverse Fourier transform

The shear fault is caused by a dislocation. Then the slip function becomes:

$$f(x) = d(\mathcal{H}(L + x) - \mathcal{H}(L - x)). \tag{A.67}$$

The Fourier transformed is

$$\tilde{f}(k) = \int_{-L}^L de^{-ikx} dx = \frac{2d\sin(Lk)}{k}. \quad (\text{A.68})$$

The function  $\tilde{g}(k)$  becomes in spatial domain:

$$\begin{aligned} g(x) &= \mathcal{F}^{-1}\left(ik\mu\tilde{f}(k)K\right) \\ &= -\mu K \frac{\partial f(x)}{\partial x} \\ &= -\mu dK(\delta(L+x) - \delta(L-x)) \end{aligned} \quad (\text{A.69})$$

The shear stress is difficult to calculate. The solution at the crack surface is considered, namely at  $z = 0$ . Then the shear stress is given by

$$\begin{aligned} \tilde{\sigma}_{xz}(k, 0, t) &= -2\mu \left[ \frac{|k|\tilde{f}(k)}{2} + \frac{ik}{2|k|cK} \tilde{g}(k) \right] \mathcal{H}(t) \\ &\quad + 2\mu \tilde{g}(k) \left\{ (itk|k| + \frac{ik}{2|k|cK}) \operatorname{erfc}(|k|\sqrt{cKt}) - \frac{ikt}{\sqrt{\pi cKt}} e^{-k^2 cKt} \right\} \\ &= \frac{-\mu^2 \tilde{f}(k)|k|}{c} \left\{ \left[ -\left(1 - \frac{c}{\mu}\right) \right] \mathcal{H}(t) \right. \\ &\quad \left. + (2k^2 cKt + 1) \operatorname{erfc}(|k|\sqrt{cKt}) - 2 \frac{\sqrt{k^2 cKt}}{\sqrt{\pi}} e^{-(k^2 cKt)} \right\} \end{aligned} \quad (\text{A.70})$$

Abramowitz and Stegun [1] paragraph 7.2 deals with repeated integrals of the complementary error function  $i^n \operatorname{erfc}(\lambda)$ :

$$i^n \operatorname{erfc}(\lambda) = \int_{\lambda}^{\infty} i^{n-1} \operatorname{erfc}(l) dl. \quad (\text{A.71})$$

with

$$\begin{aligned} i^n \operatorname{erfc}(\lambda) &= \frac{2}{\sqrt{\pi}} \int_{\lambda}^{\infty} \frac{(l-\lambda)^n}{n!} e^{-l^2} dl, \\ &= -\frac{\lambda}{n} i^{n-1} \operatorname{erfc}(\lambda) + \frac{1}{2n} i^{n-2} \operatorname{erfc}(\lambda) \\ i^0 \operatorname{erfc}(\lambda) &= \operatorname{erfc}(\lambda), \\ i^{-1} \operatorname{erfc}(\lambda) &= \frac{2}{\sqrt{\pi}} e^{-\lambda^2}. \end{aligned} \quad (\text{A.72})$$

We can derive that

$$\begin{aligned} i^1 \operatorname{erfc}(\lambda) &= -\lambda \operatorname{erfc}(\lambda) + \frac{1}{\sqrt{\pi}} e^{-\lambda^2}. \\ i^2 \operatorname{erfc}(\lambda) &= \frac{1}{4} \left\{ (1 + 2\lambda^2) \operatorname{erfc}(\lambda) - 2 \frac{\lambda}{\sqrt{\pi}} e^{-\lambda^2} \right\} \end{aligned} \quad (\text{A.73})$$

With  $\lambda = \sqrt{k^2 c K t}$  and a factor  $\frac{2ik}{cK|k|}$  we have found for (A.70)

$$\tilde{\sigma}_{xz}(k, 0, t) = \frac{-\mu^2 |k| \tilde{f}(k)}{c} \left\{ - \left(1 - \frac{c}{\mu}\right) \mathcal{H}(t) + 4i^2 \operatorname{erfc}(\sqrt{k^2 c K t}) \right\}. \quad (\text{A.74})$$

For calculating the inverse Fourier, the first and second term are calculated separately. Since  $\tilde{f}(k)$  is symmetric and  $|k|$  is symmetric, the first term is symmetric. For the inverse Fourier transformation this means that only the real part, i.e. symmetric part, of  $e^{ikx} = \cos(kx) + i\sin(kx)$  will contribute to the final result. This property is shown below.

$$\begin{aligned} \mathcal{F}^{-1}(|k| \tilde{f}(k)) &= \int_{-\infty}^{\infty} 2d|k| \frac{\sin(kL)}{k} e^{ikx} dk \\ &= \frac{d}{\pi} \int_{-\infty}^{\infty} |k| \frac{\sin(kL)}{k} (\cos(kx) + i\sin(kx)) dk \\ &= \frac{d}{\pi} \left( \int_{-\infty}^0 -\sin(kL) (\cos(kx) + i\sin(kx)) dk + \int_0^{\infty} \sin(kL) (\cos(kx) + i\sin(kx)) dk \right) \\ &= \frac{d}{\pi} \left( \int_0^{\infty} \sin(kL) (\cos(kx) - i\sin(kx)) (-dk) + \int_0^{\infty} \sin(kL) (\cos(kx) + i\sin(kx)) dk \right) \\ &= \frac{2d}{\pi} \int_0^{\infty} \sin(kL) \cos(kx) dk. \end{aligned} \quad (\text{A.75})$$

The result of the first Fourier inverse is

$$\begin{aligned} \mathcal{F}^{-1}(|k| \tilde{f}(k)) &= \frac{2d}{\pi} \int_0^{\infty} \sin(kL) \cos(kx) dk \\ &= \frac{2d}{\pi} \frac{(L-x) \cos((L+x)x) + (L+x) \cos((L-x)x)}{2(x^2 - L^2)} \Big|_0^{\infty}, \\ &= \frac{2d}{\pi} \frac{L}{(L^2 - x^2)}. \end{aligned} \quad (\text{A.76})$$

The error function  $i^2 \operatorname{erfc}(\sqrt{k^2 c K t})$  is symmetric in  $k$ . This means that the second part of the shear stress is symmetric in  $k$  too. The real part of  $e^{ikx}$  will only contribute. This way the inverse Fourier reduces to

$$\begin{aligned} \mathcal{F}^{-1}(|k| \tilde{f}(k) i^2 \operatorname{erfc}(\sqrt{k^2 c K t})) &= \int_{-\infty}^{\infty} \tilde{f}(k) |k| i^2 \operatorname{erfc}(\sqrt{k^2 c K t}) e^{ikx} dk \\ &= \frac{2d}{\pi} \int_0^{\infty} i^2 \operatorname{erfc}(\sqrt{k^2 c K t}) \sin(kL) \cos(kx) dk \\ &= \frac{2d}{\pi} \operatorname{Int}_{i^2 \operatorname{erfc}}. \end{aligned} \quad (\text{A.77})$$

The integral  $\operatorname{Int}_{i^2 \operatorname{erfc}} = \int_0^{\infty} i^2 \operatorname{erfc}(\sqrt{k^2 c K t}) \sin(kL) \cos(kx) dk$  is introduced. By partial integration we find that the next integral can be derived. The property  $\lim_{x \rightarrow \infty} i^n \operatorname{erfc}(x) =$

0 is used.

$$\begin{aligned}
Int_{i^2 erf c} &= \int_0^{\infty} i^2 erf c(\sqrt{k^2 c K t}) \sin(kL) \cos(kx) dk \\
&= \left[ \frac{1}{x} i^2 erf c(\sqrt{k^2 c K t}) \sin(kL) \sin(kx) \right]_0^{\infty} \\
&\quad - \int_0^{\infty} \left\{ \frac{-\sqrt{c K t}}{x} i^1 erf c(\sqrt{k^2 c K t}) \sin(kL) + \frac{1}{x} i^2 erf c(\sqrt{k^2 c K t}) \cos(kL) \right\} \sin(kx) dk, \\
&= 0 + \left[ \left\{ \frac{-\sqrt{c K t}}{x^2} i^1 erf c(\sqrt{k^2 c K t}) \sin(kL) + \frac{1}{x^2} i^2 erf c(\sqrt{k^2 c K t}) \cos(kL) \right\} \cos(kx) \right]_0^{\infty} \\
&\quad - \int_0^{\infty} \left\{ \frac{c K t}{x^2} erf c(\sqrt{k^2 c K t}) \sin(kL) - 2 \frac{L \sqrt{c K t}}{x^2} i^1 erf c(\sqrt{k^2 c K t}) \cos(kL) \right\} \cos(kx) dk \\
&\quad + \frac{L^2}{x^2} Int_{i^2 erf c}, \\
&= -\frac{L}{x^2} i^2 erf c(0) + \frac{L^2}{x^2} Int_{i^2 erf c} - \frac{c K t}{x^2} \int_0^{\infty} erf c(\sqrt{k^2 c K t}) \sin(kL) \cos(kx) dk \\
&\quad + 2 \frac{L \sqrt{c K t}}{x^2} \int_0^{\infty} i^1 erf c(\sqrt{k^2 c K t}) \cos(kL) \cos(kx) dk, \\
&= \frac{1}{L^2 - x^2} \left\{ + L i^2 erf c(0) + c K t Int_{erf c} - 2 L \sqrt{c K t} Int_{i^1 erf c} \right\}.
\end{aligned} \tag{A.78}$$

We denote  $Int_{i^1 erf c} = \int_0^{\infty} erf c(\sqrt{k^2 c K t}) \cos(kL) \cos(kx) dk$ :

$$\begin{aligned}
Int_{i^1 erf c} &= \int_0^{\infty} erf c(\sqrt{k^2 c K t}) \cos(kL) \cos(kx) dk \\
&= 0 - \frac{1}{x} \int_0^{\infty} \left\{ -\sqrt{c K t} erf c(\sqrt{k^2 c K t}) \cos(kL) - L i^1 erf c(\sqrt{k^2 c K t}) \sin(kL) \right\} \sin(kx) dk \\
&= \frac{\sqrt{c K t}}{x} \int_0^{\infty} erf c(\sqrt{k^2 c K t}) \cos(kL) \sin(kx) dk - \frac{L}{x^2} \int_0^{\infty} i^1 erf c(\sqrt{k^2 c K t}) \sin(kL) d \cos(kx), \\
&= \frac{\sqrt{c K t}}{x} \int_0^{\infty} erf c(\sqrt{k^2 c K t}) \cos(kL) \sin(kx) dk - 0 \\
&\quad + \frac{L}{x^2} \int_0^{\infty} \left\{ -\sqrt{c K t} erf c(\sqrt{k^2 c K t}) \sin(kL) + L i^1 erf c(\sqrt{k^2 c K t}) \cos(kL) \right\} \cos(kx) dk \\
&= \frac{\sqrt{c K t}}{x} \int_0^{\infty} erf c(\sqrt{k^2 c K t}) \left\{ \cos(kL) \sin(kx) - \frac{L}{x} \sin(kL) \cos(kx) \right\} dk + \frac{L^2}{x^2} Int_{i^1 erf c}, \\
&= -\frac{x \sqrt{c K t}}{L^2 - x^2} \int_0^{\infty} erf c(\sqrt{k^2 c K t}) \left\{ \cos(kL) \sin(kx) - \frac{L}{x} \sin(kL) \cos(kx) \right\} dk.
\end{aligned} \tag{A.79}$$

The integral left is similar to  $Int_{erf c}$ , but with  $x$  and  $L$  the other way around. We denote

$Int_{erf c} = \int_0^{\infty} erf c(\sqrt{k^2 c K t}) \sin(kL) \cos(kx) dk$ :

$$\begin{aligned}
Int_{erf c} &= \int_0^{\infty} erf c(\sqrt{k^2 c K t}) \sin(kL) \cos(kx) dk \\
&= \left[ \frac{1}{x} erf c(\sqrt{k^2 c K t}) \sin(kL) \sin(kx) \right]_0^{\infty} \\
&\quad - \int_0^{\infty} \frac{1}{x} \left\{ -\frac{2\sqrt{c K t}}{\sqrt{\pi}} e^{-k^2 c K t} \sin(kL) + L erf c(\sqrt{k^2 c K t}) \cos(kL) \right\} \sin(kx) dk \\
&= 0 + \int_0^{\infty} \frac{1}{x} \frac{2\sqrt{c K t}}{\sqrt{\pi}} e^{-k^2 c K t} \sin(kL) \sin(kx) dk + \left[ \frac{L}{x^2} erf c(\sqrt{k^2 c K t}) \cos(kL) \cos(kx) \right]_0^{\infty} \\
&\quad - \frac{L}{x^2} \int_0^{\infty} \frac{2\sqrt{c K t}}{\sqrt{\pi}} e^{-k^2 c K t} \cos(kL) \cos(kx) dk + \frac{L^2}{x^2} Int_{erf c} \\
&= -\frac{L erf c(0)}{x^2} + \int_0^{\infty} \frac{1}{x} \frac{2\sqrt{c K t}}{\sqrt{\pi}} e^{-k^2 c K t} \left\{ \sin(kL) \sin(kx) + \frac{L}{x} \cos(kL) \cos(kx) \right\} dk + \frac{L^2}{x^2} Int_{erf c} \\
&= \frac{1}{L^2 - x^2} \left\{ L erf c(0) - \frac{2x \sqrt{c K t}}{\sqrt{\pi}} Int_{exp} \right\}
\end{aligned} \tag{A.80}$$

The last unknown integral is the one in  $Int_{exp}$ . This integral is derived here.

$$\begin{aligned}
Int_{exp} &= \int_0^{\infty} e^{-k^2 c K t} \left\{ \sin(kL) \sin(kx) + \frac{L}{x} \cos(kL) \cos(kx) \right\} dk \\
&= \int_0^{\infty} e^{-k^2 c K t} \left\{ \frac{(L-x)}{2x} \cos((L+x)k) + \frac{(L+x)}{2x} \cos((L-x)k) \right\} dk, \\
&= \frac{(L-x)}{4x} \int_0^{\infty} \left\{ e^{-k^2 c K t + i(L+x)k} + e^{-k^2 c K t - i(L+x)k} \right\} dk \\
&\quad + \frac{(L+x)}{4x} \int_0^{\infty} \left\{ e^{-k^2 c K t + i(L-x)k} + e^{-k^2 c K t - i(L-x)k} \right\} dk, \\
&= \frac{(L-x)}{4x} \int_0^{\infty} e^{-\frac{(L+x)^2}{4cKt}} \left\{ e^{-(k\sqrt{cKt} + i\frac{(L+x)}{2\sqrt{cKt}})^2} + e^{-(k\sqrt{cKt} - i\frac{(L+x)}{2\sqrt{cKt}})^2} \right\} dk \\
&\quad + \frac{(L+x)}{4x} \int_0^{\infty} e^{-\frac{(L-x)^2}{4cKt}} \left\{ e^{-(k\sqrt{cKt} + i\frac{(L-x)}{2\sqrt{cKt}})^2} + e^{-(k\sqrt{cKt} - i\frac{(L-x)}{2\sqrt{cKt}})^2} \right\} dk, \\
&= -\frac{(L+x)}{4x} e^{-\frac{(L-x)^2}{4cKt}} \frac{\sqrt{\pi}}{2\sqrt{cKt}} \left\{ \operatorname{erfc}\left(-i\frac{(L+x)}{2\sqrt{cKt}}\right) + \operatorname{erfc}\left(i\frac{(L+x)}{2\sqrt{cKt}}\right) \right\} \\
&\quad + \frac{(L+x)}{4x} e^{-\frac{(L-x)^2}{4cKt}} \frac{\sqrt{\pi}}{2\sqrt{cKt}} \left\{ \operatorname{erfc}\left(-i\frac{(L-x)}{2\sqrt{cKt}}\right) + \operatorname{erfc}\left(i\frac{(L-x)}{2\sqrt{cKt}}\right) \right\} \\
&= \frac{(L-x)}{4x} \frac{\sqrt{\pi}}{\sqrt{cKt}} e^{-\frac{(L+x)^2}{4cKt}} + \frac{(L+x)}{4x} \frac{\sqrt{\pi}}{\sqrt{cKt}} e^{-\frac{(L-x)^2}{4cKt}}.
\end{aligned} \tag{A.81}$$

Then

$$\begin{aligned}
Int_{erfc} &= \frac{\operatorname{Lerfc}(0)}{L^2 - x^2} - \frac{1}{2(L+x)} e^{-\frac{(L+x)^2}{4cKt}} - \frac{1}{2(L-x)} e^{-\frac{(L-x)^2}{4cKt}} \\
Int_{i^1 erfc} &= \frac{\sqrt{cKt}}{L^2 - x^2} \left\{ \frac{L^2 + x^2}{L^2 - x^2} \operatorname{erfc}(0) - \frac{(L-x)}{2(L+x)} e^{-\frac{(L+x)^2}{4cKt}} - \frac{(L+x)}{2(L-x)} e^{-\frac{(L-x)^2}{4cKt}} \right\} \\
&= \sqrt{cKt} \left\{ \frac{L^2 + x^2}{(L^2 - x^2)^2} \operatorname{erfc}(0) - \frac{1}{2(L+x)^2} e^{-\frac{(L+x)^2}{4cKt}} - \frac{1}{2(L-x)^2} e^{-\frac{(L-x)^2}{4cKt}} \right\}
\end{aligned} \tag{A.82}$$

All the separate integrals have been determined and we find for  $Int_{i^2 erfc}$  the next solution.

$$\begin{aligned}
Int_{i^2 erfc} &= \frac{1}{L^2 - x^2} \left\{ Li^2 \operatorname{erfc}(0) + cKt Int_{erfc} - 2L\sqrt{cKt} Int_{i^1 erfc} \right\} \\
&= \frac{1}{(L^2 - x^2)} \left\{ Li^2 \operatorname{erfc}(0) - cKt \frac{3Lx^2 + L^3}{(L^2 - x^2)^2} \operatorname{erfc}(0) \right. \\
&\quad \left. + cKt \left( \frac{(L-x)}{2(L+x)^2} e^{-\frac{(L+x)^2}{4cKt}} + \frac{(L+x)}{2(L-x)^2} e^{-\frac{(L-x)^2}{4cKt}} \right) \right\}.
\end{aligned} \tag{A.83}$$

Furthermore for the repetitive error function holds:

$$\begin{aligned}
i^n \operatorname{erfc}(\infty) &= 0 \\
i^n \operatorname{erfc}(0) &= [2^n \Gamma(n/2 + 1)]^{-1} \\
\Gamma(n) &= (n-1)!, \quad n \in \mathcal{N}^+.
\end{aligned} \tag{A.84}$$

The next holds:

$$\frac{(L+x)}{2(L-x)^2} + \frac{(L-x)}{2(L+x)^2} = \frac{(L+x)^3 + (L-x)^3}{2(L^2 - x^2)^2} = \frac{3Lx^2 + L^3}{(L^2 - x^2)^2} \tag{A.85}$$

We have found for  $Int_{i^2erfc}$

$$Int_{i^2erfc} = \frac{1}{L^2-x^2} \left\{ \frac{L}{4} - cKt \left( \frac{(L-x)}{2(L+x)^2} (1 - e^{-\frac{(L+x)^2}{4cKt}}) + \frac{(L+x)}{2(L-x)^2} (1 - e^{-\frac{(L-x)^2}{4cKt}}) \right) \right\} \quad (\text{A.86})$$

Then the shear stress is given by equation (A.74)

$$\begin{aligned} \sigma_{xz}(x,0,t) &= \mathcal{F}^{-1} \left( \frac{-\mu^2 |k| \tilde{f}(k)}{c} \left\{ - \left(1 - \frac{c}{\mu}\right) \mathcal{H}(t) + 4i^2 erfc(\sqrt{k^2 c K t}) \right\} \right) \\ &= \frac{-\mu^2 \mathcal{H}(t)}{c} \left\{ - \left(1 - \frac{c}{\mu}\right) \mathcal{F}^{-1} \left( |k| \tilde{f}(k) \right) + 4 \mathcal{F}^{-1} \left( i^2 erfc(\sqrt{k^2 c K t}) |k| \tilde{f}(k) \right) \right\} . \quad (\text{A.87}) \\ &= \frac{-2\mu \mathcal{H}(t) d}{\pi} \left\{ \left(1 - \frac{\mu}{c}\right) \frac{L}{L^2-x^2} + 4 \frac{\mu}{c} Int_{i^2erfc} \right\} \end{aligned}$$

which leads to

$$\sigma_{xz}(x,0,t) = \frac{-2\mu \mathcal{H}(t) d}{\pi(L^2-x^2)} \left\{ L - \mu K F(x,t) \right\} \quad (\text{A.88})$$

with

$$F(x,t) = 2t \frac{(L-x)}{(L+x)^2} (1 - e^{-\frac{(L+x)^2}{4cKt}}) + \frac{(L+x)}{(L-x)^2} (1 - e^{-\frac{(L-x)^2}{4cKt}}) \quad (\text{A.89})$$

## A.8 Chemical potential and flow

The chemical potential does not only satisfies Eq. (3.9), but it also satisfies Eq.(3.28), with  $S$  time independent. Assuming almost circular diffusion from the crack-tip, the equation can be solved using Hankel transformation. [15,76]. The result is that the chemical potential follows

$$\mu^f = (1 - e^{-r^2/4cKt}) \mu_0^f \quad \mu_0^f = AL \frac{\sin(\theta)}{r} \quad (\text{A.90})$$

with local polar coordinate  $r$  defined as the radius at one of the two crack-tips and  $\theta$  the angle with  $x$ -axis. The parameter  $A$  is a measure for the offset:  $A = \frac{2\mu db}{2\pi L}$ . In  $x, z$ -plane, this becomes

$$\begin{aligned} \mu^f &= \frac{2\mu d}{L} \frac{z}{2\pi L} \left[ \frac{L^2}{(x-L)^2+z^2} - \frac{L^2}{(x+L)^2+z^2} \right] \\ &\quad - \frac{2\mu d}{L} \frac{z}{2\pi L} e^{-z^2/4cKt} \left[ \frac{L^2 e^{-(x-L)^2/4cKt}}{(x-L)^2+z^2} - \frac{L^2 e^{-(x+L)^2/4cKt}}{(x+L)^2+z^2} \right] \end{aligned} \quad (\text{A.91})$$

and therefore (A.92) holds.

$$\begin{aligned} \mu^f &= \frac{\mu dz}{\pi} \left[ \frac{1}{(x-L)^2+z^2} - \frac{1}{(x+L)^2+z^2} \right] \\ &\quad - \frac{\mu dz}{\pi} e^{-z^2/4cKt} \left[ \frac{e^{-(x-L)^2/4cKt}}{(x-L)^2+z^2} - \frac{e^{-(x+L)^2/4cKt}}{(x+L)^2+z^2} \right] \end{aligned} \quad (\text{A.92})$$

From this we can derive the flow over the crack ( $\vec{n}$  vector normal to the crack):

$$\begin{aligned}
 \vec{q} \cdot \vec{n} = -K \frac{\partial \mu^f}{\partial z} = & -K \frac{\mu d}{\pi} \left[ \frac{1}{(x-L)^2+z^2} - \frac{1}{(x+L)^2+z^2} \right] \\
 & + K \frac{2\mu dz^2}{\pi} \left[ \frac{1}{((x-L)^2+z^2)^2} - \frac{1}{((x+L)^2+z^2)^2} \right] \\
 & + K \frac{\mu d(1-2z^2/4cKt)}{\pi} e^{-z^2/4cKt} \left[ \frac{e^{-(x-L)^2/4cKt}}{(x-L)^2+z^2} - \frac{e^{-(x+L)^2/4cKt}}{(x+L)^2+z^2} \right] \\
 & - K \frac{2\mu dz^2}{\pi} e^{-z^2/4cKt} \left[ \frac{e^{-(x-L)^2/4cKt}}{((x-L)^2+z^2)^2} - \frac{e^{-(x+L)^2/4cKt}}{((x+L)^2+z^2)^2} \right]
 \end{aligned} \tag{A.93}$$

and the flow along the crack ( $\vec{t}$  vector in direction of crack-tip  $x = +L$ ):

$$\begin{aligned}
 \vec{q} \cdot \vec{t} = -K \frac{\partial \mu^f}{\partial x} = & \frac{\mu dz}{\pi} \left[ \frac{-2(x-L)}{(x-L)^2+z^2} - \frac{-2(x+L)}{(x+L)^2+z^2} \right] \\
 & - \frac{\mu dz}{\pi} e^{-z^2/4cKt} \left[ \frac{\frac{-2(x-L)}{4cKt} e^{-(x-L)^2/4cKt}}{(x-L)^2+z^2} - \frac{\frac{-2(x+L)}{4cKt} e^{-(x+L)^2/4cKt}}{(x+L)^2+z^2} \right] \\
 & - \frac{\mu dz}{\pi} e^{-z^2/4cKt} \left[ \frac{-2(x-L) e^{-(x-L)^2/4cKt}}{((x-L)^2+z^2)^2} - \frac{-2(x+L) e^{-(x+L)^2/4cKt}}{((x+L)^2+z^2)^2} \right]
 \end{aligned} \tag{A.94}$$





## APPENDIX B

# Numerical aspects of a discontinuity

In this appendix some features of the two standard models are repeated and elaborated with pictures.

### B.1 Discontinuities and FEM

The modes of failure are represented in Fig. B.1.

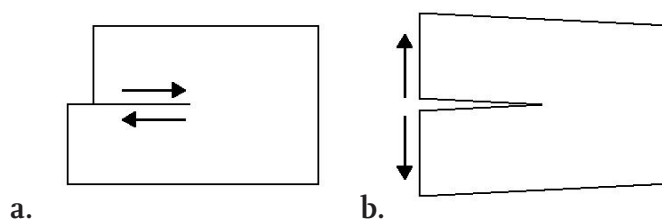


**Figure B.1:** Representation of **a.** mode II or shear loading and **b.** mode I or tensile loading

The mathematical representation of discontinuities are different than the representation in the FEM. Two methods are compared, Fig. B.2. The basis functions are enhanced with

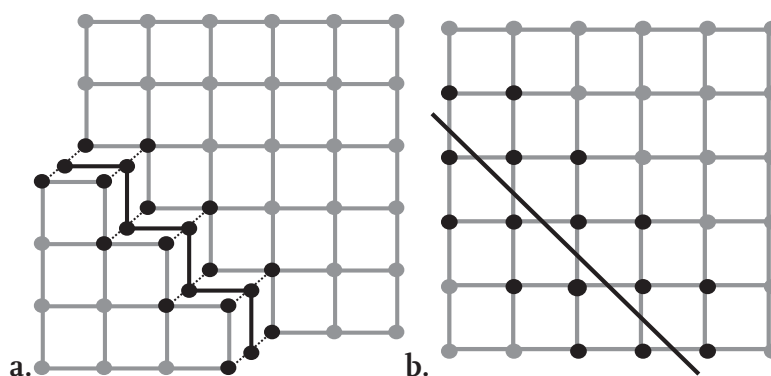


**Figure B.2:** **a.** Using interface model, extra nodes are introduced to represent crack. **b.** Using PUM, the discontinuity is projected on the mesh by increasing the degrees of freedom of the existing nodes.

the following discontinuities.

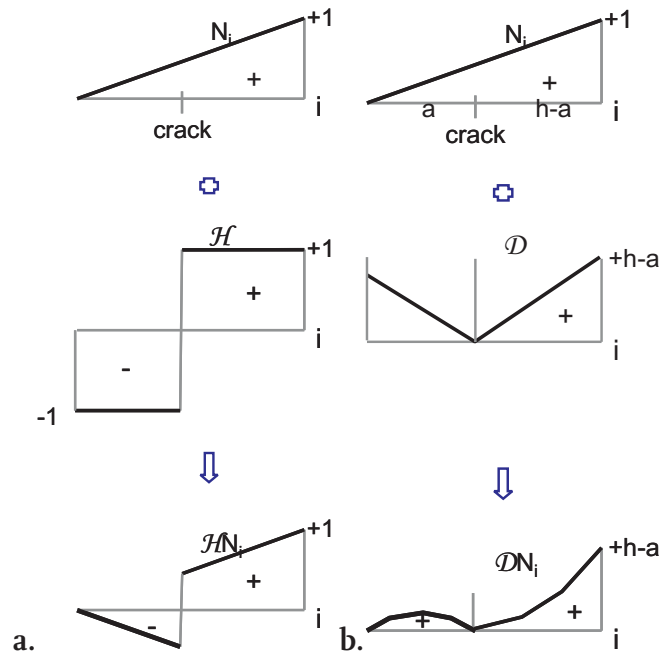


Figure B.3: Enhancing the basis functions for a. Strong discontinuity b. Weak discontinuity.

## B.2 Cohesive zone

The cohesive zone model represents a damage evolution. The evolution can be represented as (nonlinear) springs.

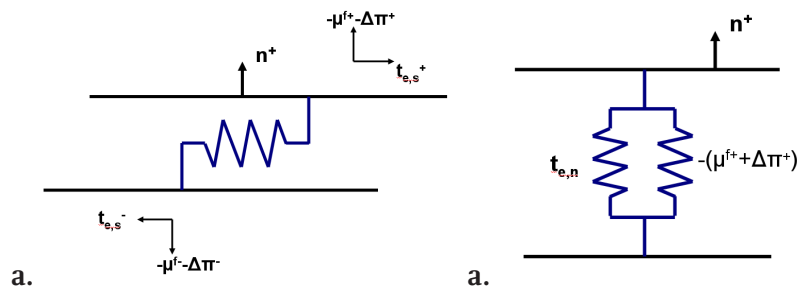


Figure B.4: Traction forces at the discontinuity represented as (nonlinear) springs for a. Shear loading b. Tensile loading.

## B.3 Yield criterion

The direction of crack growth is chosen nonlocally, since the local stress field is not known at the crack-tip and cannot be calculated reliable locally. The stress field is calculated nonlocally by integration over an area around the tip using

$$\begin{aligned}\sigma_{tip} &= \sum_{i=1}^{n_{tot}} \frac{w_i}{w_{tot}} \sigma_i \\ w_{tot} &= \sum_{j=1}^{n_{tot}} w_j \\ w_i &= \frac{(2\pi)^{2/3}}{l_a^3} e^{-\frac{r_i^2}{2l_a^2}}.\end{aligned}\tag{B.1}$$

with  $r_i$  the distance between integration point  $i$  and the crack-tip and  $l_a$  is a length scale parameter which determines the influence of a sample point. Typically  $l_a$  is a material length scale. Fig. B.5 shows the integration area. The wider the area the more the stress field is spread and the less the steepness of the stress field.

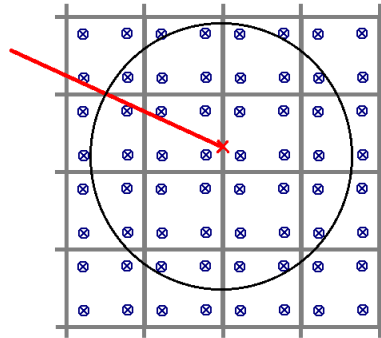


Figure B.5: Circle of influence for determining the stress state at the crack tip.

## B.4 Implementation aspects

This section is adopted from the thesis of Wells [106] and Remmers [78].

During a calculation, the initiation criterion is monitored. Each time step (increment), the system of equations are solved iteratively with the Newton-Rhapson procedure. When the solution of the increment has converged, the propagation criterion is checked. When the criterion is met, a discontinuity is introduced through the entire element. The assumption of one element crossed straight at one time step is one for implementation and not of formulation. This assumption avoids spurious unloading and sudden jumps in the solution [107]. This assumption is of no consequences upon mesh-refinement. Furthermore the solution depends more on energy dissipation through opening of sliding in the cohesive zone, then on moment of extension. The extension is at the end of the time increment, to keep the quadratic convergence of the Newton-Rhapson procedure.

Only elements crossed by a strong discontinuity are enhanced by the Heaviside function, since the Heaviside function is constant in all other elements, which is already included in the span of the basis functions. Furthermore only elements crossed by a weak discontinuity are enhanced by a distance function for practical issues. This assumption is of no consequences, when the effect of the discontinuity is local. .

If only a very small portion of the element is crossed by a discontinuity, the volume of either  $\Omega^+$  ( $\Omega_s^+$ ) or  $\Omega^-$  ( $\Omega_s^-$ ) is small, the Heaviside function is almost constant throughout the element. To ensure a well-conditioned stiffness matrix, i.e. stable calculations, only the nodes are enhanced when the support contributes sufficiently to the stiffness matrix. In other words only all nodes of the element are enhanced when the support is crossed by a discontinuity and the next holds:

$$\frac{\min(\Omega_s^+, \Omega_s^-)}{\Omega_s} > \epsilon_{tol} \quad (\text{B.2})$$

with  $\Omega_s$  the volume of a support of a node and  $\epsilon_{tol}$  the tolerance level dependent on the solver. Last but not least, the nodes on the element boundary including the crack-tip are not enhanced, to enforce zero opening at the tip,  $[\vec{u}] = \vec{0}$ .

The difficulty of integration of enhanced elements lies with adequately integration of both sides of the discontinuity. For the partition of unity method continuous or standard elements are integrated in a standard FE way, using Gauss integration scheme and have nodal degrees of freedom  $\vec{a}_u$  and  $a_\mu$ . Elements crossed by a discontinuity have nodal degrees of freedom  $\vec{a}_u$ ,  $a_\mu$ ,  $\vec{b}_u$  and  $b_\mu$ . When an element is crossed by the discontinuity for the first time, the separate domains  $\Omega^+$  and  $\Omega^-$  are divided into subdomains by triangulation and within each subdomain Gauss integration is performed. Furthermore two integration points are added on the discontinuity for integration of the terms in the local momentum and mass balance. The discontinuity is represented by a straight line in 2D, therefore a standard 1-D integration scheme is used. For the integration over the

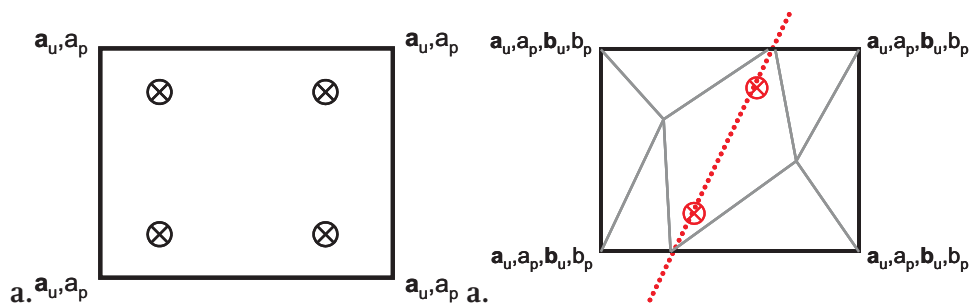


**Figure B.6:** Integration of elements. a. Continuous element b. Element crossed by a discontinuity.

discontinuity Newton-Cotes algorithm is used to prevent locking [79].

# Samenvatting

## Voortplantende discontinuïteiten in geïoniseerde poreuze media

Kleischalie, leem, hydrogelen en biologische weefsels zwellen en krimpen onder verandering van osmotische condities. Deze verandering in condities kan leiden tot lokale spanningen en tot bezwijkgedrag. De materialen worden gemodelleerd als een meerfasenmateriaal bestaande uit een vaste stof met ionen ingebed in de matrix (vaste lading) en een vloeistof met vrij bewegende tegengesteld geladen ionen. Daarom worden ze gekarakteriseerd als geïoniseerde poreuze media. De aanwezigheid van de vaste lading veroorzaakt een verschil in osmotische druk tussen het materiaal en de vloeistof eromheen en daardoor een voorspanning in het materiaal. De reactie van dit materiaal op mechanische of chemische belasting wordt sterk beïnvloed door de aanwezige voorspanning, vloeistof, en scheuren. Ontwerp en gebruik van dit soort materialen vereist begrip van de bezwijkmechanismen. Toepassingen zijn te vinden in de olie-industrie (zoals hydraulic fracturing en boorgatinstabiliteit), materiaal ontwerp (zoals klei, luiers, prothesen) en voor medische behandelingen (hernia en weefselvervangers). De relatie tussen scheurvorming en vloeistofstroming is weinig bestudeerd, maar de relatie tussen scheurvorming en osmotische condities nog minder. Het doel is daarom het effect van osmotische condities te bestuderen op de voortplanting van discontinuïteiten onder verscheidene belastingen in verzadigde geïoniseerde poreuze media gebruikmakend van de eindige-elementenmethode (EEM).

Discrete scheuren kunnen wiskundig voorgesteld worden als verplaatsingssprongen, i.e. sterke discontinuïteiten. Het modelleren van dit soort discontinuïteiten is een uitdaging. Standaard Eindige-elementenmodellen kunnen niet omgaan met discontinuïteiten, omdat de methode continuïteit van het verplaatsingsveld aanneemt. Continue of uitgesmeerde benaderingen met EEM zijn geschikt wanneer er geen prominente scheur is. In het geval van een prominente scheur, kunnen discontinuïteiten toegevoegd worden aan EEM door het aanpassen van het onderliggende rooster, door gebruik te maken van tussenliggende elementen of door het rooster lokaal telkens opnieuw aan te maken. Als alternatief, kan een discontinuïteit onafhankelijk van het onderliggende rooster ingebracht worden door gebruik te maken van de eigenschap dat de basisfuncties een "partition of unity" (eenheidsverzameling) vormen. De "partition of unity" methode laat toe dat discontinue functies toegevoegd worden aan de basisfuncties and daardoor de benadering van discontinue velden onafhankelijk van het onderliggende rooster. Daarvoor wordt het aantal vrijheidsgraden van het element met een scheur verhoogd en niet het aantal elementen. Daardoor verandert de topologie niet. Verder wordt de scheur

niet op voorhand ingelegd waardoor geen dummystijfheden nodig zijn om de scheur dicht te houden alvorens groei, zoals bij sommige geometrische methoden.

Scheurvoortplanting in poreuze media vindt in het algemeen plaats door microsclade voor de scheurtip. Deze microsclade wordt in het model toegevoegd via de "cohesive zone" (zone van cohesie) methode. Deze methode verzamelt alle schade voor de echte scheurtip en brengt deze samen in een vergelijking die het verzwakken van het materiaal representeert en werkt op een virtuele verlenging van de scheur. De vervorming van het materiaal veroorzaakt een vloeistofstroming. Er is nog geen consensus hoe de vloeistofstroming geassocieerd met scheurvorming gemodelleerd kan worden.

In de thesis wordt de "partition of unity" methode gecombineerd met het "cohesive zone" model toegepast voor geïoniseerde poreuze media. Het bulk materiaal wordt gemodelleerd als een tweefasenmateriaal, bestaande uit een vaste stof en een vloeistof, waarbij de invloed van ionenstroom wordt verwaarloosd. Osmose wordt ingecalculleerd in het constitutieve gedrag en in de initiële spanningstoestand. Het model wordt beschreven in hoofdstuk 2.

Het werk bestaat verder uit drie delen. In het eerste deel wordt een analytische oplossing voor een dislocatie in een zwellend medium afgeleid voor verificatie van de methode afgeleid in het tweede deel. In het tweede deel wordt het modelleren van scheurgroei onder afschuiving (modus II) behandeld en in het derde deel wordt scheurgroei onder trekspanning behandeld. Omdat de verschillende belastingen in de laatste twee delen verschillende vloeistofstromingen veroorzaken, wordt de vloeistofstroming verschillend behandeld.

In het eerste deel wordt de verdeling van de afschuifspanning in het vlak van de scheur analytisch afgeleid voor een gesimplificeerde situatie van een niet-voortplantende dislocatie in een osmo-elastisch materiaal (hoofdstuk 3). Deze oplossing wordt afgeleid door gebruik van Fourier en Laplace transformaties. Tevens wordt de vloeistofverdeling afgeleid. Vergelijking van de analytische oplossing met simulaties met een commercieel eindige-elementen-pakket, laat zien dat een goede representatie van scheuren een must is. De analytische oplossing is geschikt als standaard voor verificatie van het "partition of unity" model in het tweede gedeelte.

In het tweede deel wordt het probleem van scheurvorming onder afschuiving onder de loep genomen (hoofdstuk 4). De afschuivingsbelasting veroorzaakt initieel een hoge drukgradiënt over de scheur voor een kleine overgangszone, terwijl de scheurvlakken met elkaar in contact zijn. Met de tijd neemt de druk af in absolute grootte en wordt de overgangszone breder. Dit fenomeen wordt benaderd door het veronderstellen dat de vloeistofstroming over de scheur door schade evenredig is met een sprong in het drukveld. Verder is de evenredigheidsconstante afhankelijk van de tijd sinds opening en laat relaxatie van de vloeistof toe. Vergelijking van numerieke berekeningen met de analytische oplossing van het eerste deel laat goede overeenkomsten zien. Compressietesten laten zien dat voorspanning in het medium invloed heeft op scheurgroei, zowel in snelheid als in richting. De resultaten van scheurgroei zijn redelijk roosteronafhankelijk. In het laatste deel wordt het groeien van discontinuïteiten onder trekspanning bekeken.

Trekspanning op een scheur resulteert in het openen van de scheur en hoge drukgradiënten tussen het medium en de scheur. Dit vereist daardoor een andere aanpak van de vloeistofstroming van modus-I vergeleken met modus-II. In dit geval, wordt een zwakke discontinuïteit verondersteld voor de druk in het scheurgebied, en dus continuïteit van de druk, maar een discontinuïteit in het gradiëntveld. Daarnaast, wordt er voor de vloeistofstroming in de scheur Couette stroming verondersteld. De resultaten laten zien dat afhankelijk van de belasting, permeabiliteit, voorspanning en stijfheid van het materiaal, scheurgroei leidt tot het aantrekken van vloeistof naar de scheurtip toe. Deze vloeistof komt eerder van de scheur zelf dan van de porositeit van het materiaal. Dit leidt tot het sluiten van de scheuren en daarmee het vertragen van de scheurgroei. De resultaten zijn onafhankelijk van het rooster voor materialen met grote stijfheid.

Interessant is dat stapsgewijze scheurgroei door het medium is gezien in beide modi van belastingen. Scheurgroei alterneert met pauzes waarin consolidatie van het scheurtipgebied plaatsvindt. De consolidatie resulteert in een belastingoverdracht van de vloeistof naar de vaste stof. Intussen groeit de belasting op de vaste stof, de bezwijkbelasting wordt gehaald en de scheur groeit weer.

Verder blijkt scheurgroei afhankelijk te zijn van osmotische voorspanning voor beide modi. In modus-II beïnvloedt de voorspanning de hoek van groei. In modus-I kan de voorspanning scheurgroei bevorderen of tegen scheurgroei beschermen afhankelijk van de belasting en de materiaaleigenschappen. Osmotische voorspanning zelf kan scheurgroei toestaan zonder een uitwendige belasting, zoals het spontaan ontstaan van scheuren in klei bij uitdroging, maar dan in volledig door vloeistof verzadigde condities. Dit mechanisme zou een verklaring kunnen zijn voor de scheuren gezien in tussenwervelschijven gedurende degeneratie.





---

## Acknowledgement

Without the opportunity given to me by the people at the faculty Biomedical Engineering, I would not have been able to do this research. Therefore I want to thank first of all my supervisor Jacques Huyghe for the support and discussions. I also thank him for giving me the freedom to pursue ideas, to be involved in extracurricular activities and challenging me by sending me to conferences on my own.

I would further like to thank Frank Baaijens and Keita Ito for the discussions, the financial support and the flexible attitude. It has been a great experience to work side by side with people from biology to mechanics and fluid dynamics, in computer studies and in the lab. Furthermore, I thank all the supporting staff involved.

This project has been part of a Dutch-German collaboration called "Multi-scale Methods in Computational Mechanics". This collaboration between the universities of Delft, Eindhoven, Stuttgart and München, has been a wonderful collaboration for me with fruitful discussion every half a year. The exchange in Stuttgart has helped my project being able to talk to experts on porous media on one side and experts on fracture mechanics on the other side of the wing. I would like to thank Wolfgang Ehlers for the opportunity and the warm welcome in Stuttgart, the supporting staff and the PhD candidates (especially Ayhan) for the organization involved, the discussions and fun.

From this international collaboration, a closer collaboration was initiated between Delft (Rene de Borst and Joris Remmers) and us. I would like to thank Rene de Borst and Joris Remmers for the opportunity, the practical insights and for the use of the Jem/Jive finite element toolkit which has been developed by Habanera. The part-time visit at Delft has been a fruitful experience and I would like to thank all the people present at that time (staff and Ph.D. candidates) for the good times.

I would like to thank all other people who contributed in any way to this thesis. I thank Silvia Wognum and Reinder Roos for the welcome and getting me started with the project. I thank Roman Dittmar for trying the visualization experiments with me.

I thank the people of PromoVE and Hora Est who were present around the time I was an active (board) member, for the training of the soft skills and all the pleasant times. Most of all I thank my roommates of WH4.12, Yvonne Schröder and Peter van den Broek, for the discussions on the biomechanics of the disc and cell mechanics, attacking problems, sports and friendship.

Lastly, the load of a Ph.D. project is much easier to bear with the support from home. Thanks to my family and close friends, with special thanks to my best friend and husband, Harmen Slot.



---

# Curriculum vitae

born August 27, 1979 in 's Gravendeel, The Netherlands

- Jun 2009 - Current* Geomechanical surveillance engineer ,  
at Shell International Exploration and Production B.V..
- Jan 2009 - May 2009* Shell project: Simulation of hydraulic fracturing in tight gas sand.
- Oct 2004 - Dec 2009* Ph.D. candidate, department of Biomedical Engineering,  
Eindhoven University of Technology.  
*Thesis on "Propagating discontinuities in ionized porous media"*
- Oct 2005 - Oct 2007* Board member of PromoVE, Eindhoven University of Technology,  
University-wide Ph.D. council.
- Oct 2006 - Mar 2007* Part-time research visit, group of Engineering Mechanics,  
department of Aerospace Engineering, Delft University of Technology.
- Nov 2005 - Oct 2006* Board member of Hora Est, Eindhoven University of Technology,  
Ph.D. council Mechanical Engineering and Biomedical Engineering.
- Dec 2005 - Feb 2006* Research visit, Institute of Applied Mechanics (Civil Engineering),  
Chair II, University of Stuttgart, Germany.
- Sep 1997 - Jul 2004* M.Sc. Mathematical Engineering, group of Mathematical Physics,  
Delft University of Technology.  
*Thesis on "Pulsated viscous flow through curved elastic tubes"*
- Feb 1999 - Apr 2002* Student assistant, department of Applied Mathematics,  
Delft University of Technology.
- Sep 1992 - Jun 1997* Gymnasium, RSG Oud-Beijerland, Oud-Beijerland.

